

Accurate and scalable exchange-correlation with deep learning

Giulia Luise^{1,†}, Chin-Wei Huang^{1,†}, Thijs Vogels^{1,†}, Derk P. Kooi^{1,†}, Sebastian Ehlert^{1,†}, Stephanie Lanius¹, Klaas J. H. Giesbertz¹, Amir Karton^{1,2}, Deniz Gunceler¹, Megan Stanley¹, Wessel P. Bruinsma¹, Lin Huang¹, Xinran Wei¹, José Garrido Torres¹, Abylay Katbashev¹, Rodrigo Chavez Zavaleta¹, Bálint Máté^{1,a}, Sékou-Oumar Kaba^{1,b}, Roberto Sordillo¹, Yingrong Chen³, David B. Williams-Young³, Christopher M. Bishop¹, Jan Hermann^{1,*}, Rianne van den Berg^{1,*}, Paola Gori-Giorgi^{1,*}

[†]These authors contributed equally and are ordered randomly.

¹*Microsoft Research, AI for Science*

²*School of Science and Technology, University of New England, Australia*

³*Microsoft Quantum*

*{pgorigiorgi,rvandenberg,jan.hermann}@microsoft.com

Abstract Density Functional Theory (DFT) is the most widely used electronic structure method for predicting the properties of molecules and materials. Although DFT is, in principle, an exact reformulation of the Schrödinger equation, practical applications rely on approximations to the unknown exchange-correlation (XC) functional. Most existing XC functionals are constructed using a limited set of increasingly complex, hand-crafted features that improve accuracy at the expense of computational efficiency. Yet, no current approximation achieves the accuracy and generality for predictive modeling of laboratory experiments at chemical accuracy — typically defined as errors below 1 kcal/mol. In this work, we present Skala, a modern deep learning-based XC functional that bypasses expensive hand-designed features by learning representations directly from data. Skala achieves chemical accuracy for atomization energies of small molecules while retaining the computational efficiency typical of semi-local DFT. This performance is enabled by training on an unprecedented volume of high-accuracy reference data generated using computationally intensive wavefunction-based methods. Notably, Skala systematically improves with additional training data covering diverse chemistry. By incorporating a modest amount of additional high-accuracy data tailored to chemistry beyond atomization energies, Skala achieves accuracy competitive with the best-performing hybrid functionals across general main group chemistry, at the cost of semi-local DFT. As the training dataset continues to expand, Skala is poised to further enhance the predictive power of first-principles simulations.

1 Introduction

The energy of the electrons in molecules and materials serves as a glue between their atoms, determining the stability and properties of the chemical structure. Accurately computing the electron energy is therefore essential for predictive modeling across a broad spectrum of applications, including assessing whether a chemical reaction will proceed, whether a candidate drug molecule will bind to its target protein, whether a material is suitable for carbon capture, or if a flow battery can be optimized for renewable energy storage. Unfortunately, computing this energy amounts to solving the Schrödinger equation, whose cost scales exponentially with the number of electrons N . Density functional theory (DFT),¹ provides an exact reformulation that replaces the many-electron wavefunction with the much simpler electron density. Although exact in principle, one component of the total energy — the exchange-correlation (XC) functional — remains unknown and must be approximated in practical implementations. The role of the XC functional is to capture intricate quantum many-body interactions of electrons using only the electron density, making this a universal functional that has the same form for all molecules and materials.^{2,3} Equipped with a formalism⁴ whose cost scales asymptotically as $O(N^3)$, and supported by practical functional approximations pioneered over several decades,^{5–12} DFT has become the computational workhorse in disciplines ranging from (bio)chemistry to catalysis to materials science.¹³ However, DFT users must still choose from among hundreds of XC functional approximations,^{11,13,14} often relying on dedicated benchmark studies or experimental results to guide the choice for the application at hand. Crucially, current XC approximations still fall short of the accuracy required to reliably *predict* experimental outcomes across a wide range of chemical systems and properties.^{11,13,14} Achieving this level of precision — commonly

^{ab}Work done during an internship at Microsoft Research AI for Science ^aCurrent address: *University of Geneva, Department of Computer Science* ^bCurrent address: *Mila – Quebec AI Institute*

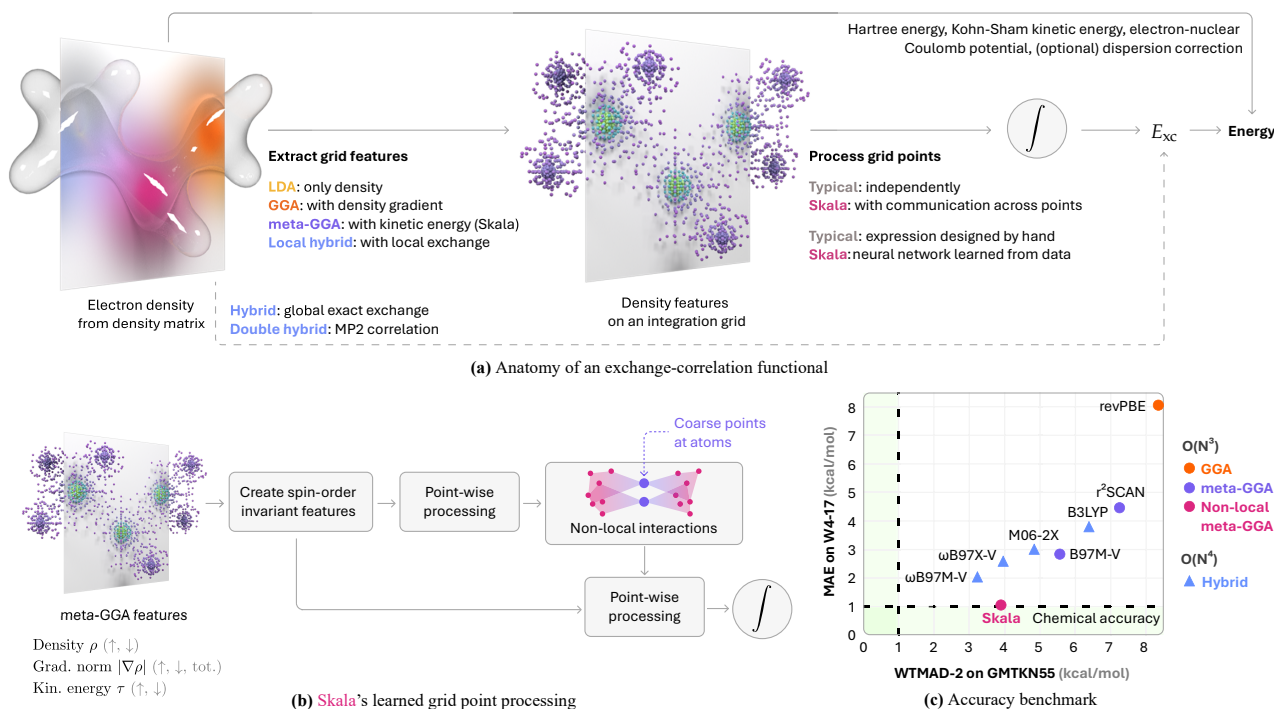


Figure 1: Skala is a scalable deep learned exchange-correlation functional. (a) Jacob’s ladder of density functional approximations¹⁶ defines the rungs **LDA**, **GGA** and **meta-GGA** by expanding the set of semi-local features they extract from an electronic density matrix into a grid representation. The next rungs, **hybrid** and **double hybrid** extract more and more expensive wavefunction-based information directly from the density matrix. **Skala** departs from this ladder by extracting relatively cheap meta-GGA features, and instead gaining expressivity by learning non-local interactions between grid points at a manageable and controllable cost. (b) High-level overview of the neural network architecture for the Skala functional. (c) The plot’s horizontal axis shows weighted total mean absolute deviation (WTMAD-2) on the GMTKN55¹⁴ test set for general main group thermochemistry, kinetics and non-covalent interactions. The vertical axis shows mean absolute error on the diverse atomization energies test set W4-17¹⁷. Skala performs similarly to the best-performing hybrid functionals, and reaches near chemical accuracy (1 kcal/mol) on W4-17.

known as *chemical accuracy* — typically demands errors below ~ 1 kcal/mol for processes involving making and breaking covalent chemical bonds.¹³ This means, for example, that in silico screening pipelines for molecule and material discovery often pass too many candidates to the lab, with a large fraction failing experimental verification. In addition, lower-cost methods such as force fields and property-guided generative models trained on DFT data inherit these same limitations. The search for a general-purpose XC functional that meets chemical accuracy has persisted for over 60 years and is sometimes referred to as “the pursuit of the divine functional”¹⁵ — a challenge with profound implications for accelerating scientific discovery.

The prevailing approach has been to handcraft functional forms based on a limited set of ingredients defined by the so-called Jacob’s ladder of DFT;¹⁶ see Fig. 1. Like its biblical namesake, it is intended to guide users toward the “heaven” of chemical accuracy. The ingredients at the lower rungs allow to retain the asymptotic $O(N^3)$ scaling of DFT, but amount to XC functionals that only use (semi-)local information such as the density, its gradient, the Laplacian and the Kohn-Sham kinetic energy density. However, it is well established that the exact XC functional exhibits non-local dependence on the density,³ and in practice lower-rung approximations yield only limited accuracy. To improve accuracy, researchers began introducing non-locality through wavefunction-like ingredients.^{8,9} While this approach enhances accuracy in many cases, it does not do so for all chemical problems, and it increases the computational complexity¹ to $O(N^4)$, $O(N^5)$ or higher, thereby defining the higher rungs of the ladder. The vast majority of XC functionals is built from this hierarchy of Jacob’s ladder ingredients. They differ primarily in how these ingredients are combined and the number of parameters involved. The focus on these ingredients is driven by their compatibility with exact constraints, offering a rigorous theoretical foundation for building functional approximations.

¹We express computational cost using the standard asymptotic scaling with system size, $O(f(N))$. In practice, however, actual performance depends on algorithmic speedups, hardware optimizations, and prefactors. Therefore, in Sec. 5, we empirically compare the cost of Skala with that of other functionals.

As in many other areas of science, machine learning (ML) has been explored as a promising approach for developing accurate XC functionals, revealing the challenges and subtleties of this complex learning problem.¹⁸ Yet, to date this has not led to a meaningful shift in the established accuracy-cost tradeoff, and no ML-based functional has seen widespread adoption. There are two interlinked reasons for this. First, high-level data for this complex learning problem are very scarce, as they must be generated using computationally intensive wavefunction methods that require specialized expertise to be used at scale. Second, confined to this low-data regime, the vast majority of efforts have been limited to feeding handcrafted features into machine learning models, whether based on Jacob’s ladder ingredients^{19–24} or newly designed descriptors.^{25–28} This approach mirrors machine learning strategies used in computer vision and speech recognition prior to the deep learning (DL) revolution, which may partly account for the limited impact observed so far. In the absence of sufficient data, the handful of efforts to move beyond handcrafted features — though promising — have remained focused on model systems or narrowly defined problems.^{29–33}

In this work, we present a key milestone toward a true deep learning solution to this long-standing scientific problem, addressing both the data scarcity challenge and several core machine learning challenges. Our initial focus is on the total atomization energy (TAE) — the energy required to dissociate a molecule into its constituent atoms — as it represents one of the most fundamental and challenging thermodynamic properties for electronic structure methods.^{34–36} From atomization energies, many other thermodynamic properties in complex chemical transformations involving multiple bond rearrangements can be predicted. Using an efficient wavefunction-based protocol with an accuracy of within 1 kcal/mol relative to experiments, we have generated a highly diverse training set of approximately 80k TAEs, at least two orders of magnitude larger than existing datasets of comparable accuracy.³⁷ We designed a neural network architecture that enables learning data-driven non-local representations essential for chemically accurate XC functionals, using only simple semi-local input features. The result is the Skala functional that reaches chemical accuracy on a well-established benchmark set for atomization energies. With modest additional training data covering properties beyond TAEs, Skala also reaches an accuracy competitive with the leading more computationally expensive hybrid rung functionals across general main group chemistry. Importantly, this is achieved with a scalable neural network design that allows us to retain the asymptotic complexity of semi-local DFT, and which naturally supports GPU acceleration. To further assess its practical utility, we demonstrate that Skala can make reliable predictions for equilibrium geometries and dipole moments. Moreover, while we impose only a minimal set of exact constraints through Skala’s model design, we find that adherence to additional exact constraints emerges as more data is added to the training set. Together, these capabilities make the Skala functional already suitable for practical use. As we continue to generate large amounts of data to cover different portions of chemical space, Skala is poised to systematically improve its accuracy. The implications are far-reaching: making DFT fully predictive removes a fundamental bottleneck in shifting the center of gravity from laboratory-based experimentation to *in silico* discovery — spanning fields from drug and materials design to batteries and sustainable fertilizers.

2 Learning the XC functional: Basic challenges, solutions and practical settings

The success of DFT is based on the Kohn-Sham (KS) formalism,⁴ which decomposes the energy density functional into components that capture large effects such as the Pauli exclusion principle and long-range classical electrostatics, as well as the remaining unknown term that we aim to learn — the XC functional — which accounts for a smaller but crucial energy due to quantum many-body effects. The XC functional $E_{xc}[\rho]$ maps the electron density $\rho(r)$, a positive function over three-dimensional space, to a scalar value representing the XC energy. In practical implementations of KS DFT, all terms except for the XC functional are evaluated using the density represented in a basis set via the density matrix, with atom-centered Gaussian functions being the most commonly used basis functions in chemistry. Focusing on the semi-local functional rungs, the XC energy is evaluated using a representation of the electron density on a large integration grid. For molecules containing up to several hundreds of atoms, the integration grids typically consist of approximately $\sim 10^4 - 10^6$ points. The learning problem we address is to obtain an accurate $E_{xc}^\theta[\rho]$ from the large irregular point cloud representing the local density features on the grid, while learning the crucial non-local representations from data with a neural network architecture with parameters θ . The learned XC functional should have a well-defined limit when the grid becomes infinitely dense and show good convergence as the grid is refined. Aside from the more obvious challenge of obtaining highly-accurate reference energies (also referred to as “labels”) at scale, the learning problem faces other unique challenges:

1. Obtaining accurate ground-state densities at scale, which serve as input for the XC functional, is even more challenging than obtaining accurate energy labels at scale.^{38–40}
2. Having access to accurate wavefunction energies and densities is still not sufficient to extract accurate labels for $E_{xc}[\rho]$ from wavefunction total energies. This stems from the fundamentally different way that the total energy is decomposed in Kohn–Sham DFT compared to wavefunction-based methods.^{41–46}

3. During inference, the XC functional is evaluated repeatedly as part of the self-consistent-field (SCF) KS equations to minimize the total energy of the given molecular system with respect to the density $\rho(r)$. Ensuring that the learned functional drives the system toward convergence at both the correct minimum energy and the correct minimizing density makes this learning task different from standard regression.

Previous ML attempts at learning the XC functional have proposed and analyzed several solutions to all these challenges,^{20,23–25,30,33} with many of them too computationally demanding for the much larger-scale training considered in this work. We address these challenges with a training procedure that consists of a pre-training phase and a fine-tuning phase. To tackle challenges 1 and 2, in the pre-training phase, we train the model with a straightforward reaction energy regression loss using E_{xc}^θ evaluated on densities ρ_{B3LYP} from another approximate XC functional (B3LYP^{8,47}) and E_{xc} labels, as detailed in Sec. B.1 of the Supplementary Information. These labels are extracted from accurate wavefunction energies by subtracting the other KS energy components using B3LYP KS orbitals. Leveraging approximate B3LYP densities during training, as introduced by Kirkpatrick *et al.*²³, along with the large-scale data we generated,³⁷ enables us to expose the model to a broad range of densities and energies. To tackle the third challenge, in the fine-tuning phase, the model is trained using its own SCF densities, generated on the fly during training. This aims to close the gap between the accuracy achieved when evaluating the functional on the fixed input densities from the pre-training stage, and the accuracy obtained when evaluating the functional on its own SCF densities. Crucially, this procedure does not require backpropagating through the SCF cycle, as described in more detail in Sec. B.4 of the Supplementary Information. During the SCF fine-tuning phase we monitor the aforementioned accuracy gap on a holdout validation set, as well as the accuracy of our SCF densities by comparing dipole moments with accurate labels available in the literature.⁴⁸ We stop the fine-tuning when our SCF density stops improving while the accuracy gap is still decreasing.

Several mathematical properties of the XC functional are known, usually referred to as exact constraints.^{3,10,49,50} Following a well-established practice in DFT, we facilitate the satisfaction of some of the most energetically relevant constraints (such as the high-density uniform coordinate scaling, size-consistency, and the Lieb-Oxford lower bound⁵¹) by constructing Skala as

$$E_{\text{xc}}^\theta[\rho] = -\frac{3}{4} \left(\frac{6}{\pi}\right)^{\frac{1}{3}} \int \left(\rho^{(\uparrow)}(r)^{4/3} + \rho^{(\downarrow)}(r)^{4/3}\right) f_\theta[\mathbf{x}[\rho]](r) dr, \quad (1)$$

where $\rho^{(\uparrow)}$ and $\rho^{(\downarrow)}$ are the densities of the two spin channels and f_θ is a bounded enhancement factor. The vast majority of previous ML attempts only learned the enhancement factor with a *local function* $f_\theta(\mathbf{x}[\rho](r))$ of the given hand-designed input features $\mathbf{x}[\rho](r)$.^{20–28} In contrast, our DL approach takes inspiration from neural operators,⁵² and models the enhancement factor as a neural functional that learns finite-range non-local representations from the input features, hence the explicitly distinguishing notation $f_\theta[\mathbf{x}[\rho]](r)$. The architecture for the enhancement factor, depicted in Fig. 1, takes as input the set of density-dependent semi-local features $\mathbf{x}[\rho]$ of the standard meta-generalized-gradient approximation (MGGA) $O(N^3)$ rung at each integration point r . The first module learns spin-order invariant features, followed by further learned local processing at each position r . Subsequently, in the non-local interactions module, information is exchanged with points r' in a finite range from r by communication through a set of coarse points, resulting in a scalable architecture that preserves the asymptotic computational complexity of semi-local DFT. Finally, the spin-order invariant features and the non-local representations are combined and further processed to predict the enhancement factor $f_\theta[\mathbf{x}[\rho]](r)$, followed by a numerical integration using Eq. (1). For a more detailed overview of the architecture, the reader is referred to Extended Data Fig. 6 and Sec. 7.1.

It is worth noting that some approaches incorporate hand-crafted non-locality on the DFT grid to model dispersion^{53–55} — a long-range, subtle yet crucial component of the XC energy — essential for capturing interactions that do not involve the making or breaking of covalent chemical bonds.⁵⁶ Our focus in this first milestone is very different, as we look at thermochemistry (the energy to form and break covalent bonds). We aim to show for the first time that learned non-locality can reach chemical accuracy given sufficient training data and at practical computational cost. This opens the path to a deep-learning, data-driven, systematically improvable approach to the universal XC functional, away from expensive hand-designed features. In particular, the accuracy in main-group thermochemistry has been dominated for decades by the accuracy/cost trade-off of Jacob’s ladder, which we aim to disrupt with this approach. For this reason, we do not attempt to model dispersion yet, and train our functional with a fixed D3 dispersion correction.^{57,58} We leave the learning of dispersion effects using our architecture for future work.

The functional is trained using a dataset consisting of $\sim 150\text{k}$ high-accuracy reaction energies, computed at the CCSD(T)/CBS level or higher, as detailed in Extended Data Table. 1. The largest subset of $\sim 80\text{k}$ data points consists of in-house generated diverse total atomization energies for molecules with up to five non-hydrogen atoms (MSR-ACC/TAE), most of which is released as MSR-ACC/TAE25 described in Ehlert

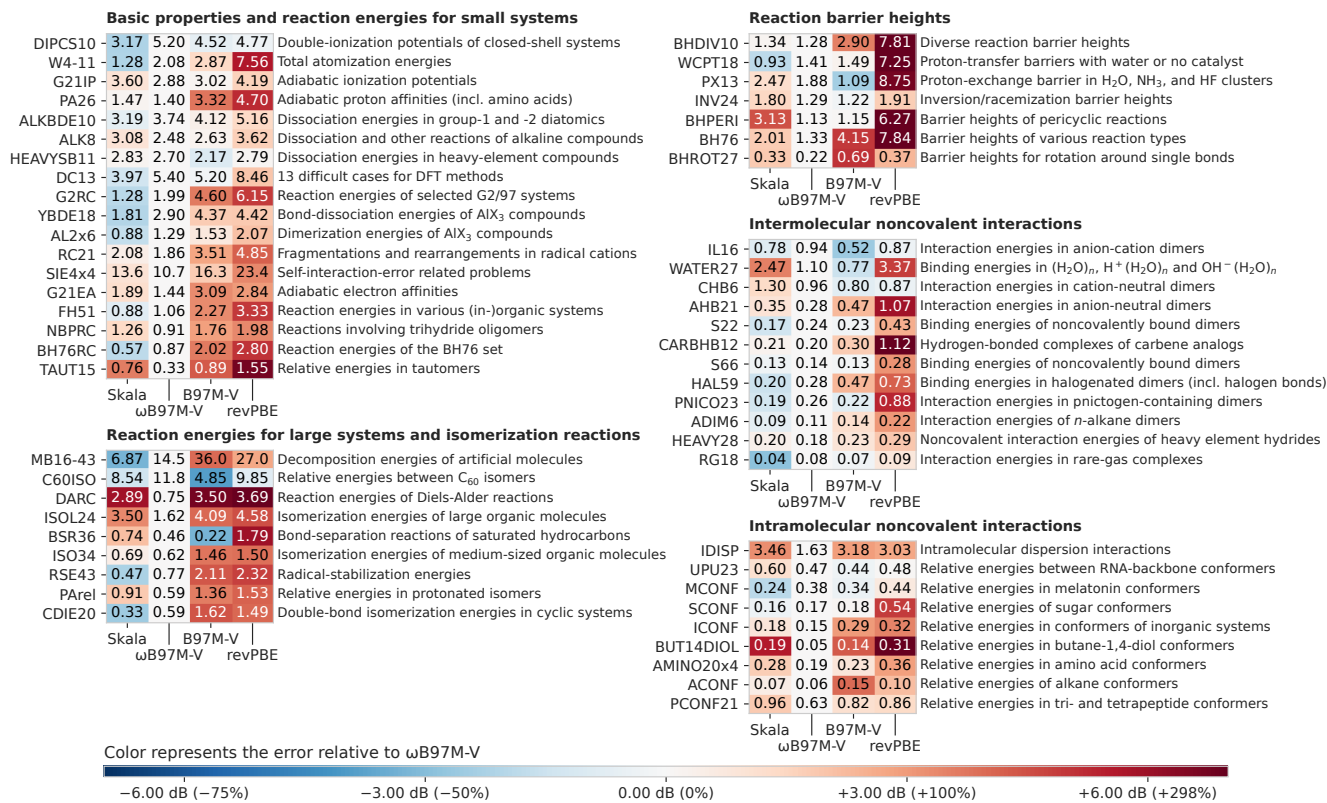


Figure 2: Mean absolute errors in kcal/mol on all GMTKN55 subsets. The datasets are grouped according to the categories reported in the original paper,¹⁴ and sorted by the mean absolute energy per dataset. The colors indicate the performance relative to ωB97M-V, where blue means better and red means worse. The colorbar shows $10 \log_{10}(\text{error ratio})$, which has unit decibel.

*et al.*³⁷. Additionally, smaller in-house generated datasets provide initial coverage of basic properties such as electron affinities (EAs) and ionization potentials (IPs) for atoms, and proton affinities (MSR-ACC/PA) and ionization potentials (MSR-ACC/IP) for molecules. Furthermore, we include in-house generated conformational energies (MSR-ACC/conf) and reaction kinetics (MSR-ACC/Reactions) datasets, as well as four subsets from the NCIAtlas^{59–63} to cover non-covalent interactions. For more details on the training data, see Sec. 7.2 and Sec. C in the Supplementary Information.

3 Accuracy and robustness of Skala

An XC functional is used to predict the energy and properties of *new* molecules: it must therefore show *compositional* generalization to different compounds than those seen during training, which should not be confused with the simpler *configurational* generalization to unseen configurations of the same system used in training.¹⁸ For this reason, as detailed in Sec. 7.2, we have subtracted the overlap with the two main test sets from the training set based on molecular graphs of all systems with more than two atoms. For atomization energies of small molecules, we test on the well-established W4-17 dataset,¹⁷ which contains 200 diverse representative atomization energies. These energies were computed using a very high-level wavefunction protocol that achieves a 95% (2σ) confidence interval of 0.17 kcal/mol and a 99% (3σ) confidence interval of 0.26 kcal/mol with respect to highly accurate experimental TAEs.^{64,65} For performance across main group chemistry, we test on the GMTKN55 database,¹⁴ which is the de facto standard benchmark for electronic structure methods, comprising 55 subsets covering five categories: basic properties, thermochemistry, kinetics, intermolecular non-covalent interactions, and conformational energies. The overall accuracy of an electronic structure method on this broad dataset is encoded in the weighted total mean absolute deviation (WTMAD-2).¹⁴

The accuracy of Skala is readily apparent in Fig. 1c and Extended Data Table 7a, which display the errors on the two benchmark sets alongside those of the best performing XC functionals in the first 3 rungs of the Jacob’s ladder (up to the hybrid or $O(N^4)$ rung).ⁱⁱ For atomization energies of small molecules — the domain

ⁱⁱThe DM21²³ functional is a machine learned local hybrid with hand-crafted features that achieved competitive accuracy on GMTKN55, with a reported WTMAD-2 of 3.97 kcal/mol. However, we omit the performance of DM21 on the test sets W4-17 and GMTKN55 for two reasons. First, its training set fully includes the test set W4-17, and has nontrivial overlap with the atomization

represented by the largest training subset — Skala achieves chemical accuracy, outperforming the state-of-the-art range-separated hybrid functional ω B97M-V,⁶⁶ reducing the error by half. Across the broader domain of main group chemistry, Skala already demonstrates competitive accuracy with the best hybrid XC functionals — a performance enabled by the inclusion of our first batch of training data beyond atomization energies, as detailed in Sec. 3.2. A breakdown of the unweighted errors on the different subsets of GMTKN55 is further shown in Fig. 2, where we compare Skala to the best performing GGA, meta-GGA and hybrid according to the WTMAD-2 metric. We find that Skala outperforms the best hybrid functional in several thermochemistry subsets, while remaining remarkably robust on subsets entirely out of distribution, including those with heavier elements, like Sn, Sb, Te and Pb in the HEAVYSB11 dataset, which were never seen in training. Here, Skala often surpasses the best meta-GGA and, even in the few worst cases, maintains GGA-level accuracy. This highlights the key advantage of training an XC functional on high-accuracy small-molecule data over training a force field: the largest contribution to the energy that governs generalization to different elements and bigger systems is described in KS DFT by other terms than the XC functional.

Given that achieving chemical accuracy on the W4-17 atomization energies test set is a key result, it warrants a more in-depth examination. Our large training dataset MSR-ACC/TAE includes a wide range of diverse and unusual bonding. As shown in Extended Data Table 7b, Skala achieves high-accuracy predictions on the holdout set, while these molecules are very challenging for other functionals. All the molecular structures in MSR-ACC/TAE have single-reference electronic structure character, meaning that they can be treated accurately with the thermochemical W1-F12 protocol based on CCSD(T)/CBS that has been used to label them. The test set W4-17 is instead labeled with the higher-level W4 protocol, based on CCSDTQ5, and also contains multi-reference molecules on which the W1-F12 protocol makes larger errors. To assess the label quality of MSR-ACC/TAE, we computed the MAE of the W1-F12 protocol against the W4 protocol on the single-reference subset of W4-17 (183 reactions out of 200), which is estimated to be 0.49 kcal/mol. Since Skala is trained on single-reference molecules with W1-F12 labels, we further analyze its performance on the single-reference subset of W4-17 in Extended Data Table 7a, comparing it to the full test set. For multireferential molecules, approximate XC functionals can often reach better accuracy through symmetry breaking,^{67,68} which we use for all the functionals on the three most challenging multireferential cases (C_2 , 1BN and B_2). See Sec. E.1 and Table 4 in the Supplementary Information for more details and statistics.

In Sec. D of Supplementary Information, we also examine key aspects of practical usability, such as SCF-cycle convergence (Table 3) and grid-size convergence (Fig. 10). As expected for an ML-based functional, Skala exhibits slightly less smooth behavior than traditional functionals, but all variations remain well within acceptable ranges for practical use.

3.1 The importance of learning nonlocal interactions

The non-local branch of our architecture is remarkably lightweight — Skala comprises just 276,001 parameters in total, with 265,473 allocated to the local branch. This compact design is crucial for maintaining scalability. It is therefore insightful to examine the performance gains enabled by the learned non-locality. In Fig. 3a, we show ablation results by training the local branch only and compare it to the full model that includes the nonlocal module, both on the full training set of Extended Data Table 1. The local model arguably provides the accuracy limit for meta-GGAs on the chemistry covered by GMTKN55, which is not that far from the accuracy of the parameterized meta-GGA B97M-V.⁷⁰ This ablation study is performed with settings that reduce computational demands, as described in Sec. B.3, with SCF fine-tuning limited to 1000 steps and evaluation on the representative subset Diet GMTKN55,⁶⁹ which was designed to approximate the WTMAD-2 metric on the full GMTKN55 dataset.

3.2 Skala’s accuracy improves systematically with training data

Figure 3b reports an ablation study on training data composition, which shows systematic improvement of Skala as we add more diverse chemistry in training. With the same settings as in the previous section (1000 SCF fine-tuning steps and evaluation on Diet GMTKN55), we find that if we train on MSR-ACC/TAE only (A), Skala can reach chemical accuracy on W4-17, while performing at low-tier GGA level on GMTKN55. If we train only on the publicly available data in Extended Data Table 1, which we denote with B and which is composed of NCIAtlas, W4-CC, and the atomic datasets TOT, EA, IP, then the model performs very poorly, with low accuracy and large inter-seed variance. When we add the non-covalent interactions and atomic data in B to MSR-ACC/TAE, we see that Skala maintains the accuracy on W4-17 while improving dramatically

energy subset W4-11 and some of the intermolecular non-covalent interactions subsets of GMTKN55. While some traditional functionals are also fit on GMTKN55, these functionals typically involve only a few parameters. In contrast, the DM21 functional has approximately 4×10^5 parameters, making the performance on the test sets an unreliable measure for generalization. Second, as a local hybrid, DM21 is substantially more expensive than leading XC functionals, as evidenced in Sec. 5.

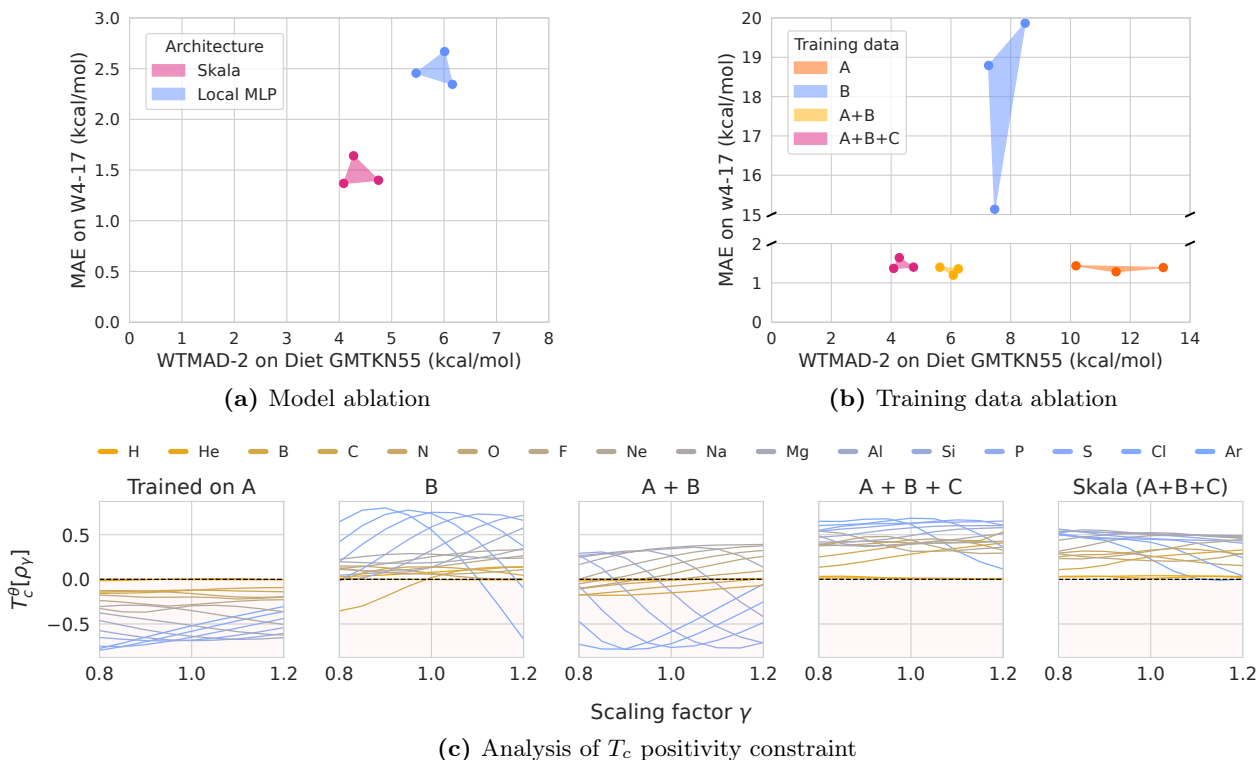


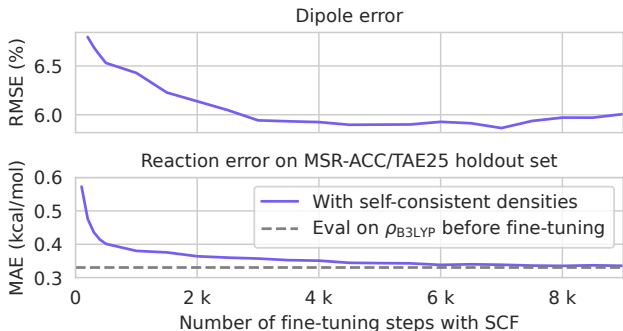
Figure 3: Model insights. (a): Accuracy of Skala’s nonlocal architecture compared with its local branch only, trained on all of the data in Extended Data Table 1. (b): Data composition ablation from Extended Data Table 1: results of training Skala on A, MSR-ACC/TAE only, on B, the public data NCIAtlas and W4-CC plus the Atomic datasets only, on A + B, and further adding all the other MSR-ACC data C. In both ablations, for each setting we trained three models using different random seeds. SCF fine-tuning was limited to 1000 steps, and evaluation was performed on the smaller Diet GMTKN55.⁶⁹ (c) The kinetic correlation component $T_c[\rho_\gamma]$ of E_{xc} as a function of the density scaling parameter γ . The first four panels show results for models trained with the same data compositions as in panel b, while the fifth panel shows results of the final Skala functional, which was trained with more compute. Positive values indicate that exact constraint of T_c being positive is satisfied, while negative values indicate violations.

on GMTKN55. Finally, its performance continues to improve systematically as we add the latest MSR-ACC training data, covering conformers, reactions, IPs and PAs, denoted by C.

3.3 The emergence of learned exact constraints with training data

Exact constraints of the XC functional have been pivotal in guiding the approximations that made DFT practical for thousands of applications in chemistry and materials science.⁵⁰ Many are ingeniously built in by design,^{7,10} lending robustness to the functionals that include them. In Skala, we imposed only minimal constraints to maximize model flexibility, making it interesting to explore whether exact constraints can emerge from data.

As part of the same data ablation study of Fig. 3b, we tracked whether the model learns to satisfy the positivity of T_c ,⁴⁹ the kinetic correlation component of E_{xc} . This constraint reflects the physical principle that correlation makes electrons move faster to avoid one another due to their Coulomb repulsion. In Fig. 3c we evaluate $T_c^\theta[\rho_\gamma]$ as a function of the scaling parameter γ , which rescales the density as $\rho_\gamma(r) = \gamma^3 \rho(\gamma r)$, for all atoms from the Atomic TOT set in Extended Data Table 1. We clearly observe that the constraint is violated when the model is trained only on MSR-ACC/TAE (A). In contrast, when the model is trained only on the public NCIAtlas, W4-CC, and Atomic datasets (B), the constraints are violated significantly less often. This is likely attributed to the presence of dissociation curves in NCIAtlas, which sample small configurational density variations that provide a training signal akin to the derivative term in $T_c[\rho_\gamma] = \gamma^2 \frac{d}{d\gamma} \frac{E_{xc}[\rho_\gamma]}{\gamma}$. When trained on the combined (A + B), the model exhibits mixed performance. The benefit of the training set including the datasets in (B) is likely diluted when the TAE set (A) is included, given that dataset (A) contains a significantly larger number of reactions (almost 6 times larger) compared to (B). Once all MSR-ACC data is added to the training set, including conformers, reactions, IPs, and PAs, we observe a definite signal that the functional has learned to satisfy the physical constraint correctly, which is also reflected in the results for the final Skala model, trained with more compute. The emergence of Skala learning to satisfy this constraint for the largest composition of



	RMSE			Mean	Max	Std
	All	NSP	SP			
revPBE	11.79	9.87	14.78	8.45	42.96	8.26
r ² SCAN	8.95	8.16	10.28	6.07	32.27	6.60
B97M-V	11.54	10.19	13.74	7.21	67.70	9.03
B3LYP	7.09	6.60	7.95	4.13	45.94	5.79
M06-2X	7.73	7.69	7.79	4.19	61.56	6.52
ω B97X-V	5.18	4.64	6.08	3.58	18.81	3.76
ω B97M-V	5.84	5.44	6.54	3.81	32.31	4.44
Skala	5.94	5.19	7.14	3.88	22.29	4.51

(a) Effect of fine-tuning with SCF on dipole and reaction error

(b) Dipole errors⁴⁸ of various functionals

	LMGB35 [\AA]	HMGB11 [\AA]	CCse21 bond lengths [\AA]	CCse21 bond angles [$^\circ$]
GFN2-xTB (<i>tblite</i>)	0.021	0.030	0.008	0.81
revPBE	0.014	0.033	0.012	0.49
r ² SCAN	0.006	0.012	0.004	0.28
B97M-V	0.007	0.023	0.005	0.40
B3LYP	0.007	0.026	0.004	0.38
ω B97X-V	0.009	0.040	0.005	0.24
ω B97M-V	0.008	0.010	0.005	0.18
Skala	0.014	0.032	0.012	0.26

(c) Geometry optimization errors of various functionals

Figure 4: Dipoles and equilibrium geometries. (a): The dipole error⁴⁸ (top) and reaction error on the holdout set of total atomization energies (bottom) during the fine-tuning of Skala with self-consistent densities instead of B3LYP densities. The reaction error statistics were collected on 729 out of 730 reactions that were consistently converged during all fine-tuning iterations. For dipoles, we show the root-mean-square of the regularized error⁴⁸ (RMSE, top) and, for energies, the mean absolute error (MAE, bottom). (b): Comparison of Skala’s dipole errors on the benchmark of Hait & Head-Gordon⁴⁸ against reference functionals. (c): Geometry optimization results. The geometries in the benchmark datasets LMGB35, HMGB11⁷¹ and CCse21⁷² were optimized for various functionals and Skala. The table shows average absolute errors for bond lengths (in Ångstrom) and bond angles (in degrees) compared to the ground truth values from these datasets. Box plots show the quartiles of the error distribution.

datasets likely stems from the fact that dataset C contains a sufficiently large proportion of data with relatively smaller density variations, such as those found in the MSR-ACC conformers and reactions datasets. For more detailed results, the reader is referred to Sec. E.5 of the Supplementary Information.

4 Beyond energies: Densities and equilibrium geometries

Since labels for accurate densities and equilibrium geometries are not included in our training data, it is essential to verify that Skala maintains at the very least the baseline quality of standard semi-local DFT for these observables, to ensure its practical utility.

4.1 Densities

Starting with densities, it is important to recall that the energy error from a KS DFT calculation with a given XC functional can be decomposed into two components: a *functional error*, which is the error the functional would make if evaluated on the exact density, and a *density-driven error*, which is the error the exact functional would make when evaluated on the self-consistent density of the approximate functional.^{73–75} These two errors can compensate each other,^{76,77} yielding XC approximations that improve energies by worsening their SCF densities, “straying from the path toward the exact functional”, quoting Medvedev *et al.*⁷⁸ We train our functional on fixed approximate densities ρ_{B3LYP} and we further fine-tune it using on-the-fly calculated SCF densities for a small number of steps, to close the gap between the accuracy learned on ρ_{B3LYP} and that on the self-consistent densities ρ_{Skala} produced by Skala, as detailed in Sec. B.4 of the Supplementary Information. To ensure that this SCF fine-tuning does not rely on error compensation, we monitor the quality of the SCF density by comparing its dipole moments against a highly accurate dataset of 151 structures.⁴⁸ Figure 4a illustrates how, on the TAE holdout set, the gap between the accuracy learned on B3LYP densities and the actual SCF evaluation of Skala closes during the fine-tuning process. We also report how the errors of the SCF Skala density behave

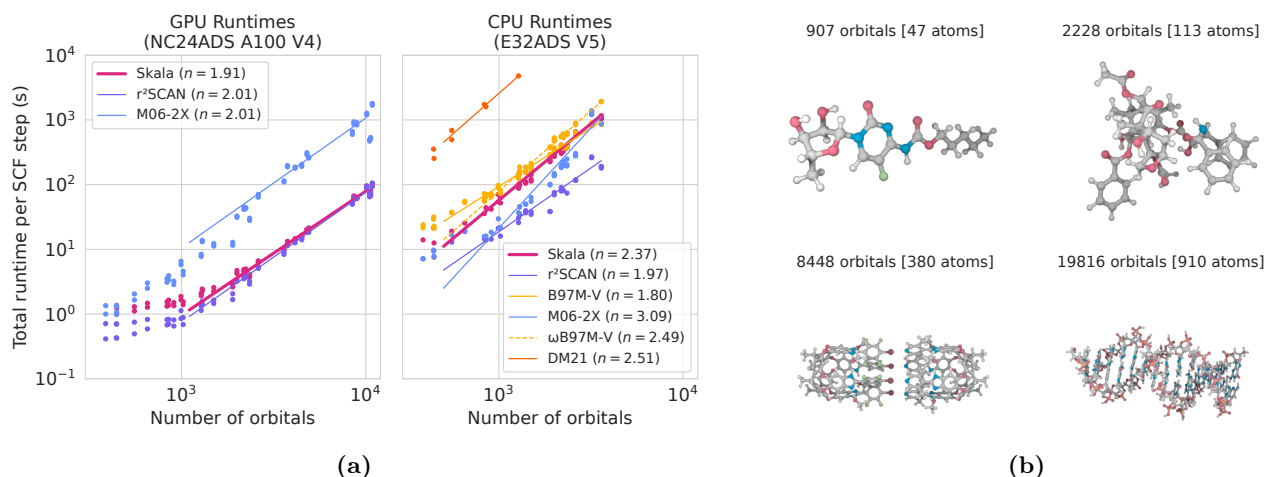


Figure 5: Computational cost. (a): Runtime for molecules with increasing molecular size for various functionals. The left panel shows results for computations performed on Azure NC24ADS V4 A100 virtual machines with Accelerated DFT,⁸⁰. The right panel shows CPU timings performed on Azure E32ADS V5 virtual machines with PySCF 2.7.0,⁸¹. For more detailed settings the reader is referred to Sec. D.7. Lines show fitted power laws aN_{orbitals}^n disregarding offsets at smaller system sizes. The fitted power n is reported in the legend for each functional. (b) A sample of the molecules used for evaluating timings of Skala in Accelerated DFT and PySCF. See Sec. D.1 for more information on all molecules.

during the fine-tuning. We clearly see a first phase where the model is improving both energies and densities, a second phase in which only energies are improved, and a subsequent phase in which the SCF densities start to deteriorate, indicating that the model begins to exploit compensation between functional and density-driven error: at this point, we terminate the fine-tuning. The final Skala error on the dipole dataset falls below the error of B3LYP and is close to the errors of the best range-separated hybrid functionals, as shown in Table 4b.

4.2 Equilibrium geometries

One of the use cases for DFT is to predict the equilibrium structures of molecules by relaxing the positions of the nuclei to their lowest energy configuration. We test geometries optimized with Skala against (semi-)experimental datasets that include light main group bond lengths (LMGB35),⁷¹ heavy main group bond lengths (HMGB11),⁷¹ and the bond lengths and bond angles of the 21 small molecules of the CCse21 set.⁷² The results are shown in Table 4c, where, besides comparing with functionals in different rungs, we also compare to the semi-empirical GFN2-xTB⁷⁹ method. Skala was not specifically trained for the accuracy of optimal geometries, and we see that its performance is of GGA quality or better in most benchmarks, with the worst outlier being the significantly out-of-distribution Pb-Pb bond length in the HMGB11 dataset. For details on the evaluation settings the reader is referred to Sec. D.6 of the Supplementary Information.

5 Computational cost of Skala

The computational cost of quantum chemistry methods is commonly expressed through its asymptotic scaling with system size, $O(f(N))$, a convention we have followed so far in this paper. In practice, the prefactors of that scaling can differ by orders of magnitude between methods, the cost can be dominated by other terms for smaller to medium-sized molecules, and the bottleneck for scaling may be memory rather than compute.⁸² Moreover, hardware-specific optimizations and algorithmic advances continue to lower these scalings in practice.

For all these reasons, although our architecture design ensures that Skala has the same asymptotic scaling as meta-GGA semi-local DFT, we have to empirically verify its prefactor and actual cost as system size increases. A relevant analogy to clarify why this is crucially important is the following. At the hybrid rung of Jacob’s ladder we find both global hybrids and local hybrids. For global hybrids, the XC functional contains a fixed fraction of exact exchange evaluated on the basis set, which can be made computationally efficient but lacks universality, as different systems often require different optimal fractions. In contrast, the more flexible local hybrids allow the fraction of exact exchange to be position-dependent, requiring the exchange to be evaluated on the grid. Although both have the same asymptotic scaling, the latter has a much larger prefactor, with basic implementations being even more expensive than the double hybrids of the next rung. Despite impressive progress over the last decade,^{83–85} less costly implementations of local hybrids are still very rare,⁸⁶ which has

prevented their widespread use so far. A reasonable cost *before any dedicated optimization* is therefore essential for quick adoption of an XC functional in practical applications.

Figure 5 presents the computational runtimes of two non-optimized implementations of Skala: one GPU-based version integrated into Accelerated DFT,⁸⁰ and one CPU-based version implemented in PySCF.⁸¹ For the GPU-based implementation in Accelerated DFT, we clearly observe that after a modest prefactor for small systems, Skala’s cost becomes the same as the semi-local meta-GGA r²SCAN, at least 10 times lower than hybrid cost.⁸⁷ The CPU-based implementation in PySCF shows a reasonable $\sim 3\text{--}4$ prefactor with respect to r²SCAN. Skala’s scaling here is also affected by a suboptimal interface with PySCF, which does not take full advantage of basis function screening when computing the features, resulting in higher computational overhead. Therefore, this second test provides a rather loose upper bound to Skala’s cost. For more details on the evaluation settings see Supplementary Information Sec. D.7 and for additional results on the GPU cost for the exchange correlation energy component and electron repulsion integrals see Sec. E.4.

The take-home message of these results is that already a very basic, non-optimized implementation of Skala has a cost comparable to functionals routinely used in practical applications. To put this in perspective: going back to the comparison with local hybrids, a basic implementation of the DM21²³ functional in PySCF has a computational cost more than 100 times higher than standard functionals, as shown in Fig. 5.

6 Conclusion

We have presented a deep learning-based exchange-correlation functional, Skala, that marks a significant step forward in the long-standing quest for a general-purpose, chemically accurate, and computationally efficient density functional. By addressing the dual challenges of data scarcity and model design, we demonstrate that it is possible to learn non-local quantum mechanical effects from simple semi-local inputs, without sacrificing the favorable $O(N^3)$ scaling of semi-local DFT.

Our approach leverages a large, diverse high-accuracy dataset and a neural architecture capable of capturing non-locality in a scalable manner. The resulting functional achieves chemical accuracy on benchmark datasets for atomization energies of small molecules and performs competitively in terms of accuracy with state-of-the-art range-separated hybrid functionals across a broad range of main group chemistry, at the cost of only semi-local DFT. These results show that deep learning can break the traditional trade-off between accuracy and computational cost that has limited XC functional development for decades.

One of the key advantages of learning an XC functional — rather than a force field — from high-accuracy wavefunction data is that the KS framework inherently captures the dominant energy contributions needed to generalize across unseen elements and larger systems. The XC functional represents a smaller correction term, and by embedding basic properties into its design, Skala remains robust: it generalizes with high accuracy to most thermochemistry benchmark sets and, in the worst-case scenario, defaults to the performance of (potentially lower-tier) semi-local DFT. This makes learning an accurate XC functional a compelling strategy for transferring the accuracy of wavefunction methods from small systems to the medium-large ones accessible to DFT. In turn, the learned functional can be used to generate high-quality data for larger systems, enabling the training of force fields and other models. This creates a cascade of accuracy transfer across scales, with the potential to transform the predictive power of computational chemistry.

As we continue to expand the training dataset to encompass a broader range of chemical phenomena, we expect Skala to systematically improve in both accuracy and generality. A key challenge in this endeavor will be extending coverage to multi-reference and strongly correlated systems, where generating accurate reference data at scale remains an obstacle that will require new scientific and computational advances to overcome. Skala opens the door to a new generation of data-driven functionals that are both predictive and efficient, enabling transformative advances in computational chemistry, materials science, and molecular discovery.

References

1. Kohn, W. Nobel Lecture: Electronic structure of matter—wave functions and density functionals. *Rev. Mod. Phys.* **71**, 1253. doi:10.1103/RevModPhys.71.1253 (1999).
2. Hohenberg, P. & Kohn, W. Inhomogeneous Electron Gas. *Phys. Rev.* **136**, B864. doi:10.1103/PhysRev.136.B864 (1964).
3. Lieb, E. H. Density functionals for coulomb systems. *Int. J. Quantum Chem.* **24**, 243. doi:10.1002/qua.560240302 (1983).
4. Kohn, W. & Sham, L. J. Self-Consistent Equations Including Exchange and Correlation Effects. *Phys. Rev.* **140**, A1133. doi:10.1103/PhysRev.140.A1133 (1965).

5. Perdew, J. P. & Yue, W. Accurate and simple density functional for the electronic exchange energy: Generalized gradient approximation. *Phys. Rev. B* **33**, 8800. doi:10.1103/PhysRevB.33.8800 (1986).
6. Becke, A. D. Density-functional exchange-energy approximation with correct asymptotic behavior. *Phys. Rev. A* **38**, 3098. doi:10.1103/PhysRevA.38.3098 (1988).
7. Perdew, J. P., Burke, K. & Ernzerhof, M. Generalized Gradient Approximation Made Simple. *Phys. Rev. Lett.* **77**, 3865. doi:10.1103/PhysRevLett.77.3865 (1996).
8. Becke, A. D. Density-functional thermochemistry. III. The role of exact exchange. *J. Chem. Phys.* **98**, 5648. doi:10.1063/1.464913 (1993).
9. Grimme, S. Semiempirical hybrid density functional with perturbative second-order correlation. *J. Chem. Phys.* **124**, 034108. doi:10.1063/1.2148954 (2006).
10. Sun, J., Ruzsinszky, A. & Perdew, J. P. Strongly Constrained and Appropriately Normed Semilocal Density Functional. *Phys. Rev. Lett.* **115**, 036402. doi:10.1103/PhysRevLett.115.036402 (2015).
11. Mardirossian, N. & Head-Gordon, M. Thirty years of density functional theory in computational chemistry: an overview and extensive assessment of 200 density functionals. *Mol. Phys.* **115**, 2315. doi:10.1080/00268976.2017.1333644 (2017).
12. Lebeda, T. & Kümmel, S. Meta-GGA that describes weak interactions in addition to bond energies and band gaps. *Phys. Rev. B* **111**, 155133. doi:10.1103/PhysRevB.111.155133 (2025).
13. M. Teale, A. *et al.* DFT exchange: sharing perspectives on the workhorse of quantum chemistry and materials science. *Phys. Chem. Chem. Phys.* **24**, 28700. doi:10.1039/D2CP02827A (2022).
14. Goerigk, L., Hansen, A., Bauer, C., Ehrlich, S., Najibi, A. & Grimme, S. A look at the density functional theory zoo with the advanced GMTKN55 database for general main group thermochemistry, kinetics and noncovalent interactions. *Phys. Chem. Chem. Phys.* **19**, 32184. doi:10.1039/c7cp04913g (2017).
15. Mattsson, A. E. In Pursuit of the "Divine" Functional. *Science* **298**, 759. doi:10.1126/science.1077710 (2002).
16. Perdew, J. P. & Schmidt, K. Jacob's ladder of density functional approximations for the exchange-correlation energy. *AIP Conf. Proc.* **577**, 1. doi:10.1063/1.1390175 (2001).
17. Karton, A., Sylvetsky, N. & Martin, J. M. L. W4-17: A diverse and high-confidence dataset of atomization energies for benchmarking high-level electronic structure methods. *J. Comput. Chem.* **38**, 2063. doi:10.1002/jcc.24854 (2017).
18. Akashi, R., Sogal, M. & Burke, K. *Can machines learn density functionals? Past, present, and future of ML in DFT* 2025. doi:10.48550/arXiv.2503.01709.
19. Tozer, D. J., Ingamells, V. E. & Handy, N. C. Exchange-correlation potentials. *J. Chem. Phys.* **105**, 9200. doi:10.1063/1.472753 (1996).
20. Dick, S. & Fernandez-Serra, M. Machine learning accurate exchange and correlation functionals of the electronic density. *Nat. Commun.* **11**, 3509. doi:10.1038/s41467-020-17265-7 (2020).
21. Kasim, M. F. & Vinko, S. M. Learning the Exchange-Correlation Functional from Nature with Fully Differentiable Density Functional Theory. *Phys. Rev. Lett.* **127**, 126403. doi:10.1103/PhysRevLett.127.126403 (2021).
22. Cuierrier, E., Roy, P.-O. & Ernzerhof, M. Constructing and representing exchange-correlation holes through artificial neural networks. *J. Chem. Phys.* **155**, 174121. doi:10.1063/5.0062940 (2021).
23. Kirkpatrick, J. *et al.* Pushing the frontiers of density functionals by solving the fractional electron problem. *Science* **374**, 1385. doi:10.1126/science.abj6511 (2021).
24. Kanungo, B., Hatch, J., Zimmerman, P. M. & Gavini, V. *Learning local and semi-local density functionals from exact exchange-correlation potentials and energies* 2024. <http://arxiv.org/abs/2409.06498>.
25. Nagai, R., Akashi, R. & Sugino, O. Completing density functional theory by machine learning hidden messages from molecules. *npj Comput. Mater.* **6**, 1. doi:10.1038/s41524-020-0310-0 (2020).
26. Bystrom, K. & Kozinsky, B. CIDER: An Expressive, Nonlocal Feature Set for Machine Learning Density Functionals with Exact Constraints. *J. Chem. Theory Comput.* **18**, 2180. doi:10.1021/acs.jctc.1c00904 (2022).
27. Bystrom, K. & Kozinsky, B. *Nonlocal Machine-Learned Exchange Functional for Molecules and Solids* 2023. doi:10.48550/arXiv.2303.00682.
28. Polak, E., Zhao, H. & Vuckovic, S. *Real-space machine learning of correlation density functionals* 2024. doi:10.26434/chemrxiv-2024-zk6hp.

29. Schmidt, J., Benavides-Riveros, C. L. & Marques, M. A. L. Machine Learning the Physical Nonlocal Exchange–Correlation Functional of Density-Functional Theory. *J. Phys. Chem. Lett.* **10**, 6425. doi:10.1021/acs.jpcllett.9b02422 (2019).
30. Li, L., Hoyer, S., Pederson, R., Sun, R., Cubuk, E. D., Riley, P. & Burke, K. Kohn-Sham Equations as Regularizer: Building Prior Knowledge into Machine-Learned Physics. *Phys. Rev. Lett.* **126**, 036401. doi:10.1103/PhysRevLett.126.036401 (2021).
31. Margraf, J. T. & Reuter, K. Pure non-local machine-learned density functional theory for electron correlation. *Nat. Commun.* **12**, 344. doi:10.1038/s41467-020-20471-y (2021).
32. Kalita, B., Pederson, R., Chen, J., Li, L. & Burke, K. How Well Does Kohn–Sham Regularizer Work for Weakly Correlated Systems? *J. Phys. Chem. Lett.* **13**, 2540. doi:10.1021/acs.jpcllett.2c00371 (2022).
33. Gao, N., Eberhard, E. & Günnemann, S. *Learning Equivariant Non-Local Electron Density Functionals* 2024. <http://arxiv.org/abs/2410.07972>.
34. Sprague, M. K. & Irikura, K. K. Quantitative estimation of uncertainties from wavefunction diagnostics. *Theor. Chem. Accounts* **133**, 1544. doi:10.1007/s00214-014-1544-z (2014).
35. Curtiss, L. A., Raghavachari, K., Redfern, P. C. & Pople, J. A. Assessment of Gaussian-3 and density functional theories for a larger experimental test set. *J. Chem. Phys.* **112**, 7374. doi:10.1063/1.481336 (2000).
36. Curtiss, L. A., Redfern, P. C. & Raghavachari, K. Assessment of Gaussian-3 and density-functional theories on the G3/05 test set of experimental energies. *J. Chem. Phys.* **123**, 124107. doi:10.1063/1.2039080 (2005).
37. Ehlert, S. *et al. Accurate Chemistry Collection: Coupled cluster atomization energies for broad chemical space* 2025. doi:10.48550/arXiv.2506.14492.
38. Assaraf, R., Caffarel, M. & Scemama, A. Improved Monte Carlo estimators for the one-body density. *Phys. Rev. E* **75**, 035701. doi:10.1103/PhysRevE.75.035701 (2007).
39. Chen, S., Motta, M., Ma, F. & Zhang, S. *Ab initio* electronic density in solids by many-body plane-wave auxiliary-field quantum Monte Carlo calculations. *Phys. Rev. B* **103**, 075138. doi:10.1103/PhysRevB.103.075138 (2021).
40. Cheng, L., Szabó, P. B., Schätzle, Z., Kooi, D. P., Köhler, J., Giesbertz, K. J. H., Noé, F., Hermann, J., Gori-Giorgi, P. & Foster, A. Highly accurate real-space electron densities with neural networks. *J. Chem. Phys.* **162**, 034120. doi:10.1063/5.0236919 (2025).
41. Umrigar, C. J. & Gonze, X. Accurate exchange-correlation potentials and total-energy components for the helium isoelectronic series. *Phys. Rev. A* **50**, 3827. doi:10.1103/PhysRevA.50.3827 (1994).
42. Schipper, P. R. T., Gritsenko, O. V. & Baerends, E. J. One-determinantal pure state versus ensemble Kohn-Sham solutions in the case of strong electron correlation: CH₂ and C₂. *Theor. Chem. Accounts: Theory, Comput. Model. (Theoretica Chimica Acta)* **99**, 329. doi:10.1007/s002140050343 (1998).
43. Colonna, F. & Savin, A. Correlation energies for some two- and four-electron systems along the adiabatic connection in density functional theory. *J. Chem. Phys.* **110**, 2828. doi:10.1063/1.478234 (1999).
44. Ryabinkin, I. G., Kohut, S. V. & Staroverov, V. N. Reduction of Electronic Wave Functions to Kohn-Sham Effective Potentials. *Phys. Rev. Lett.* **115**, 083001. doi:10.1103/PhysRevLett.115.083001 (2015).
45. Tribedi, S., Dang, D.-K., Kanungo, B., Gavini, V. & Zimmerman, P. M. Exchange correlation potentials from full configuration interaction in a Slater orbital basis. *J. Chem. Phys.* **159**, 054106. doi:10.1063/5.0157942 (2023).
46. Kanungo, B., Tribedi, S., Zimmerman, P. M. & Gavini, V. Accelerating inverse Kohn–Sham calculations using reduced density matrices. *J. Chem. Phys.* **162**, 064112. doi:10.1063/5.0241971 (2025).
47. Stephens, P. J., Devlin, F. J., Chabalowski, C. F. & Frisch, M. J. *Ab Initio* Calculation of Vibrational Absorption and Circular Dichroism Spectra Using Density Functional Force Fields. *J. Phys. Chem.* **98**, 11623. doi:10.1021/j100096a001 (1994).
48. Hait, D. & Head-Gordon, M. How Accurate Is Density Functional Theory at Predicting Dipole Moments? An Assessment Using a New Database of 200 Benchmark Values. *J. Chem. Theory Comput.* **14**, 1969. doi:10.1021/acs.jctc.7b01252 (2018).
49. Levy, M. & Perdew, J. P. Hellmann-Feynman, virial, and scaling requisites for the exact universal density functionals. Shape of the correlation potential and diamagnetic susceptibility for atoms. *Phys. Rev. A* **32**, 2010. doi:10.1103/PhysRevA.32.2010 (1985).

50. Kaplan, A. D., Levy, M. & Perdew, J. P. *Predictive Power of the Exact Constraints and Appropriate Norms in Density Functional Theory* 2022. doi:10.1146/annurev-physchem-062422-013259.
51. Lieb, E. H. A lower bound for Coulomb energies. *Phys. Lett. A* **70**, 444. doi:10.1016/0375-9601(79)90358-X (1979).
52. Kovachki, N., Li, Z., Liu, B., Aizzadenesheli, K., Bhattacharya, K., Stuart, A. & Anandkumar, A. *Neural Operator: Learning Maps Between Function Spaces* 2023. <http://arxiv.org/abs/2108.08481>.
53. Dion, M., Rydberg, H., Schröder, E., Langreth, D. C. & Lundqvist, B. I. Van der Waals Density Functional for General Geometries. *Phys. Rev. Lett.* **92**, 246401. doi:10.1103/PhysRevLett.92.246401 (2004).
54. Langreth, D. C., Dion, M., Rydberg, H., Schröder, E., Hyldgaard, P. & Lundqvist, B. I. Van der Waals density functional theory with applications: Van Der Waals DFT. *Int. J. Quantum Chem.* **101**, 599. doi:10.1002/qua.20315 (2005).
55. Vydrov, O. A. & Van Voorhis, T. Nonlocal van der Waals density functional: The simpler the better. *J. Chem. Phys.* **133**, 244103. doi:10.1063/1.3521275 (2010).
56. Hermann, J., DiStasio, R. A. & Tkatchenko, A. First-Principles Models for van der Waals Interactions in Molecules and Materials: Concepts, Theory, and Applications. *Chem. Rev.* **117**, 4714. doi:10.1021/acs.chemrev.6b00446 (2017).
57. Grimme, S., Antony, J., Ehrlich, S. & Krieg, H. A consistent and accurate ab initio parametrization of density functional dispersion correction (DFT-D) for the 94 elements H-Pu. *J. Chem. Phys.* **132**, 154104. doi:10.1063/1.3382344 (2010).
58. Grimme, S., Ehrlich, S. & Goerigk, L. Effect of the damping function in dispersion corrected density functional theory. *J. Comput. Chem.* **32**, 1456. doi:10.1002/jcc.21759 (2011).
59. Řezáč, J. Non-Covalent Interactions Atlas Benchmark Data Sets 2: Hydrogen Bonding in an Extended Chemical Space. *J. Chem. Theory Comput.* **16**, 6305. doi:10.1021/acs.jctc.0c00715 (2020).
60. Řezáč, J. Non-Covalent Interactions Atlas Benchmark Data Sets: Hydrogen Bonding. *J. Chem. Theory Comput.* **16**, 2355. doi:10.1021/acs.jctc.9b01265 (2020).
61. Kříž, K., Nováček, M. & Řezáč, J. Non-Covalent Interactions Atlas Benchmark Data Sets 3: Repulsive Contacts. *J. Chem. Theory Comput.* **17**, 1548. doi:10.1021/acs.jctc.0c01341 (2021).
62. Kříž, K. & Řezáč, J. Non-covalent interactions atlas benchmark data sets 4: σ -hole interactions. *Phys. Chem. Chem. Phys.* **24**, 14794. doi:10.1039/D2CP01600A (2022).
63. Řezáč, J. Non-Covalent Interactions Atlas benchmark data sets 5: London dispersion in an extended chemical space. *Phys. Chem. Chem. Phys.* **24**, 14780. doi:10.1039/D2CP01602H (2022).
64. Karton, A., Rabinovich, E., Martin, J. M. L. & Ruscic, B. W4 theory for computational thermochemistry: In pursuit of confident sub-kJ/mol predictions. *J. Chem. Phys.* **125**, 144108. doi:10.1063/1.2348881 (2006).
65. Karton, A., Daon, S. & Martin, J. M. W4-11: A high-confidence benchmark dataset for computational thermochemistry derived from first-principles W4 data. *Chem. Phys. Lett.* **510**, 165. doi:10.1016/j.cplett.2011.05.007 (2011).
66. Mardirossian, N. & Head-Gordon, M. ω B97M-V: A combinatorially optimized, range-separated hybrid, meta-GGA density functional with VV10 nonlocal correlation. *J. Chem. Phys.* **144**, 214110. doi:10.1063/1.4952647 (2016).
67. Perdew, J. P., Ruzsinszky, A., Sun, J., Nepal, N. K. & Kaplan, A. D. Interpretations of ground-state symmetry breaking and strong correlation in wavefunction and density functional theories. *Proc. National Acad. Sci.* **118**, e2017850118. doi:10.1073/pnas.2017850118 (2021).
68. Perdew, J. P., Chowdhury, S. T. u. R., Shahi, C., Kaplan, A. D., Song, D. & Bylaska, E. J. Symmetry Breaking with the SCAN Density Functional Describes Strong Correlation in the Singlet Carbon Dimer. *J. Phys. Chem. A* **127**, 384. doi:10.1021/acs.jpca.2c07590 (2023).
69. Gould, T. ‘Diet GMTKN55’ offers accelerated benchmarking through a representative subset approach. *Phys. Chem. Chem. Phys.* **20**, 27735. doi:10.1039/C8CP05554H (2018).
70. Mardirossian, N. & Head-Gordon, M. Mapping the genome of meta-generalized gradient approximation density functionals: The search for B97M-V. *J. Chem. Phys.* **142**, 074111. doi:10.1063/1.4907719 (2015).
71. Grimme, S., Brandenburg, J. G., Bannwarth, C. & Hansen, A. Consistent structures and interactions by density functional theory with small atomic orbital basis sets. *J. Chem. Phys.* **143**, 054107. doi:10.1063/1.4927476 (2015).

72. Piccardo, M., Penocchio, E., Puzzarini, C., Biczysko, M. & Barone, V. Semi-Experimental Equilibrium Structure Determinations by Employing B3LYP/SNSD Anharmonic Force Fields: Validation and Application to Semirigid Organic Molecules. *J. Phys. Chem. A* **119**, 2058. doi:10.1021/jp511432m (2015).
73. Kim, M.-C., Sim, E. & Burke, K. Understanding and Reducing Errors in Density Functional Calculations. *Phys. Rev. Lett.* **111**, 073003. doi:10.1103/PhysRevLett.111.073003 (2013).
74. Mezei, P. D., Csonka, G. I. & Kállay, M. Electron Density Errors and Density-Driven Exchange-Correlation Energy Errors in Approximate Density Functional Calculations. *J. Chem. Theory Comput.* **13**, 4753. doi:10.1021/acs.jctc.7b00550 (2017).
75. Gubler, M., Schäfer, M. R., Behler, J. & Goedecker, S. Accuracy of charge densities in electronic structure calculations. *J. Chem. Phys.* **162**, 094103. doi:10.1063/5.0251833 (2025).
76. Kanungo, B., Kaplan, A. D., Shahi, C., Gavini, V. & Perdew, J. P. Unconventional Error Cancellation Explains the Success of Hartree-Fock Density Functional Theory for Barrier Heights. *J. Phys. Chem. Lett.* **15**, 323. doi:10.1021/acs.jpcllett.3c03088 (2024).
77. Kaplan, A. D., Shahi, C., Sah, R. K., Bhetwal, P., Kanungo, B., Gavini, V. & Perdew, J. P. How Does HF-DFT Achieve Chemical Accuracy for Water Clusters? *J. Chem. Theory Comput.* **20**, 5517. doi:10.1021/acs.jctc.4c00560 (2024).
78. Medvedev, M. G., Bushmarinov, I. S., Sun, J., Perdew, J. P. & Lyssenko, K. A. Density functional theory is straying from the path toward the exact functional. *Science* **355**, 49. doi:10.1126/science.aah5975 (2017).
79. Bannwarth, C., Ehlert, S. & Grimme, S. GFN2-xTB—An Accurate and Broadly Parametrized Self-Consistent Tight-Binding Quantum Chemical Method with Multipole Electrostatics and Density-Dependent Dispersion Contributions. *J. Chem. Theory Comput.* **15**, 1652. doi:10.1021/acs.jctc.8b01176 (2019).
80. Ju, F. *et al.* *Acceleration without Disruption: DFT Software as a Service* 2024. doi:10.48550/arXiv.2406.11185.
81. Sun, Q. *et al.* PySCF: the Python-based simulations of chemistry framework. *WIREs Comput. Mol. Sci.* **8**, e1340. doi:10.1002/wcms.1340 (2018).
82. Scuseria, G. E. Linear Scaling Density Functional Calculations with Gaussian Orbitals. *J. Phys. Chem. A* **103**, 4782. doi:10.1021/jp990629s (1999).
83. Bahmann, H. & Kaupp, M. Efficient Self-Consistent Implementation of Local Hybrid Functionals. *J. Chem. Theory Comput.* **11**, 1540. doi:10.1021/ct501137x (2015).
84. Laqua, H., Kussmann, J. & Ochsenfeld, C. Efficient and Linear-Scaling Seminumerical Method for Local Hybrid Density Functionals. *J. Chem. Theory Comput.* **14**, 3451. doi:10.1021/acs.jctc.8b00062 (2018).
85. Kussmann, J., Laqua, H. & Ochsenfeld, C. Highly Efficient Resolution-of-Identity Density Functional Theory Calculations on Central and Graphics Processing Units. *J. Chem. Theory Comput.* **17**, 1512. doi:10.1021/acs.jctc.0c01252 (2021).
86. Kaupp, M., Wodyński, A., Arbuznikov, A. V., Fürst, S. & Schattenberg, C. J. Toward the Next Generation of Density Functionals: Escaping the Zero-Sum Game by Using the Exact-Exchange Energy Density. *Accounts Chem. Res.* **57**, 1815. doi:10.1021/acs.accounts.4c00209 (2024).
87. Furness, J. W., Kaplan, A. D., Ning, J., Perdew, J. P. & Sun, J. Accurate and Numerically Efficient r2SCAN Meta-Generalized Gradient Approximation. *J. Phys. Chem. Lett.* **11**, 8208. doi:10.1021/acs.jpcllett.0c02405 (2020).

7 Methods

Here we expand on details of the model architecture and the training data. The Supplementary Information contains further detailed information on the model (Sec. A), training details (Sec. B), training data (Sec. C), evaluation protocols (Sec. D) and additional results (Sec. E).

7.1 Skala: A model for scalable non-local representation learning

Skala’s enhancement factor in Eq. (1) is a non-local functional modeled with a deep neural network that takes as input a set of semi-local, density-dependent features $\mathbf{x}[\rho]$ from the standard meta-generalized-gradient approximation (meta-GGA) $O(N^3)$ rung, and which are represented on the aforementioned large irregular integration grid. The challenge here is to design an accurate XC functional that models intricate non-local interactions across the grid in order to achieve the accuracy that is often only attainable by more expensive functionals of a higher rung, while maintaining a computational cost comparable to functionals from the meta-GGA rung. While a naive solution with all-to-all communication across the grid would enable non-local representation learning, it is not a scalable design, since the cost of doing so on grids of the order of 10^4 to 10^6 points quickly grows out of control. Instead, Skala introduces a second coarse grid with far fewer points,⁸⁸ which acts as an intermediary layer through which the points on the finer grid can communicate.

Extended Data Fig. 6 shows the overall schematic of the neural network architecture. Starting from the input meta-GGA features, the 7 semi-local inputs are log-transformed, followed by a small multilayer perceptron (MLP) that acts strictly locally on each grid point. The MLP is applied twice, once to each spin-ordering of the transformed features, followed by an averaging operation. This yields a spin-symmetrized semi-local hidden representation that serves as input for the rest of the model. By making the hidden layer spin symmetric before feeding it through any non-local computation across the grid, we avoid having to run the more expensive part of the non-local neural network twice, saving computational cost.

Before the spin-symmetrized features are passed into the non-local interaction model, they are projected to a lower-dimensional hidden vector. Subsequently, the coarse points collect non-local information from the fine grid, analogous to the accumulation of multipole moments. More specifically, for each coarse point, the local hidden features on the integration grid are projected onto a product of radial basis functions and spherical harmonics that depend on the distance vector between the coarse and fine points, followed by an integration over space of all fine grid points. While one could consider further processing the coarsened features using message-passing layers on the coarse grid,⁸⁸ in preliminary experiments, we found this to lead to significant overfitting behavior. Instead, using the same product basis of radial and spherical components for each coarse point, we construct functions that when evaluated on the finer grid yield non-local hidden features on each fine grid point, which are invariant with respect to the Euclidean symmetry. In order to ensure that the non-local interaction between the coarse and fine points (and therefore also between the fine points) has a finite range, enabling the model to satisfy the size-consistency constraint, the radial basis functions are modulated by an envelope function⁸⁹ that smoothly decays to zero beyond 5 bohr.

Finally, the non-local hidden representations are concatenated with earlier semi-local hidden features, processed through a purely local MLP, and projected down to a scalar value per grid point. The scalar value is passed through a scaled sigmoid activation function with a range between 0 and 2,⁹⁰ yielding a bounded enhancement factor that enforces the Lieb-Oxford lower bound.⁹¹ The result is plugged into the discretized equivalent of Eq. (1) to yield the predicted $E_{xc}^\theta[\rho]$.

In Sec. A.5 we show that the hidden features on the coarse grid can be interpreted as multipole moments, and that the non-local module has the expressivity to model any two-body interaction. This could also be systematically increased to approximate any N-body interaction^{92,93} on the density grid to any desired accuracy. While in principle the non-local module has the ability to approximate non-local interactions independent of where the coarse points are placed, we take advantage of the structure of integration grids typically used in DFT — centered around the atomic centers — and place the coarsened points on the atomic centers. For more details on the neural network architecture, see Sec. A in the Supplementary Information.

7.2 Training data

Our training data comprise $\sim 150\text{k}$ reaction energies (Extended Data Table 1) computed at the CCSD(T)/CBS level of theory or higher, as detailed in Sec. C in the Supplementary Information. The largest subset of our training data (over half) is composed of $\sim 80\text{k}$ diverse total atomization energies for general molecules with up to five non-hydrogen atoms (MSR-ACC/TAE). Molecular structures from this dataset consisting of a single stable molecular fragment (90.7%) are released as the MSR-ACC/TAE25 dataset, described in Ehlert *et al.*⁹⁴

We extend the training data on total atomization energies with 14 publicly available linear and cyclic carbon clusters,⁹⁵ and we further add total atomic energies to the training data to gauge total energies.

To this large thermochemistry dataset, we add smaller datasets that provide initial coverage of reaction kinetics, basic properties, and both intra- and intermolecular non-covalent interactions. For the last category, we draw on the relatively abundant publicly available data and select four datasets from the NCIAtlas collection (D442x10, SH250x10, R739x5, HB300SPXx10).^{96–100} The remainder of this first batch of training data was generated in-house, as detailed in Sec. C. To begin coverage of basic properties, we include atomic datasets of electron affinities (EAs) and ionization potentials (IPs) — including double and triple IPs — for elements up to argon, as well as proton affinities (MSR-ACC/PA) and ionization potentials (MSR-ACC/IP) for the molecules in the MSR-ACC/TAE dataset. For conformational energies, the MSR-ACC/Conf dataset includes all conformers within a 10 kcal/mol energy window of the molecules in MSR-ACC/TAE. To start covering kinetics, the MSR-ACC/Reactions dataset comprises elementary steps of reactions of small organic molecules with up to eight atoms, including both transition states and endpoints along the reaction pathways.

From all these datasets, we removed the overlap with the test sets GMTKN55¹⁰¹ and W4-17¹⁰² based on the molecular graphs of all systems with more than two atoms. We determine molecular graphs (with undetermined bond order) from the bond model of GFN-FF¹⁰³ and we subtract W4-17 from the training data by removing all reactions that contain any molecule that contains any covalently connected subgraph found in any molecule in W4-17 (some molecules in W4-17 are not recognized as fully connected by GFN-FF). Similarly, we subtract GMTKN55 from the training data by removing all reactions that share the same set of molecules (defined by the GFN-FF graph) with the same stoichiometric ratios. This prevents any leakage of W4-17 into the trained model and minimizes the leakage of GMTKN55. After the test sets subtraction, 1% of MSR-ACC/TAE consisting of a single stable molecular fragment is further reserved for validation as a holdout set. Both the holdout and training splits of MSR-ACC/TAE25 are released as part of Ehlert *et al.*⁹⁴

As explained in Sec. 2, in the pre-training phase we evaluate our model at fixed densities using B3LYP^{104,105} in a def2-QZVP basis set,¹⁰⁶ or with a ma-def2-QZVP basis set¹⁰⁷ if the molecule is part of a dataset that contains strongly localized anions. Using the fixed densities, we compute the relative energy of a reaction from the B3LYP total energies by replacing the B3LYP XC energies with the XC energies predicted with our functional. To regularize the trained model with respect to numerical variations on the grid, we use eight distinct integration grids, using level 2 and level 3 from PySCF¹⁰⁸ with four different angular integration schemes.

7.3 Data availability

The training data is summarized in Extended Data Table 1. Molecular structures from the in-house generated MSR-ACC/TAE dataset consisting of a single stable molecular fragment (90.7% of the total size of MSR-ACC/TAE) are released publicly as the MSR-ACC/TAE25 dataset, described in Ehlert *et al.*⁹⁴. The in-house generated datasets MSR-ACC/Conf, MSR-ACC/PA, MSR-ACC/IP, MSR-ACC/Reactions are not released publicly, but detailed information on their generation protocol is given in Sec.7.2 and Sec.C. The W4-CC⁹⁵, D442x10¹⁰⁰, SH250x10⁹⁹, R739x5⁹⁸, and HB300SPXx10⁹⁶ are all publicly available datasets.

The evaluation benchmark sets W4-17¹⁰² and GMTKN55¹⁰¹, the dipole moment evaluation dataset¹⁰⁹, and the geometry optimization datasets LMGB35,¹¹⁰ HMGB11,¹¹⁰ and CCse21¹¹¹ are all publicly available. The molecular structures for the computational cost results are described in Sec. D.1 in Fig. 8, and are collected from the following publicly available sources: Grimme,¹¹² S30L,¹¹³ HS13L,¹¹⁴ and NCI16L.¹¹⁵

7.4 Code availability

The Skala model and inference code are available under MIT license at <https://github.com/microsoft/skala>. The repository contains the PyTorch implementation of the Skala model and its hookups to quantum chemistry packages PySCF¹⁰⁸, GPU4PySCF and ASE¹¹⁶. The Skala model is also served in Azure AI Foundry at <https://ai.azure.com/catalog/models/Skala>, where the SCF evaluation is implemented using Accelerated DFT¹¹⁷ (inference on GPU) and GauXC^{118–120}.

Acknowledgments

We thank Maik Riechert, Hannes Schulz and Eray Inanc for supporting our engineering infrastructure and Kenji Takeda and the Microsoft Accelerator team for their crucial role in designing and executing our data generation campaign. Furthermore, we are grateful for feedback and support from Gregor Simm, Marwin Segler, Frank Noé, Jia Zhang, Bonnie Kruft, Rachel Howard, Rosa de Rosa and Bev Baker. We also thank Jan Gerit Brandenburg, Nicola Marzari and John P. Perdew for insightful feedback on an earlier version of this manuscript.

3D visualizations in this paper were rendered with Mitsuba 3.¹²¹

Author contributions

Conceptualization: C.-W.H., G.L., T.V., D.P.K., S.E., K.J.H.G., J.H., R.v.d.B., P.G.-G. Methodology: G.L., C.-W.H., T.V., D.P.K., S.E., B.M., S.-O.K., J.H., R.v.d.B., P.G.-G. Software: T.V., C.-W.H., G.L., D.P.K., S.E., S.L., J.H., R.v.d.B., D.G., X.W., L.H., R.C.Z., Ab.K., K.J.H.G. Validation: D.P.K., C.-W.H., T.V., G.L., S.E., J.H., R.v.d.B. Formal analysis: C.-W.H., T.V., G.L., D.P.K., K.J.H.G., S.E., J.H., R.v.d.B. Investigation: C.-W.H., T.V., G.L., D.P.K., S.E., J.H., R.v.d.B., P.G.-G., D.G., Y.C., D.B.W.-Y., Ab.K., K.J.H.G., M.S., W.B. Resources: C.M.B., D.G. Data generation & curation: J.H., S.E., D.P.K., Am.K., S.L., J.G.T., K.J.H.G., C.-W.H., G.L., T.V., R.v.d.B., P.G.-G. Writing - Original Draft: G.L., C.-W.H., T.V., D.P.K., S.E., K.J.H.G., J.H., R.v.d.B., and P.G.-G. Writing - Review & Editing: G.L., C.-W.H., T.V., C.M.B., J.H., R.v.d.B., and P.G.-G. Visualization: T.V., C.-W.H., S.E., D.P.K., W.B., M.S., R.v.d.B. Supervision: J.H., R.v.d.B., and P.G.-G. Project administration: R.S.

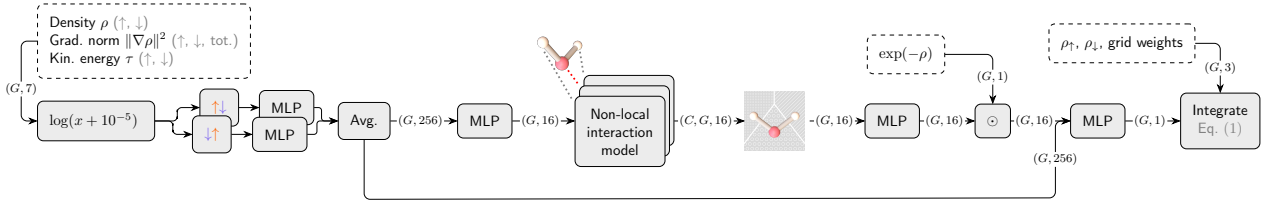
Competing interests

All authors declare employment by Microsoft while engaged in the research for this manuscript. G.L., C.-W.H., T.V., D.P.K., S.E., S.L., K.J.H.G., D.G., M.S., W.B., R.S., J.H., R.v.d.B., and P.G.-G. declare a filed patent application for the model and training pipeline in this article.

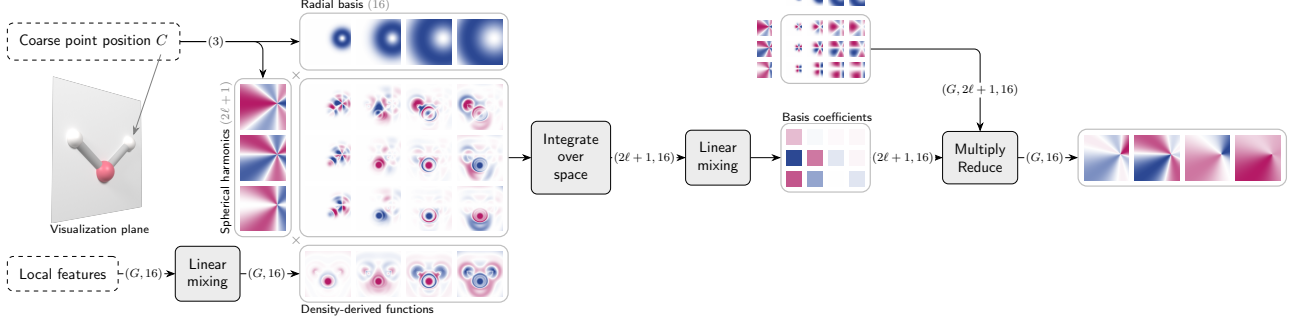
Method References

88. Gao, N., Eberhard, E. & Günnemann, S. *Learning Equivariant Non-Local Electron Density Functionals* 2024. <http://arxiv.org/abs/2410.07972>.
89. Gasteiger, J., Groß, J. & Günnemann, S. *Directional Message Passing for Molecular Graphs* 2022. doi:10.48550/arXiv.2003.03123.
90. Kirkpatrick, J. *et al.* Pushing the frontiers of density functionals by solving the fractional electron problem. *Science* **374**, 1385. doi:10.1126/science.abj6511 (2021).
91. Lieb, E. H. A lower bound for Coulomb energies. *Phys. Lett. A* **70**, 444. doi:10.1016/0375-9601(79)90358-X (1979).
92. Dusson, G., Bachmayr, M., Csanyi, G., Drautz, R., Etter, S., Oord, C. v. d. & Ortner, C. *Atomic Cluster Expansion: Completeness, Efficiency and Stability* 2021. doi:10.48550/arXiv.1911.03550.
93. Batatia, I., Kovacs, D. P., Simm, G., Ortner, C. & Csanyi, G. *MACE: Higher Order Equivariant Message Passing Neural Networks for Fast and Accurate Force Fields in Advances in Neural Information Processing Systems* (Curran Associates, Inc., 2022) (eds Koyejo, S., Mohamed, S., Agarwal, A., Belgrave, D., Cho, K. & Oh, A.) **35** (), 11423–11436. https://proceedings.neurips.cc/paper_files/paper/2022/file/4a36c3c51af11ed9f34615b81edb5bbc-Paper-Conference.pdf.
94. Ehlert, S. *et al.* *Accurate Chemistry Collection: Coupled cluster atomization energies for broad chemical space* 2025. doi:10.48550/arXiv.2506.14492.
95. Karton, A., Tarnopolsky, A. & M.L. Martin, J. Atomization energies of the carbon clusters C_n (n = 2–10) revisited by means of W4 theory as well as density functional, Gn, and CBS methods. *Mol. Phys.* **107**, 977. doi:10.1080/00268970802708959 (2009).
96. Řezáč, J. Non-Covalent Interactions Atlas Benchmark Data Sets 2: Hydrogen Bonding in an Extended Chemical Space. *J. Chem. Theory Comput.* **16**, 6305. doi:10.1021/acs.jctc.0c00715 (2020).
97. Řezáč, J. Non-Covalent Interactions Atlas Benchmark Data Sets: Hydrogen Bonding. *J. Chem. Theory Comput.* **16**, 2355. doi:10.1021/acs.jctc.9b01265 (2020).
98. Kříž, K., Nováček, M. & Řezáč, J. Non-Covalent Interactions Atlas Benchmark Data Sets 3: Repulsive Contacts. *J. Chem. Theory Comput.* **17**, 1548. doi:10.1021/acs.jctc.0c01341 (2021).
99. Kříž, K. & Řezáč, J. Non-covalent interactions atlas benchmark data sets 4: σ -hole interactions. *Phys. Chem. Chem. Phys.* **24**, 14794. doi:10.1039/D2CP01600A (2022).
100. Řezáč, J. Non-Covalent Interactions Atlas benchmark data sets 5: London dispersion in an extended chemical space. *Phys. Chem. Chem. Phys.* **24**, 14780. doi:10.1039/D2CP01602H (2022).
101. Goerigk, L., Hansen, A., Bauer, C., Ehrlich, S., Najibi, A. & Grimme, S. A look at the density functional theory zoo with the advanced GMTKN55 database for general main group thermochemistry, kinetics and noncovalent interactions. *Phys. Chem. Chem. Phys.* **19**, 32184. doi:10.1039/c7cp04913g (2017).

102. Karton, A., Sylvetsky, N. & Martin, J. M. L. W4-17: A diverse and high-confidence dataset of atomization energies for benchmarking high-level electronic structure methods. *J. Comput. Chem.* **38**, 2063. doi:10.1002/jcc.24854 (2017).
103. Spicher, S. & Grimme, S. Robust Atomistic Modeling of Materials, Organometallic, and Biochemical Systems. *Angewandte Chemie Int. Ed.* **59**, 15665. doi:10.1002/anie.202004239 (2020).
104. Becke, A. D. Density-functional thermochemistry. III. The role of exact exchange. *J. Chem. Phys.* **98**, 5648. doi:10.1063/1.464913 (1993).
105. Stephens, P. J., Devlin, F. J., Chabalowski, C. F. & Frisch, M. J. Ab Initio Calculation of Vibrational Absorption and Circular Dichroism Spectra Using Density Functional Force Fields. *J. Phys. Chem.* **98**, 11623. doi:10.1021/j100096a001 (1994).
106. Weigend, F. & Ahlrichs, R. Balanced basis sets of split valence, triple zeta valence and quadruple zeta valence quality for H to Rn: Design and assessment of accuracy. *Phys. Chem. Chem. Phys.* **7**, 3297. doi:10.1039/B508541A (2005).
107. Zheng, J., Xu, X. & Truhlar, D. G. Minimally augmented Karlsruhe basis sets. *Theor. Chem. Accounts* **128**, 295. doi:10.1007/s00214-010-0846-z (2011).
108. Sun, Q. *et al.* PySCF: the Python-based simulations of chemistry framework. *WIREs Comput. Mol. Sci.* **8**, e1340. doi:10.1002/wcms.1340 (2018).
109. Hait, D. & Head-Gordon, M. How accurate are static polarizability predictions from density functional theory? An assessment over 132 species at equilibrium geometry. *Phys. Chem. Chem. Phys.* **20**, 19800. doi:10.1039/C8CP03569E (2018).
110. Grimme, S., Brandenburg, J. G., Bannwarth, C. & Hansen, A. Consistent structures and interactions by density functional theory with small atomic orbital basis sets. *J. Chem. Phys.* **143**, 054107. doi:10.1063/1.4927476 (2015).
111. Piccardo, M., Penocchio, E., Puzzarini, C., Biczysko, M. & Barone, V. Semi-Experimental Equilibrium Structure Determinations by Employing B3LYP/SNSD Anharmonic Force Fields: Validation and Application to Semirigid Organic Molecules. *J. Phys. Chem. A* **119**, 2058. doi:10.1021/jp511432m (2015).
112. Grimme, S. Exploration of Chemical Compound, Conformer, and Reaction Space with Meta-Dynamics Simulations Based on Tight-Binding Quantum Chemical Calculations. *J. Chem. Theory Comput.* **15**, 2847. doi:10.1021/acs.jctc.9b00143 (2019).
113. Sure, R. & Grimme, S. Comprehensive Benchmark of Association (Free) Energies of Realistic Host–Guest Complexes. *J. Chem. Theory Comput.* **11**, 3785. doi:10.1021/acs.jctc.5b00296 (2015).
114. Gorges, J., Grimme, S. & Hansen, A. Reliable prediction of association (free) energies of supramolecular complexes with heavy main group elements – the HS13L benchmark set. *Phys. Chem. Chem. Phys.* **24**, 28831. doi:10.1039/D2CP04049B (2022).
115. Gorges, J., Baendorf, B., Grimme, S. & Hansen, A. Efficient computation of the interaction energies of very large non-covalently bound complexes. *Synlett* **34**, 1135. doi:10.1055/s-0042-1753141 (2023).
116. Hjorth Larsen, A. *et al.* The atomic simulation environment—a Python library for working with atoms. *J. Physics: Condens. Matter* **29**, 273002. doi:10.1088/1361-648X/aa680e (2017).
117. Ju, F. *et al.* *Acceleration without Disruption: DFT Software as a Service* 2024. doi:10.48550/arXiv.2406.11185.
118. Petrone, A., Williams-Young, D. B., Sun, S., Stetina, T. F. & Li, X. An efficient implementation of two-component relativistic density functional theory with torque-free auxiliary variables. *Eur. Phys. J. B* **91**, 169. doi:10.1140/epjb/e2018-90170-1 (2018).
119. Williams-Young, D. B., de Jong, W. A., van Dam, H. J. J. & Yang, C. On the Efficient Evaluation of the Exchange Correlation Potential on Graphics Processing Unit Clusters. *Front. Chem.* **8**. doi:10.3389/fchem.2020.581058 (2020).
120. Williams-Young, D. B., Asadchev, A., Popovici, D. T., Clark, D., Waldrop, J., Windus, T. L., Valeev, E. F. & de Jong, W. A. Distributed memory, GPU accelerated Fock construction for hybrid, Gaussian basis density functional theory. *J. Chem. Phys.* **158**, 234104. doi:10.1063/5.0151070 (2023).
121. Jakob, W., Speierer, S., Roussel, N., Nimier-David, M., Vicini, D., Zeltner, T., Nicolet, B., Crespo, M., Leroy, V. & Zhang, Z. *Mitsuba 3 renderer* 2022.
122. Karton, A., Daon, S. & Martin, J. M. W4-11: A high-confidence benchmark dataset for computational thermochemistry derived from first-principles W4 data. *Chem. Phys. Lett.* **510**, 165. doi:10.1016/j.cplett.2011.05.007 (2011).



(a) Skala architecture overview



(b) Non-local interaction model

Extended Data Figure 6: Skala’s architecture (a): Overview of the architecture modules. G is the size of the DFT integration grid, and C is the number of coarse points. We log-transform 7 meta-GGA features, apply the same MLP to both spin-orderings, and average to generate spin-order invariant hidden features. After local processing, a non-local interaction model is applied between grid points. These interactions, detailed in (b), are centered around coarse points aligned with nuclei positions and reassembled via soft partitioning. Local and non-local features are fed into a final MLP that produces an enhancement factor, multiplied with a scale-function based on the local density, and integrated over the grid to obtain E_{xc}^{θ} . (b): The non-local interaction model. While Skala uses only meta-GGA features, it models non-local effects with communication between grid points indirectly through selected coarse points. For each coarse point and spherical harmonic level $\ell = 0, 1, 2, 3$, local grid features are treated as functions and multiplied pointwise by $2\ell + 1$ spherical harmonics and 16 radial basis functions. The products are integrated and then linearly mixed to allow interactions between radial basis functions. For each radial basis function, the mixed coarsened features become coefficients for the spherical harmonic basis, producing new grid-represented functions that capture non-local interactions. These 16 functions, with spherical frequency of order ℓ , are combined across orders and reassembled via distance-based soft partitioning as shown in (a).

Extended Data Table 1: Training datasets. The table shows the original number of labels and the number of training labels after subtraction of the overlap with the test sets GMTKN55 and W4-17 and splitting off any validation sets.

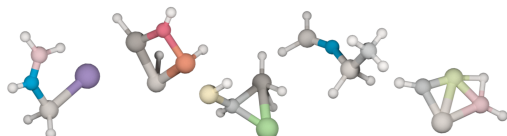
Dataset	Number of reactions			Avg. E [kcal/mol]	Elements	Description
	<i>Full</i>	<i>Training</i>				
MSR-ACC/						
TAE	80549	78650	(97.6%)	539.76	H, Li-F, Na-Cl	Total atomization energies
Conf	34021	33795	(99.3%)	1.68	H, Li-F, Na-Cl	Conformational energies
PA	10226	9961	(97.4%)	222.68	H, Li-F, Na-Cl	Proton affinities
IP	9962	9677	(97.1%)	164.82	H, Li-F, Na-Cl	Ionization potentials
Reactions	4964	3709	(74.7%)	40.63	H, C-O	Reaction paths
Atomic/						
TOT	16	16	(100.0%)	—	H-He, B-Ar	Atomic total energies
EA	11	11	(100.0%)	33.58	H, B-C, O-F, Na, Al-Cl	Atomic electron affinities
IP	43	43	(100.0%)	667.19	He, B-Ar	Atomic ionization potentials
W4-CC	14	14	(100.0%)	745.11	C	Total atomization energies of carbon clusters
NCIAtlas/						
D442x10	4420	4368	(98.8%)	1.38	H-He, B-Ne, P-Ar, Br-Kr, I-Xe	Dispersion interactions
R739x5	3695	3435	(93.0%)	1.09	H-He, B-Ne, P-Ar, Br-Kr, I-Xe	Repulsive contacts
HB300SPXx10	3000	2990	(99.7%)	3.18	H, C-F, P-Cl, Br, I	Hydrogen bonds
SH250x10	2500	2410	(96.4%)	3.99	H, C-F, P-Cl, As-Br, I	Sigma-hole contacts
Total	153421	149079	(97.2%)		H-Ar, As-Kr, I-Xe	

	W4-17	W4-17	GMTKN55
	(full)	(single ref.)	
	[MAE]	[MAE]	[WTMAD-2]
revPBE	8.05	7.22	8.34
r ² SCAN	4.46	3.84	7.25
B97M-V	2.84	2.52	5.56
B3LYP	3.80	3.73	6.38
M06-2X	3.01	2.39	4.83
ω B97X-V	2.59	2.14	3.96
ω B97M-V	2.04	1.66	3.23
Skala	1.06	0.85	3.89

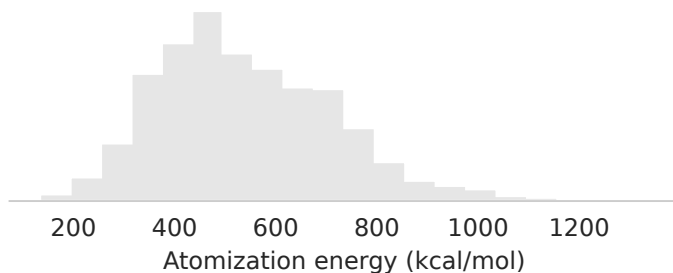
(a)

Functional	MAE on the MSR-ACC/TAE25 holdout set [kcal/mol]
revPBE	6.69
r ² SCAN	6.77
B97M-V	10.23
B3LYP	4.42
M06-2X	3.76
ω B97X-V	5.12
ω B97M-V	4.34
Skala	0.35
Label quality	0.49 (estimated as avg. error of W1-F12 w.r.t. W4)

(b)



(c)



(d)

Extended Data Figure 7: Errors for reaction energies. (a) Shows the errors (in kcal/mol) on W4-17 and GMTKN55, corresponding to the numbers in the plot in Fig. 1. For W4-17, the table shows both the MAE on the full set as well as on the set of 183 single-reference structures with %TAE[(T)] < 10%.¹²² (b) Displays the errors on the MSR-ACC/TAE25 holdout set. The estimated quality of the W1-F12 labels used in MSR-ACC/TAE25 is computed as the error of W1-F12 against the more accurate W4 protocol on the single-reference subset of W4-17. The estimate is conservative because the W4-17 subset was created with a \sim 10% cutoff in %TAE[(T)], while MSR-ACC/TAE25 has a cutoff of 6% in %TAE[(T)]. The MSR-ACC/TAE25 holdout set has the same distribution as part of our training set, but none of its molecules are used for training. Panel (c) displays example molecules and panel (d) shows the distribution of total atomization energies in this set.

Supplementary information: Accurate and scalable exchange-correlation with deep learning

Table of contents

A	Modeling the exchange-correlation functional	23
A.1	In theory	23
A.2	In practice	23
A.3	Neural network architecture	24
A.4	Non-local interaction through coarse points	25
A.5	Intuition on the structure of the non-local layer	26
A.6	Related work	28
B	Training details	28
B.1	Training objective	28
B.2	Parameter initialization	29
B.3	Optimization	29
B.4	Self-consistent fine-tuning	29
C	Training data: computational details	30
C.1	MSR-ACC/TAE dataset	30
C.2	MSR-ACC/IP, /PA, /Conf, and /Reactions datasets	30
C.3	Atomic datasets	30
C.4	3rd-party public datasets	30
C.5	Density features on the grid	31
D	Evaluation protocols	31
D.1	Evaluation sets	31
D.2	Baselines and dispersion correction settings	31
D.3	Basis sets	31
D.4	SCF retry protocol	31
D.5	SCF with orbital gradient descent fallback	32
D.6	Geometry optimization: implementation	33
D.7	Computational cost: GPU and CPU implementation	34
E	Additional results	34
E.1	Spin-symmetry broken solutions for multi-reference systems	34
E.2	GMTKN55 benchmark	36
E.3	Convergence with respect to the grid size	39
E.4	Computational cost on GPU for exchange correlation energy and electron repulsion integrals	39
E.5	Emergence of exact constraints with more training data	40

A Modeling the exchange-correlation functional

In this section we summarize how we model the exchange-correlation functional. We describe the input features and the architecture.

A.1 In theory

The foundation of DFT is built on the insight that the ground-state energy of a many-electron system can, in principle, be expressed as a functional of the electron density alone. As explained in Sec. 2 in the main body of the paper, such functional of the electron density has an unknown component, the exchange-correlation part. Following the Kohn-Sham formalism,¹²³ the ground-state energy of a many-electron system in a static potential v can be written as

$$E = \min_{\rho} E_{\text{tot}}[\rho], \quad E_{\text{tot}}[\rho] = \int v(r)\rho(r) dr + \frac{1}{2} \int \int \frac{\rho(r)\rho(r')}{|r-r'|} dr dr' + T_s[\rho] + E_{\text{xc}}[\rho], \quad (2)$$

where $v(r)$ in the first term is the external potential due to the nuclei, the second term is the Hartree electrostatic energy, $T_s[\rho]$ is the kinetic energy of a system of non-interacting electrons with density ρ and $E_{\text{xc}}[\rho]$ is the exchange-correlation energy of an interacting system with density ρ .¹²³ The expression of E_{xc} is unknown and the central challenge becomes then to find an accurate description for it. E_{xc} is a functional of the electron density, meaning that we can define it as $E_{\text{xc}} : L^1(\mathbb{R}^3) \rightarrow \mathbb{R}$. E_{xc} takes a density ρ as input and it outputs a scalar $E_{\text{xc}}[\rho]$. There exists many different ways to produce an approximation. Many ML and traditional functionals represent the E_{xc} as an integral of an energy density, as follows:

$$E_{\text{xc}}^{\theta}[\rho] = -\frac{3}{4} \left(\frac{6}{\pi}\right)^{\frac{1}{3}} \int \left(\rho^{(\uparrow)}(r)^{4/3} + \rho^{(\downarrow)}(r)^{4/3}\right) f_{\theta}[\mathbf{x}[\rho]](r) dr, \quad (3)$$

where f_{θ} is a learnable function of a set of features $\mathbf{x}[\rho]$ called the *enhancement factor*. When $f_{\theta} = 1$, the remaining terms reduce to the Local Density Approximation (LDA) exchange functional.¹²⁴ In Skala, the enhancement factor f_{θ} is parameterized by a deep neural network, whose architecture is explained in detail in Sec. A.3. This particular form of E_{xc} , written as a learnable enhancement factor times the LDA exchange energy density, is mainly designed to make it easier to enforce properties that the exact E_{xc} functional is known to satisfy, such as the high-density uniform coordinate scaling, size consistency, and the Lieb-Oxford lower bound.¹²⁵

A.2 In practice

Theoretically, the density ρ is a function $\mathbb{R}^3 \rightarrow \mathbb{R}$. However, in practice, we work with a discretized version. Similar to Ref. [126–130], we choose to discretize the density features by evaluating them on a set of points $\{r_i \in \mathbb{R}^3, i = 1, \dots, G\}$ that are defined by a classical integration grid. An integration grid is a set of points $r_i \in \mathbb{R}^3$ (effectively, a point cloud in \mathbb{R}^3) and associated weights $w_i \in \mathbb{R}$ used to numerically approximate spatial integrals, such as the exchange-correlation energy and its potential. We refer to Ref. [131–133] for details on such integration grids. This representation of the density evaluated on a point cloud in \mathbb{R}^3 has the advantage of being independent of the basis set.

Following the discretization, E_{xc} is therefore approximated as

$$E_{\text{xc}}[\rho] \approx -\frac{3}{4} \left(\frac{6}{\pi}\right)^{\frac{1}{3}} \sum_{i=1}^G \left(\rho^{(\uparrow)}(r_i)^{4/3} + \rho^{(\downarrow)}(r_i)^{4/3}\right) f_{\theta}[\mathbf{x}[\rho]](r_i) w_i. \quad (4)$$

In our setting, we pick the following set of features $\mathbf{x}[\rho]$:

$$\mathbf{x}[\rho](r_i) = \left[\rho^{(\uparrow)}(r_i), \rho^{(\downarrow)}(r_i), \left\| \nabla \rho^{(\uparrow)}(r_i) \right\|^2, \left\| \nabla \rho^{(\downarrow)}(r_i) \right\|^2, \tau^{(\uparrow)}(r_i), \tau^{(\downarrow)}(r_i), \left\| \nabla \rho^{(\uparrow)}(r_i) + \nabla \rho^{(\downarrow)}(r_i) \right\|^2 \right], \quad (5)$$

where τ denotes the Kohn-Sham kinetic energy density and the \uparrow and \downarrow denote the two spin channels. Such features are standard semi-local features used in meta-GGA functionals.¹³⁴ Effectively, the input $\mathbf{x}[\rho]$ of the neural network is then a tensor in $\mathbb{R}^{G \times 7}$, where G typically depends on system size. These input features are called semi-local, because they only collect information at each given grid point. It is known that the exact functional cannot be captured with an enhancement factor that is just a function of semi-local features. It must also have a non-local dependence on the density.

Analyzing the expression of the enhancement factor $f_{\theta}[\mathbf{x}[\rho]]$, it is clear that there are two separate strategies to incorporate such non-local information on the density ρ :

- including extra hand-designed features in the set $\mathbf{x}[\rho]$ that capture in each grid point information from density features at other distant points, as it is done by adding exchange-like features¹²⁹ or convolved features;^{135,136} this is in the spirit of climbing Jacob’s ladder.
- keeping the set of features as in Eq. (5) and allowing the model f_θ to *learn* longer range dependencies and mix information across different points.

We take on the second approach, which is a step away from traditional DFT approaches built on Jacob’s ladder or other hand-designed features and gears towards inferring non-locality through data and the model. Among non-local effects, dispersion is very long-range and traditional functionals do not model it directly. Instead, post-correction is typically applied. As we train on B3LYP densities, we train with its D3 correction^{137,138} as part of the total energy, and focus on learning the other shorter-range non-local effects.

A.3 Neural network architecture

In this section, we give an overview of the functional architecture used to parameterize the enhancement factor f_θ in Eq. (3). We work with features on a finite grid, and use subscripts i , j , and k to refer to specific coordinates. For example, ρ_i is the density feature evaluated on grid point r_i , i.e. $\rho(r_i)$. The 7 semi-local features introduced in Eq. (5) are first processed as follows:

$$x_i^{(\uparrow, \downarrow)} = \log \left(\left[\rho_i^{(\uparrow)}, \rho_i^{(\downarrow)}, \left\| \nabla \rho_i^{(\uparrow)} \right\|^2, \left\| \nabla \rho_i^{(\downarrow)} \right\|^2, \tau_i^{(\uparrow)}, \tau_i^{(\downarrow)}, \left\| \nabla \rho_i^{(\uparrow)} + \nabla \rho_i^{(\downarrow)} \right\|^2 \right] + \epsilon \right) \quad (6)$$

where the arrows refer to the respective spin channels, (\uparrow, \downarrow) in x_i emphasizes the ordering of the spin in the input vector and ϵ is a small constant to ensure numerical stability that in our setting is equal to 10^{-5} .

Our architecture is mainly comprised of three parts.

Part one. The first part is an input representation extractor

$$f_{\text{repr}}(x) = \sigma(W_2 \sigma(W_1 x + b_1) + b_2), \quad (7)$$

where W_1 and b_1 represent the first linear layer that projects the input vector x onto a higher dimensional space $\mathbb{R}^{D_{\text{hid}}}$, followed by a Swish activation function¹³⁹ σ and another fully-connected layer with parameters W_2 and b_2 . We evaluate the representation model twice on each grid point, changing the ordering of the spin channels in the input features, and then average the two, in order to obtain a feature vector that is invariant to the ordering of spin channels:

$$h_i = \frac{f_{\text{repr}}(x_i^{(\uparrow, \downarrow)}) + f_{\text{repr}}(x_i^{(\downarrow, \uparrow)})}{2}. \quad (8)$$

Part two. The second part processes these features via a non-local layer and obtain a D_{nonl} -dimensional non-local feature:

$$h_{\text{nonl}, i} = f_{\text{nonl}}(h_i, \{R_j\}) \quad (9)$$

where $\{R_j\}$ is a set of assisting coordinates used. We will elaborate on the choice of $\{R_j\}$ and the precise structure of f_{nonl} in detail in Sec. A.4.

Part three. The third component of the architecture is an output model concatenating h_i and $h_{\text{nonl}, i}$ and mapping it through another MLP to produce the enhancement factor

$$h_{\text{enh}, i} = \sigma_{\text{out}}(W_6 \cdots \sigma(W_3[h_i, h_{\text{nonl}, i}] + b_3) \cdots + b_6). \quad (10)$$

Here W_3 is a $D_{\text{hid}} \times (D_{\text{hid}} + D_{\text{nonl}})$ matrix, W_4 and W_5 are both $D_{\text{hid}} \times D_{\text{hid}}$, and W_6 is $1 \times D_{\text{hid}}$, mapping to a scalar. The biases are all conformable to their corresponding weights. The last activation function of the output model is a scaled sigmoid function centered around one: $\sigma_{\text{out}}(x) = \frac{2}{1 + \exp(-x/2)}$. This ensures if the logit is close to zero, the final integration is close to the LDA exchange, as we multiply the enhancement factor with the LDA exchange energy density to obtain the final exchange-correlation energy

$$E_{\text{xc}}[\rho] = -\frac{3}{4} \left(\frac{6}{\pi} \right)^{\frac{1}{3}} \sum_{i=1}^G h_{\text{enh}, i} \left(\rho_i^{(\uparrow) 4/3} + \rho_i^{(\downarrow) 4/3} \right) w_i \quad (11)$$

where w_i is the integration grid weight. The $f_\theta[\mathbf{x}[\rho]](r_i)$ in Eq. (4) is then $h_{\text{enh}, i}$ and the parameters θ denote all the learnable parameters in the architecture described above.

In all our experiments, we set $D_{\text{hid}} = 256$ and $D_{\text{nonl}} = 16$.

A.4 Non-local interaction through coarse points

In this section we expand on the structure of the non-local layer, sketched in Eq. (9). Due to the large number of integration grid points, it is computationally prohibitive to let all the grid points communicate with each other. In this section, we introduce a mechanism to pass on non-local information with the aid of some chosen helper nodes referred to as coarse points. The information coarsening step is akin to accumulating multipole moments. We will discuss this relation formally in the next section.

There are two sets of points that play a role in the exchange of non-local information: the set of points of the integration grid (the same ones on which we evaluate the input features) and the set of coarse points that are used as helpers. We use the term ‘‘downsampling’’ to refer to the operations that send messages from the integration grid points to the coarse points, which reduces the dimensionality. We call it ‘‘upsampling’’ when sending messages back from the coarse points to the integration grid points, which increases the dimensionality.

Pre-downsampling transform: As the non-local interaction is the computational bottleneck, we first project the local features onto a lower-dimensional vector which is cheaper to manipulate. We define

$$h_{\text{pre-down},i} = \sigma(W_{\text{pre-down}}h_i + b_{\text{pre-down}}), \quad (12)$$

where the weight $W_{\text{pre-down}}$ is $D_{\text{nonl}} \times D_{\text{hid}}$. We maintain the dimensionality $D_{\text{hid}} = 16$ throughout the non-local component.

Downsampling: Let R_j be the coordinates of a coarse point. We define the coarsened feature of order ℓ in the c 's channel as a $2\ell + 1$ -dimensional vector

$$H_{j\ell c} = \sum_k \phi_c(\|r_{jk}\|) Y_\ell(\widehat{r}_{jk}) \sum_{c'} W_{\text{down},\ell cc'} h_{\text{pre-down},kc'} w_k \quad (13)$$

where $r_{jk} = R_j - r_k$, $\widehat{r} = r/\|r\|$, Y_ℓ are the spherical harmonics, and ϕ_c is a radial basis function described in Eq. (18). R_j is a coarse point on which we summarize the local density features. In practice, we choose them to be located at the atomic centers, and let j be the atomic index. This expansion first projects the local scalar feature $h_{\text{pre-down},kc'}$ onto the product basis $\phi_c Y_\ell$ (with a learnable weight per tensor order ℓ , which mixes the channels), and is followed by an aggregation step that sums up the messages sent by all integration grid points k to the coarse point j . The resulting feature $H_{j\ell c}$ is a feature on the coarse point j which transforms equivariantly according to the rotation of the input grid points and coarse points. The spherical tensor order ℓ ranges from 0 to ℓ_{max} . We use $\ell_{\text{max}} = 3$ in the paper.

Upsampling: Next, we send the message back from the coarse points to the integration grid points via

$$h'_{ic} = \sum_j \sum_\ell \phi_c(\|r_{ij}\|) \left\langle Y_\ell(\widehat{r}_{ij}), \sum_{c'} W_{\text{up},\ell cc'} H_{j\ell c'} \right\rangle \pi_{ij} \quad (14)$$

where again $r_{ij} = r_i - R_j$ and π_{ij} is defined as follows:

$$\pi_{ij} = \frac{\tilde{\pi}(r_{ij}, r_{\text{max}})}{\sum_{j'} \tilde{\pi}(r_{ij'}, r_{\text{max}}) + 0.1}, \quad (15)$$

with $\tilde{\pi}(\cdot, r_{\text{max}}) : \mathbb{R} \rightarrow \mathbb{R}$ being a function that smoothly turns off interactions beyond a certain cutoff. In $\tilde{\pi}(r, r_{\text{max}})$, the input r is first divided by the cutoff r_{max} , clamped to the interval $[0, 1]$ and then processed through the following piecewise function:

$$\begin{cases} 1 - 2r^2, & \text{if } r < 0.5 \\ 2r^2 - 4r + 2 & \text{if } r \geq 0.5. \end{cases} \quad (16)$$

Post-upsampling transform: After the message is sent back, we postprocess it with

$$h_{\text{post-up},i} = \sigma(W_{\text{post-up}}h'_i + b_{\text{post-up}}) \quad \text{and} \quad h_{\text{nonl},i} = \exp(-\rho_i)h_{\text{post-up},i} \quad (17)$$

where $W_{\text{post-up}}$ is $D_{\text{nonl}} \times D_{\text{nonl}}$ and $\exp(-\rho_i)$ is imposed to suppress non-local effects on grid points with higher density values, such as regions near the nuclei, as an inductive bias.

Radial basis function: We use the following second-moment Gaussian radial basis function in the message passing involved in down- and up-sampling

$$\phi_c(r) = \frac{2}{\dim \cdot (2\pi s_c^2)^{\frac{\dim}{2}}} \frac{r^2}{2s_c^2} \exp\left(-\frac{r^2}{2s_c^2}\right) \phi_{\text{env}}(r) \quad (18)$$

where $\dim = 3$ and s_c are 16 different scale coefficients evenly spaced between $0.3023 a_0$ and $2.192 a_0$, chosen such that two standard deviations of the Gaussians would reach the smallest and largest covalent radius estimates from Pyykko and Atsumi.¹⁴⁰ The squared term r^2 is chosen to suppress the influence of the near-core features, so that the learned coarsened features focus more on the bonding area. The polynomial envelope function ϕ_{env} is taken from Gasteiger *et al.*¹⁴¹ and defined as

$$\phi_{\text{env}}(r) = 1 - \frac{1}{2} \left(\frac{r}{r_{\text{max}}}\right)^p \left(p(p+1) \left(\frac{r}{r_{\text{max}}} - 1\right)^2 - 2p \left(\frac{r}{r_{\text{max}}} - 1\right) + 2 \right) \quad (19)$$

for $0 \leq r \leq r_{\text{max}}$, and smoothly extends to 0 for $r > r_{\text{max}}$. We use polynomial degree $p = 8$ and cutoff radius $r_{\text{max}} = 5.0$ Bohrs. The envelope function ensures the non-local interaction is finite. This entails that for densities represented using the standard atomic grids, the model scales linearly in number of atoms for systems with atomic distances lower bounded by any given strictly positive constant.

A.5 Intuition on the structure of the non-local layer

This section is meant as a theoretical motivation for the structure of the non-local component of our functional. The main role of the non-local component is to capture interactions between features at different grid points, through helper nodes called coarse points. We provide an intuition about:

1. how the non-local layer has the ability to approximate non-local interactions independent of the coarse points chosen for computational convenience;
2. how the expressivity of our functional could be systematically increased to approximate arbitrary target functional to any desired accuracy.

We consider $(\{\phi_c, Y_\ell^m\})$ a basis set of $L^2(\mathbb{R}^3)$. We take two copies of it, indexed by (c, ℓ, m) and (c', ℓ', m') and consider a product basis of $L^2(\mathbb{R}^3 \times \mathbb{R}^3)$. A given function $\kappa \in L^2(\mathbb{R}^3 \times \mathbb{R}^3)$ that is globally rotationally invariant, i.e. $\kappa(Qr_i, Qr_k) = \kappa(r_i, r_k)$ for any $Q \in \text{SO}(3)$, can be expressed (this is shown in Theorem 1 later in this section) as

$$\kappa(r_i, r_k) = \sum_c \sum_\ell \phi_c(\|r_i\|) \left\langle Y_\ell(\hat{r}_i), \sum_{c'} C_{c,\ell,c'} \phi_{c'}(\|r_k\|) Y_\ell(\hat{r}_k) \right\rangle, \quad (20)$$

where $C_{c,\ell,c'}$ is a set of coefficients that depend on the function κ and the basis chosen and Y_ℓ is a vector that contains Y_ℓ^m for $-\ell \leq m \leq \ell$. Using this expression, a convolved feature h of the form

$$h(r_i) := \int \tilde{h}(r_k) \kappa(r_i, r_k) dr_k$$

can be written as

$$h(r_i) = \sum_c \sum_\ell \phi_c(\|r_i\|) \left\langle Y_\ell(\hat{r}_i), \sum_{c'} C_{c,\ell,c'} \int \tilde{h}(r_k) \phi_{c'}(\|r_k\|) Y_\ell(\hat{r}_k) dr_k \right\rangle. \quad (21)$$

We can now draw a parallel between this expression and the structure of the non-local layer, which shows that our non-local layer can approximate two-body interactions between features on the grid. Combining the downsampling, upsampling and post-upsampling parts described in Eqs. (13), (14), and (17), we obtain the following expression with some rearrangement

$$h_{\text{post-up},i} = \sigma(W_{\text{post-up}} h'_i + b_{\text{post-up}}) \quad (22)$$

$$h'_i = \sum_j \sum_\ell \phi_c(\|r_{ij}\|) \left\langle Y_\ell(\hat{r}_{ij}), \sum_{c'} W_{\text{up},\ell c'} \sum_k \phi_{c'}(\|r_{jk}\|) Y_\ell(\hat{r}_{jk}) \tilde{h}_{k\ell c'} w_k \right\rangle \pi_{ij}, \quad (23)$$

where we redefined part of the downsampled $H_{j\ell c'}$ in Eq. (13) as $\tilde{h}_{k\ell c'}$ to make the dependence on $\phi_{c'}$ and Y_ℓ more explicit. The \sum_k approximates the integral in Eq. (21).

Comparing the expressions of $h_{\text{post-up},i}$ in Eq. (23) and $h(r_i)$ in Eq. (21), we note a similar pattern. In our case, the coefficients $C_{c,\ell,c'}$ are part of the learnable parameters, the function \tilde{h} also has a learnable component. Moreover, rather than expanding around the origin, we expand around a set of coarse points R_j and then “average” the contributions. In theory, one can expand around any position, but the fidelity of the approximation with a finite basis may depend on the choice. As atomic density features are expected to be symmetric around the atomic centers, atomic centers are a natural choice for the expansion. The final aggregation on c in Eq. (21) in our case is generalized by the linear mixing with weights $W_{\text{post-up}}$.

We now provide the result that was taken for granted at the beginning of the discussion:

Theorem 1. *Let κ be a function in $L^2(\mathbb{R}^3 \times \mathbb{R}^3)$ capturing the 2-body interaction between 3D coordinates r_1 and r_2 . We assume κ is globally rotationally invariant, that is for any $Q \in SO(3)$, we have*

$$\kappa(Qr_1, Qr_2) = \kappa(r_1, r_2). \quad (24)$$

Assume $\{\phi_c, Y_\ell^m\}$ is a basis set of $L^2(\mathbb{R}^3)$ and we consider 2 copies of it, indexed by (c_1, ℓ_1, m_1) and (c_2, ℓ_2, m_2) to form a product basis of $L^2(\mathbb{R}^3 \times \mathbb{R}^3)$. Then we can expand κ around the origin as follows:

$$\kappa(r_1, r_2) = \sum_{c_1, \ell} \phi_{c_1}(\|r_1\|) \left\langle Y_\ell(\hat{r}_1), \sum_{c_2} C_{c_1, \ell, c_2} \phi_{c_2}(\|r_2\|) Y_\ell(\hat{r}_2) \right\rangle \quad (25)$$

where C_{c_1, ℓ, c_2} is a set of coefficients that depend on κ and the basis set chosen and Y_ℓ is the vector form of Y_ℓ^m for $-\ell \leq m \leq \ell$.

Proof. By the Hilbert space structure of $L^2(\mathbb{R}^3 \times \mathbb{R}^3)$, we can decompose κ as

$$\kappa(r_1, r_2) = \sum_{\substack{c_1, \ell_1, m_1 \\ c_2, \ell_2, m_2}} C_{c_1, \ell_1, m_1, c_2, \ell_2, m_2} \prod_{i=1}^2 \phi_{c_i}(\|r_i\|) Y_{\ell_i}^{m_i}(\hat{r}_i),$$

for a certain set of coefficients $C_{c_1, \ell_1, m_1, c_2, \ell_2, m_2}$, where $-\ell_1 \leq m_1 \leq \ell_1$ and $-\ell_2 \leq m_2 \leq \ell_2$. Using the rotational invariance property, we have

$$\kappa(r_1, r_2) = \int \kappa(r_1, r_2) dQ = \sum_{\substack{c_1, \ell_1, m_1 \\ c_2, \ell_2, m_2}} C_{c_1, \ell_1, m_1, c_2, \ell_2, m_2} \prod_{i=1}^2 \phi_{c_i}(\|r_i\|) \int \prod_{j=1}^2 Y_{\ell_j}^{m_j}(Q\hat{r}_j) dQ$$

where dQ denotes the uniform measure over $SO(3)$. Using the equivariance property of spherical harmonics (Lemma 11 in Dusson *et al.*¹⁴²), we obtain

$$\begin{aligned} \kappa(r_1, r_2) &= \sum_{\substack{c_1, \ell_1, m_1 \\ c_2, \ell_2, m_2}} C_{c_1, \ell_1, m_1, c_2, \ell_2, m_2} \prod_{i=1}^2 \phi_{c_i}(\|r_i\|) \int \prod_{j=1}^2 \sum_{k_j=-\ell_j}^{\ell_j} Y_{\ell_j}^{k_j}(\hat{r}_j) D_{k_j m_j}^{\ell_j}(Q) dQ \\ &= \sum_{\substack{c_1, \ell_1, m_1 \\ c_2, \ell_2, m_2}} C_{c_1, \ell_1, m_1, c_2, \ell_2, m_2} \prod_{i=1}^2 \phi_{c_i}(\|r_i\|) \sum_{k_1, k_2} \prod_{j=1}^2 Y_{\ell_j}^{k_j}(\hat{r}_j) \int D_{k_2 m_2}^{\ell_2}(Q) D_{k_1 m_1}^{\ell_1}(Q) dQ, \end{aligned}$$

where $D_{k_i, m_i}^{\ell_i}$ are the Wigner D-matrices. Using Eq. (2) in Lemma 4.11.1 in Varshalovich *et al.*¹⁴³, we evaluate the integral of the product of Wigner matrices to be $\delta_{\ell_1, \ell_2} \delta_{m_1, -m_2} \delta_{k_1, -k_2}$, up to some constants will be absorbed into the coefficients C without renaming. Hence, we can reduce the indices to just c_1, c_2, ℓ, m , and k and obtain

$$\kappa(r_1, r_2) = \sum_{c_1, c_2, \ell, m} C_{c_1, c_2, \ell, m} \prod_{i=1}^2 \phi_{c_i}(\|r_i\|) \sum_k Y_\ell^k(\hat{r}_2) Y_\ell^{-k}(\hat{r}_1).$$

Note that the summation over m is independent of the basis functions ϕ_{c_i} and Y_ℓ^k . This means we can further simplify the expansion by absorbing the summation over m into a newly defined $C_{c_1, c_2, \ell}$

$$\kappa(r_1, r_2) = \sum_{c_1, c_2, \ell} C_{c_1, c_2, \ell} \prod_{i=1}^2 \phi_{c_i}(\|r_i\|) \sum_k Y_\ell^k(\hat{r}_2) Y_\ell^{-k}(\hat{r}_1).$$

which we rearrange to be

$$\begin{aligned}\kappa(r_1, r_2) &= \sum_{c_1, c_2, \ell} C_{c_1, \ell, c_2} \phi_{c_1}(\|r_1\|) \langle Y_\ell(\hat{r}_1), \phi_c(\|r_2\|) Y_\ell(\hat{r}_2) \rangle \\ &= \sum_{c_1, \ell} \phi_{c_1}(\|r_1\|) \left\langle Y_\ell(\hat{r}_1), \sum_{c_2} C_{c_1, \ell, c_2} \phi_{c_2}(\|r_2\|) Y_\ell(\hat{r}_2) \right\rangle,\end{aligned}$$

where Y_ℓ is the vector containing Y_ℓ^k for $-\ell \leq k \leq \ell$, obtaining the desired expression. \square

Extension to N -body interaction. Theoretically, one could generalize the theorem above to N -body interactions and adapt the non-linear layer accordingly.^{142,144}

A.6 Related work

The theoretical foundation developed in this section is firmly based on the framework of the *atomic cluster expansion* (ACE),^{142,145} which enables the systematic construction of a complete descriptor of the atomic environment. Specifically, the expressivity of message passing can be enhanced by increasing the basis set size parameters ℓ and c , as well as the correlation order of the interaction (two-body in our case).¹⁴⁴ In the ACE framework, the atomic center directly receives the message. In contrast, our approach accumulates spherical tensor features at coarse points, serving both as a computational aid and as a means to enrich modeling capacity. These aggregated features are then transmitted back to the integration grid points. This mechanism is reminiscent of numerical techniques such as the fast multipole method (FMM),¹⁴⁶ where, for example, the Laurent expansion ϕ_c can be used to approximate the long-range two-body Coulomb kernel $f(r_1, r_2) = 1/(r_1 - r_2)$. A similar strategy is employed in Gao *et al.*¹⁴⁷, where nuclei-centric descriptors of the total density are constructed. Their work further processes the coarsened features using message-passing layers within a neural force field framework,¹⁴⁸ enabling direct graph-level readout. However, in our preliminary experiments, we observed that this approach can lead to significant overfitting when evaluated on the Diet GMTKN55 benchmark.

Other studies have also leveraged coarsened features in various contexts, such as modeling protein binding sites¹⁴⁹ and compressing input signals in fluid dynamics simulations.¹⁵⁰

From a theoretical standpoint, learning the enhancement factor corresponds to learning a mapping between functional spaces. In recent machine-learning literature, neural operators have emerged as powerful tools for this purpose.¹⁵¹ These models learn operators that map input functions to output functions and can be evaluated with arbitrary discretization of the domain. In particular, our non-local layer shares similarities with low-rank kernel neural operators,¹⁵¹ which retain rich functional expressivity while reducing computational cost. We tailored the non-local layer design to better suit the structure of the atomic grids, as the irregularity limits the applicability of most standard techniques from the neural operator literature.

B Training details

B.1 Training objective

The objective of training is regression loss for reaction energy prediction, which linearly combines molecular total energies. The total energy of a molecule M is computed as

$$E_{\text{tot}}^\theta[M] = E_{\text{tot-xc}}[M] + E_{\text{xc}}^\theta[\rho] \quad (26)$$

where $E_{\text{tot-xc}}$ is the total energy minus the exchange-correlation component, calculated using the B3LYP functional.^{152,153} This is precomputed. Notably, this quantity contains the D3 dispersion energy. We calculate the reaction energy as a weighted sum of the stoichiometric coefficients $\{c_M\}$ for a reaction

$$\Delta E = \sum_M c_M E_{\text{tot}}[M]. \quad (27)$$

The final loss is then defined as a weighted mean squared error

$$\mathbb{E} \left[\frac{|\Delta E - \Delta E^{\text{ref}}|^2}{0.001 + |\Delta E^{\text{ref}}|} \right] \quad (28)$$

where the expectation is taken over all reactions, sampled uniformly, and ΔE^{ref} are the reference reaction energies.

Table 2: Parameters of Adafactor optimizer

Hyperparameter	Value
Maximum learning rate	0.01
Warmup time	50,000
Num. steps	500,000
Clipping threshold	1.0
Scale parameter	True

B.2 Parameter initialization

The weights of the local parts of the network are initialized according to the Xavier initialization scheme¹⁵⁴ using uniform distribution and the biases are set to 0. The parameters of the non-local layer are initialized with a modified Xavier scheme which also takes into account that tensor features of the same order share weights.¹⁵⁵

B.3 Optimization

Models trained in this paper were all optimized with the Adafactor optimizer.¹⁵⁶ We built on top of the implementation in the Hugging Face Transformers library¹⁵⁷ with adaptive LR using root-mean-square (RMS) scaling. We replaced the original global learning rate scaling of $1/\sqrt{\text{step}}$ with a cosine schedule, defined as

$$\text{lr} \leftarrow \begin{cases} \text{max_lr} \times \frac{\text{step}}{\text{warmup_time}}, & \text{if } \text{step} \leq \text{warmup_time} \\ \text{max_lr} \times \left(1 + \frac{1}{2} \cos \left(\frac{\text{step} - \text{warmup_time}}{\text{num_steps} - \text{warmup_time}} \pi \right) \right), & \text{otherwise.} \end{cases} \quad (29)$$

Optimizer hyperparameters are summarized in Table 2. When training Skala, we found the Adafactor optimizer to outperform other popular optimizers such as AdamW or Nesterov SGD. All ablation runs were done on 4 A100 GPUs, amounting to a total minibatch size of 4, in a distributed data parallel manner (one reaction per GPU). All models were trained for 500k steps. The final Skala functional was trained on 16 A100 GPUs with an effective batch size of 16 reactions per training iteration.

Furthermore, we perform uniform model weight averaging over a window size of 10,000 iterations to improve convergence.

B.4 Self-consistent fine-tuning

Empirically, we find the functionals trained on B3LYP features already yield decent performance when evaluated self-consistently, but sometimes there can be a gap in their predictive power compared to evaluating on B3LYP densities. To reduce this gap, we introduce a self-consistent fine-tuning strategy to transfer the predictive performance.

Concretely, recall that to evaluate the functional we solve the following minimization problem

$$E_{\text{tot}} = \min_C E_{\text{tot}}^\theta[C] \quad (30)$$

with C being a $B \times N$ matrix (B and N stand for the number of basis functions and number of electrons) with orthonormal columns, representing the occupied orbitals. By the envelope theorem (the first-order stationarity condition), we have that

$$\nabla_\theta E_{\text{tot}} = \nabla_\theta E_{\text{tot}}^\theta[C^*] \quad (31)$$

where $C^* = \arg \min_C E_{\text{tot}}^\theta[C]$. That is, to make proper model updates, we simply need to train on the ground state density matrices found self-consistently or via any minimization procedure. Therefore, at the fine-tuning stage, we take the model weights trained previously and fine-tune on self-consistent densities produced by the model itself. We use the same weighted loss as in Eq. (28). We reinitialize the optimizer state, use a constant global learning rate of 0.0005, and enable automatic RMS learning rate scaling and RMS gradient clipping. We fine-tune with a minibatch size of 1 on 1 A100 GPU for 1,000 steps in the ablation experiments and for 6,500 steps for the final checkpoint, monitoring the density error as explained in Sec. 4.1 of the main paper.

To produce self-consistent densities, we resort to a simpler SCF procedure: we use the PySCF loop along with DIIS on the latest 8 updates. We use the Treutler-Ahlrichs radial grids and grid level 3 for integration. Densities are represented in the def2-QZVP basis set.¹⁵⁸ We set the density threshold to be 10^{-8} , and discard grid points with initial density values lower than the threshold. Density fitting is enabled. The procedure starts from the MINAO initial guess and runs until energy change is lower than $5 \cdot 10^{-6} E_h$ and orbital gradient norm is smaller

than $1 \cdot 10^{-3} E_h$. The algorithm is terminated after 40 steps if not converged. During training, we first attempt to converge all the molecules in a reaction. If any molecule does not meet the convergence criteria, we discard the reaction altogether and try a new one until all the molecules in the reaction converge.

C Training data: computational details

This section specifies in detail the computational protocols that were used to produce our training data.

C.1 MSR-ACC/TAE dataset

In this section, we provide a summary of the MSR-ACC/TAE set. The protocol for generating it is specified in detail in a separate publication.¹⁵⁹ The molecular structures were obtained by enumerating all plausible covalent graphs of closed-shell charge-neutral molecules with up to 4 non-hydrogen atoms up to argon excluding the rare-gas elements and by sampling from graphs with up to 5 such atoms, then determining the 3D structure by a cascade of geometry relaxation steps with increasingly accurate methods, B3LYP-D3(BJ)/def-TZVPP being the final one. We only keep the lowest-energy conformer for each graph. Molecular graphs (with undetermined bond order) are obtained from the bond model of GFN-FF.¹⁶⁰ Molecules for which B3LYP/def-TZVPP predicts the triplet to be lower in energy than the singlet are excluded. The molecules are labeled with total atomization energies obtained by the W1-F12 protocol,¹⁶¹ which reproduces CCSD(T)/CBS at benchmark accuracy. Molecules for which the relative contribution of the perturbative triple excitations to the atomization energy (%TAE[(T)]) is larger than 6% (a sign of significant multireferential character) are excluded. All resulting stable equilibrium structures consisting of a single covalently bound fragment (90.7%) can be found in the released MSR-ACC/TAE25 dataset.¹⁵⁹ This released dataset is combined with the remainder of structures consisting of two or more covalent fragments to form the MSR-ACC/TAE training dataset.

C.2 MSR-ACC/IP, /PA, /Conf, and /Reactions datasets

The reactions in all remaining datasets in MSR-ACC are labeled with a slightly modified W1w protocol,^{161,162} an earlier version of W1-F12 with a similar accuracy and somewhat higher computational cost, using the MRCC software package.¹⁶³ In W1w, the Hartree-Fock (HF) component of the total energy is extrapolated to the complete basis-set limit (CBS) from the jul-cc-pV(T+d)Z and jul-cc-pV(Q+d)Z basis sets¹⁶⁴ using the $E(L) = E_\infty + A/L^\alpha$ two-point extrapolation formula, with $\alpha = 5$. The valence CCSD correlation energy is extrapolated from the same basis sets with an extrapolation exponent of $\alpha = 3.22$. The valence perturbative triple excitations are extrapolated from the jul-cc-pV(D+d)Z and jul-cc-pV(T+d)Z basis with an extrapolation exponent of $\alpha = 3.22$. The CCSD(T) inner-shell contribution is calculated with the cc-pwCVTZ basis set (modification of the original W1w which used a custom basis set). Like in MSR-ACC/TAE, we exclude reactions where any structure has %TAE[(T)] exceeding 6%.

The reactions in MSR-ACC/EA and /PA were obtained by removing an electron and a uniformly sampled proton, respectively, from uniformly sampled molecules from MSR-ACC/TAE. The reactions in MSR-ACC/Conf are conformational changes up to 10 kcal/mol in molecules from MSR-ACC/TAE generated with the CREST program,¹⁶⁵ with structures relaxed at the B3LYP/def2-TZVPP level. The reactions in MSR-ACC/Reactions are barrier heights of elementary reactions of organic molecules with up to eight atoms. The initial structures for this dataset were sampled from the public datasets Transition1x,¹⁶⁶ RFD1-CNHO,¹⁶⁷ and 3DReact,¹⁶⁸ and were then recombined through an in-house reaction exploration engine similar in function to Chemoton¹⁶⁹ or AutodE.¹⁷⁰ The resulting reaction paths were refined by IRC optimization with TPSSh¹⁷¹/def2-SVP.

C.3 Atomic datasets

Total energies, ionization potentials up to triple ionization, and electron affinities of atoms up to argon excluding Li and Be were calculated at CCSD(T)/CBS by extrapolating the HF component with the two-point formula of Karton & Martin¹⁷² and the CCSD(T) correlation component with the cubic power law formula from the aug-cc-pCVQZ and aug-cc-pCV5Z basis sets.

C.4 3rd-party public datasets

The W4-CC dataset¹⁷³ of total atomization energies of linear and cyclic carbon clusters is labeled by the W4 computational protocol which reaches experimental accuracy or better.

All NCIAtlas^{174–178} datasets (D442x10, SH250x10, R739x5, HB300SPXx10) of non-covalent intermolecular binding energies are labeled at the CCSD(T)/CBS level with a composite scheme that extrapolates separately MP2 and the residual difference between CCSD(T) and MP2.

C.5 Density features on the grid

To regularize the trained model with respect to numerical variations on the grid, we employ a data augmentation strategy where the density is computed on eight distinct integration grids, using level 2 and level 3 as defined in PySCF¹⁷⁹ with four different angular integration schemes: Treutler, Mura–Knowles, Gauss-Chebyshev and Delley. We use the same basis set and integration grid for molecules in the same reaction, to account for error cancellation. During training we evaluate our functional at fixed densities using B3LYP^{152,153} in the def2-QZVP basis set¹⁵⁸ or the ma-def2-QZVP basis set¹⁸⁰ for all reactions containing anions. Based on the fixed density we compute the relative energy of a reaction from the B3LYP total energy without the XC energy.

D Evaluation protocols

In this section, we describe the evaluation settings for the four benchmark categories conducted in this paper: (1) reaction energies, (2) dipole moments, (3) geometry optimization, and computational cost (4).

D.1 Evaluation sets

Reaction energies Our primary evaluation sets are the W4-17¹⁸¹ and GMTKN55¹⁸² datasets. W4-17 is a diverse and highly-accurate dataset of atomization energies of small molecules and GMTKN55 is the de facto standard benchmark for electronic structure methods covering five categories: basic properties, thermochemistry, kinetics, intermolecular non-covalent interactions, and conformational energies (or intramolecular non-covalent interactions). For the ablation studies on the model architecture and dataset composition in Sec. 3.1 and Sec. 3.2, we instead evaluate on the representative subset Diet GMTKN55,¹⁸³ containing 100 reactions, to reduce the computational cost of these ablations. Additionally, we evaluate on the MSR-ACC/TAE25 holdout set.¹⁵⁹

Dipole moments To confirm the quality of Skala SCF electron densities we compare its dipole moments against a well-established benchmark set.¹⁸⁴ We use the recommended computational protocol¹⁸⁴ with the aug-pc-3 basis. We exclude CH₂ because it was the only molecule for which we could not reproduce the reported dipole errors of the baseline functionals.

Geometry optimization benchmark sets Furthermore, we evaluate our functional on (semi-)experimental geometry datasets, including light main group bond lengths (LMGB35),¹⁸⁵ heavy main group bond lengths (HMGB11),¹⁸⁵ and the bond lengths and bond angles of 21 small molecules (CCse21).¹⁸⁶

Computational cost benchmark set The computational cost results were produced using a dataset of 38 molecules shown in Fig. 8. The systems are collected from Grimme,¹⁸⁷ S30L,¹⁸⁸ HS13L,¹⁸⁹ and NCI16L.¹⁹⁰

D.2 Baselines and dispersion correction settings

We compare our functional with several traditional baseline methods, including (meta-)GGA functionals, revPBE,¹⁹¹ B97M-V,¹⁹² and r²SCAN,^{193,194} and (range-separated) hybrid functionals, B3LYP,^{152,153} M06-2X,¹⁹⁵ ω B97X-V,¹⁹⁶ and ω B97M-V.¹⁹⁷ RevPBE, r²SCAN, B3LYP were evaluated with a D3(BJ) correction, while M06-2X was evaluated with a D3(0) correction. Skala was evaluated using a D3(BJ) correction with B3LYP parameters. B97M-V, ω B97X-V, and ω B97M-V have a VV10¹⁹⁸ correction, as indicated with “-V”. D3 dispersion corrections^{137,138} are included using the simple-dftd3 package.¹⁹⁹

D.3 Basis sets

For reaction energy benchmarks, we use the def2-QZVP^{158,200} basis set or the ma-def2-QZVP¹⁸⁰ basis set for reactions containing hard-anionic systems. For the dipole moment benchmark, we use the aug-pc-4 basis.²⁰¹ For geometry optimization, we use the smaller def2-TZVP basis set.²⁰⁰

D.4 SCF retry protocol

As expected for a ML functional, Skala’s SCF convergence is slightly more challenging than for traditional functionals, at least when using PySCF.¹⁷⁹ For this reason, we find it important to give all the specifics of our SCF settings and report statistics for Skala compared to baseline functionals.

We evaluate our functional using PySCF^{179,202,203} with appropriate Coulomb fitting basis set.^{204,205} In the evaluation process, we start SCF computations from the MINAO^{206,207} initial guess. We use a Treutler¹³³ grid with level 3. We note that for dipole moment prediction, this deviates from the grid setting of Ref. [184]. For reaction energy benchmarks and dipole computations, the SCF is run with convergence tolerance on total energy

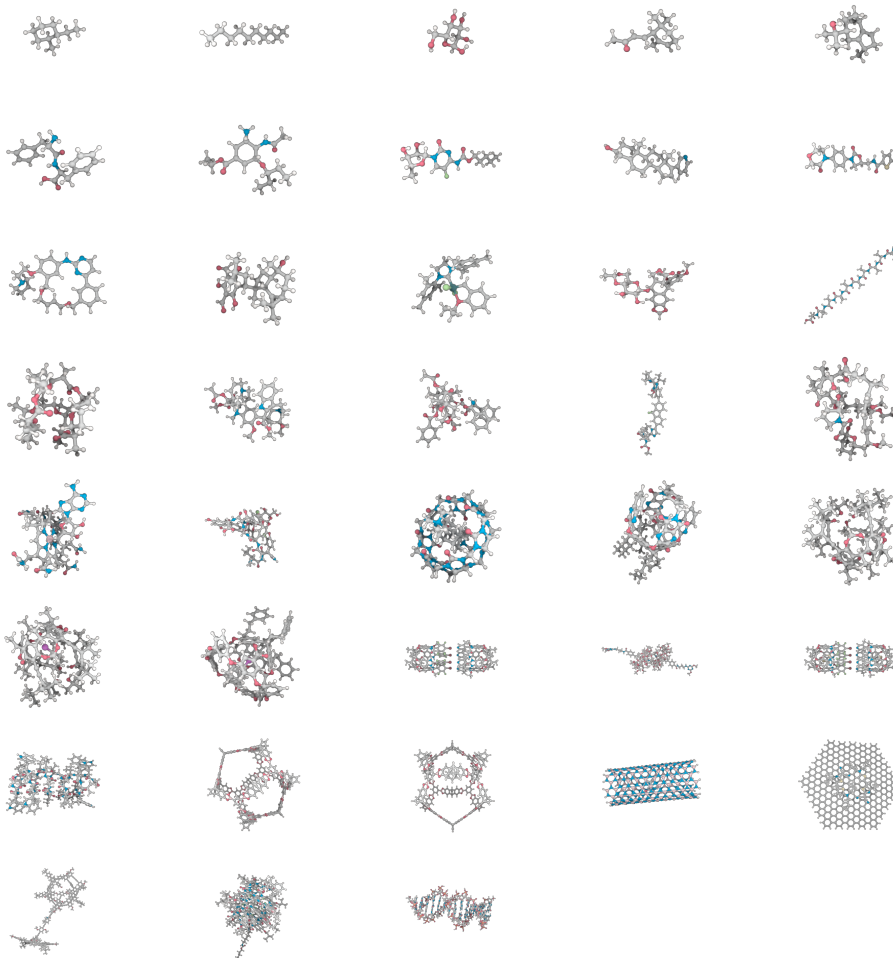


Figure 8: Systems used for evaluating the computational cost of the Skala functional

change equal to $5 \cdot 10^{-6} E_h$ and convergence tolerance on gradient norm equal to $10^{-3} E_h$. The SCF is run for a maximum number of 60 steps. If convergence criteria are not met within 60 steps, we have a retry logic in place that works as follows. Each of the following attempts is tried, in case of failure of the previous one:

1. DIIS^{208,209} with a window size of 8 is used with no damping or level shift;
2. Damping is set to 0.5 with DIIS^{208,209} start cycle set to 7;
3. The level shift parameter is incrementally set to 0.1, 0.3, and 0.5 if there is an iteration of the previous attempt with HOMO-LUMO gap (both in the spin-up and spin-down channel) below $0.1 E_h$. This means that if an attempt fails to converge, but it has HOMO-LUMO gap (both in the spin-up and spin-down channel) bigger than $0.1 E_h$ at every step, no further attempts of increasing the level shift are made.
4. As the last attempt, we enable the second-order solver from PySCF.^{210,211}

If none of the attempts mentioned above fails to reach convergence within 60 steps or converges to a non-Aufbau higher energy state, it is marked as unconverged and manually converged using a Gradient Descent algorithm, detailed in Sec. D.5. Results on how often each attempt described in the SCF retry protocol was utilized when evaluating on W4-17, GMTKN55 and dipoles are reported in Table 3.

For geometry optimization, the same logic described above is used for the initial geometry, but with stricter convergence criteria (see Sec. D.6). The settings are then kept fixed in subsequent geometry optimization steps.

D.5 SCF with orbital gradient descent fallback

As the SCF retry protocol we describe in Sec. D.4 does not converge 100% of the time, we introduce a more robust routine. We start out with an initial guess of density matrix using the Minimal Atomic Orbital basis (MINAO)^{206,207} and diagonalize the Fock matrix to obtain a permissible idempotent density matrix. In the first cycle, we compute the total energy. From the second cycle and beyond, we first check if diagonalization with

Table 3: Analysis of the retry protocol for SCF convergence described in Sec. D.4 for our functional Skala and baselines functionals. The percentages are over the evaluations on W4-17 (211 structure), GMTKN55 (2372 structures) and dipoles (151 structures), for a total of 2734 structures.

	First SCF	Damp+DIIS	Lev. shift 0.1	Lev. shift 0.3	Lev. shift 0.5	Newton	Manual
revPBE	99.93%	0.04%	0.00%	0.00%	0.00%	0.03%	0.00%
r ² SCAN	99.93%	0.00%	0.04%	0.00%	0.00%	0.03%	0.00%
B97M-V	99.89%	0.07%	0.00%	0.00%	0.00%	0.00%	0.04%
B3LYP	100.00%	0.00%	0.00%	0.00%	0.00%	0.00%	0.00%
M06-2X	99.89%	0.00%	0.00%	0.00%	0.00%	0.00%	0.11%
ω B97X-V	100.00%	0.00%	0.00%	0.00%	0.00%	0.00%	0.00%
ω B97M-V	99.93%	0.00%	0.00%	0.00%	0.00%	0.00%	0.07%
Skala	98.83%	0.15%	0.51%	0.18%	0.00%	0.29%	0.04%

DIIS^{208,209} leads to a decrease in energy; if not, we resort to gradient descent with line search in the space of molecular orbital coefficients C .

In what follows, we discuss the spin-agnostic case to simplify the notation. The matrix C can be decomposed into the occupied and virtual parts $[C_{\text{occ}}, C_{\text{vir}}]$, where only the occupied part contributes to the density matrix $\Gamma_{ij} = \sum_{k=1}^N C_{ik}C_{jk}$, for $1 \leq i, j \leq B$, which means $\Gamma = C_{\text{occ}}C_{\text{occ}}^\top$. From the density matrix, we generate the features needed to compute the exchange-correlation energy on the grid and compute the other energy components including the kinetic energy, Hartree electrostatics, and external potential. We can write the total energy as a function of Γ , $E_{\text{tot}}(\Gamma)$. The Fock matrix is defined as the gradient with respect to the density matrix $F := \frac{dE_{\text{tot}}}{d\Gamma}$. When computing the gradient with respect to the orbital matrix C , we need to take into account the fact that Γ is invariant to the rotation of the columns of C_{occ} and that all columns of C need to stay orthogonal. This can be done by looking at the virtual-occupied blocks of the Fock matrix

$$\Delta_C^{\text{hor}} = [(I - \Gamma)FC_{\text{occ}}, -\Gamma FC_{\text{vir}}]. \quad (32)$$

This is also known as the horizontal lift of the Riemannian gradient in the Grassmannian manifold (space of density matrices) to the tangent space of the orthogonal group (space of orbital coefficients).²¹²

We use the negative gradient as the search direction, and with step size α we use the exponential map to produce the new orbital matrix $C' \leftarrow C \exp(-\alpha C^\top \Delta_C^{\text{hor}})$. The form of the update can be equivalently derived by taking the gradient of $C \exp(A)$ with respect to an anti-symmetric matrix A .²¹³ We initialize the step size to be 1.0 for each calculation, and adaptively set the step size of the subsequent iterations to be 1.1 times the previous admissible step size. Within each iteration, a step size is considered admissible if it satisfies the Armijo rule

$$E_{\text{tot}}(C') - E_{\text{tot}}(C) \leq -c_1 \alpha \|\Delta_C^{\text{hor}}\|^2 \quad (33)$$

where we set $c_1 = 0.1$. We do not check the curvature condition commonly used in line search to avoid unnecessary backward computation. If the Armijo rule is violated, we form a quadratic approximation to E_{tot} as a function of α , and use the minimizer as the new trial.²¹⁴ To prevent the line search strategy from being too aggressive or too conservative, we clamp the search space to be within $[0.1\alpha, 0.9\alpha]$.

Empirically, we find that robustness of gradient descent with line search hinges on good alignment between numerical gradient and energy estimation. Therefore, all computations with gradient descent have been performed in double precision. For all computation attempts using gradient descent, we first converge with a downgraded basis, and then project onto the bigger basis set. For example, we first use def2-TZVP and then def2-QZVP.

D.6 Geometry optimization: implementation

For geometry optimization, we need the gradient of the total energy with respect to the nuclear coordinates. For standard approximate DFT functionals, this entails the evaluation of the following contributions to the nuclear gradient:

1. The explicit dependence on the nuclear positions in the nuclear potential (Hellman–Feynman forces)
2. The dependence of the atomic centered basis functions (Pulay forces)²¹⁵
3. The dependence of the integration grid on the atomic positions.

For sufficiently large grid the contribution from the grid integration tends to be small, so it can be neglected for traditional functionals. However, since the Skala architecture does not only use the grid for integration of the final energy density, but also for down- and up-sampling, we included it in computing the total forces. Additionally, we need to take into account

4. The explicit dependence of the E_{xc} functional on the nuclear positions due to the coarse points.

For the initial geometry optimization step, we use the same retry protocol as described in Sec. D.4, and during the course of geometry optimization we stick to the SCF method which successfully converged the electronic structure of the initial geometry. We use the GEOMETRIC package²¹⁶ to optimize the geometry. The convergence tolerance on the energy change was tightened to $5 \cdot 10^{-7} E_h$ and on the gradient norm to $10^{-5} E_h$, which was important to obtain accurate enough nuclear gradients for GEOMETRIC to always converge.

D.7 Computational cost: GPU and CPU implementation

GPU implementation The functional was integrated with Accelerated DFT program²¹⁷ via an extension of the GauXC library^{218–220} to evaluate the Skala functional from the TorchScript exported checkpoint. For a detailed description of the Accelerated DFT program and the optimization techniques used for DFT calculations, we refer to the original publication.²¹⁷ In the initial integration the features computed on the grid points are collected in GauXC, passed to the model for computing the exchange-correlation energy and potential and afterwards redistributed into the batches handled by GauXC. The computation of the exchange-correlation potential is done by backpropagation using the TorchScript framework.

Calculations for GPU timings were performed on Azure NC24ADS V4 A100 virtual machines with Accelerated DFT,²¹⁷ using def2-TZVP basis set with density fitting (RIJ) for the Coulomb integrals for all functionals and exact exchange integrals for all hybrid functionals, def2-universal-jkfit as auxiliary basis set, gm3 grid level for integrating the exchange-correlation energy, Treutler grid pruning and Mura–Knowles radial integration scheme.

CPU implementation CPU timings were performed on Azure E32ADS V5 virtual machines with PySCF 2.7.0,¹⁷⁹ using def2-TZVP basis set, density fitting (RIJ) for the Coulomb integrals for all functionals, and density fitting (RIK) for exchange integrals for all hybrid functionals, def2-universal-jkfit as auxiliary basis set, grid level 2 for integrating the exchange-correlation energy, with Treutler–Ahlrichs radial integration scheme and NWChem grid pruning.

Additional results can be found in Sec. E.4.

E Additional results

E.1 Spin-symmetry broken solutions for multi-reference systems

For systems with a high multi-reference character, Kohn-Sham DFT is in practice prone to breaking the spin symmetry.²²¹ These spin broken states are lower in energy and almost always give an answer closer to the ground truth. Therefore, to assess the performance of the functionals on the multi-reference subset of W4-17,¹⁸¹ we allow for spin-symmetry breaking.

Since the initial guess in PySCF has proper spin-symmetry and the gradient with respect to spin-symmetry breaking directions is zero, we kick start the search for symmetry-breaking solutions by adding random noise scaled between $[-0.1, 0.1]$ to the elements of the spin-resolved initial one-electron reduced-density-matrix (1RDM) guess. This randomly perturbed initial guess is subsequently purified by first symmetrizing it and subsequently clipping its eigenvalues to be bounded between 0 and 1. We do not normalize the trace to recover the correct number of electrons. Since multiple local minima can exist for spin-symmetry breaking solutions, for each molecule of the multi-reference subset of W4-17, we ran 50 calculations with different random seeds to increase

Table 4: Absolute error statistics on W4-17 and the single-reference subset (kcal/mol). For the full set, we compute the statistics without performing symmetry breaking, with symmetry breaking applied to ${}^1\text{BN}$, B_2 and C_2 only, and applied to all multi-referential structures. All functionals without the VV10 corrections are with D3(BJ), except M06-2X which uses D3(0).

Dataset	W4-17									W4-17 singleref		
	None			${}^1\text{BN}, \text{B}_2, \text{C}_2$			All multiref			None		
	Mean	Max	Std	Mean	Max	Std	Mean	Max	Std	Mean	Max	Std
revPBE	8.09	53.89	7.52	8.05	53.89	7.53	8.05	53.89	7.53	7.22	53.89	6.78
r ² SCAN	4.51	26.62	4.31	4.46	26.62	4.12	4.47	26.62	4.12	3.84	25.73	3.28
B97M-V	2.90	26.47	3.35	2.84	26.47	3.04	2.84	26.47	3.04	2.52	26.47	2.81
B3LYP	3.86	27.43	4.19	3.80	24.54	3.93	3.79	24.54	3.93	3.73	24.54	3.88
M06-2X	3.01	29.25	3.72	3.01	29.25	3.72	2.98	29.25	3.63	2.39	16.91	2.38
ω B97X-V	2.59	36.83	3.73	2.59	36.83	3.73	2.54	36.83	3.71	2.14	11.77	1.91
ω B97M-V	2.06	31.40	2.94	2.04	31.40	2.89	2.00	31.40	2.81	1.66	8.97	1.45
Skala	1.12	12.92	1.62	1.06	8.65	1.25	1.06	8.65	1.25	0.85	3.66	0.73

Table 5: Total energies and total spin $\langle S^2 \rangle$ for the clustering of spin-symmetry broken stationary SCF solutions for the various functionals. All quantities are in atomic units.

(a) revPBE			(b) r ² SCAN		
Molecule	Total energy	$\langle S^2 \rangle$	Molecule	Total energy	$\langle S^2 \rangle$
² ClOO	[-610.467]	[0.77]	² ClOO	[-610.477]	[0.88]
² ClO ₃	[-685.611]	[0.75]	² ClO ₃	[-685.618]	[0.76]
O ₃	[-225.494]	[0.00]	O ₃	[-225.430,-225.429]	[0.21,0.00]
ClF ₃	[-759.534]	[0.00]	ClF ₃	[-759.554]	[0.00]
³ B ₂	[-49.429,-49.424]	[2.54,2.01]	³ B ₂	[-49.405,-49.389]	[2.72,2.01]
C ₂	[-75.930]	[0.88]	C ₂	[-75.895,-75.864]	[1.01,0.00]
F ₂ O	[-274.731]	[0.00]	F ₂ O	[-274.687]	[0.00]
ClF ₅	[-959.120]	[-0.00]	ClF ₅	[-959.134]	[0.00]
S ₃	[-1194.439]	[0.00]	S ₃	[-1194.566]	[0.00]
² FO ₂	[-250.147]	[0.76]	² FO ₂	[-250.093]	[0.79]
FOOF	[-349.927]	[0.00]	FOOF	[-349.860]	[0.00]
² OClO	[-610.463]	[0.75]	² OClO	[-610.479]	[0.76]
Cl ₂ O	[-995.407]	[0.00]	Cl ₂ O	[-995.489]	[0.00]
² OF	[-174.919]	[0.75]	² OF	[-174.888]	[0.75]
S ₄ -C _{2v}	[-1592.602]	[0.00]	S ₄ -C _{2v}	[-1592.774]	[0.00]
¹ BN	[-79.411]	[0.00]	¹ BN	[-79.367]	[0.00]
ClOOCl	[-1070.573]	[0.00]	ClOOCl	[-1070.637]	[-0.00]

(c) B97M-V			(d) B3LYP		
Molecule	Total energy	$\langle S^2 \rangle$	Molecule	Total energy	$\langle S^2 \rangle$
² ClOO	[-610.401]	[0.85]	² ClOO	[-610.460]	[0.98]
² ClO ₃	[-685.548]	[0.75]	² ClO ₃	[-685.587]	[0.76]
O ₃	[-225.458]	[0.00]	O ₃	[-225.437,-225.434]	[0.34,0.00]
ClF ₃	[-759.462]	[0.00]	ClF ₃	[-759.545]	[0.00]
³ B ₂	[-49.455,-49.450]	[2.48,2.01]	³ B ₂	[-49.391]	[2.00]
C ₂	[-75.941,-75.918]	[0.96,0.00]	C ₂	[-75.888,-75.870]	[0.78,0.00]
F ₂ O	[-274.703]	[0.00]	F ₂ O	[-274.702]	[0.00]
ClF ₅	[-959.038]	[0.00]	ClF ₅	[-959.114]	[0.00]
S ₃	[-1194.334]	[0.00]	S ₃	[-1194.508]	[0.00]
² FO ₂	[-250.110]	[0.79]	² FO ₂	[-250.099]	[0.83]
FOOF	[-349.882]	[0.00]	FOOF	[-349.868]	[0.00]
² OClO	[-610.402]	[0.75]	² OClO	[-610.457]	[0.76]
Cl ₂ O	[-995.318]	[0.00]	Cl ₂ O	[-995.457]	[0.00]
² OF	[-174.901]	[0.75]	² OF	[-174.900]	[0.75]
S ₄ -C _{2v}	[-1592.462]	[0.00]	S ₄ -C _{2v}	[-1592.688]	[0.00]
¹ BN	[-79.418]	[0.00]	¹ BN	[-79.375]	[0.00]
ClOOCl	[-1070.476]	[0.00]	ClOOCl	[-1070.604]	[0.00]

(e) M06-2X			(f) ωB97X-V		
Molecule	Total energy	$\langle S^2 \rangle$	Molecule	Total energy	$\langle S^2 \rangle$
² ClOO	[-610.482]	[1.19]	² ClOO	[-610.438,-610.429,-610.429]	[1.21,0.98,0.83]
² ClO ₃	[-685.616,-685.546]	[0.76,0.77]	² ClO ₃	[-685.579,-685.511]	[0.76,0.77]
O ₃	[-225.428,-225.420]	[0.50,0.00]	O ₃	[-225.446,-225.440]	[0.47,0.00]
ClF ₃	[-759.568]	[0.00]	ClF ₃	[-759.518]	[0.00]
³ B ₂	[-49.401]	[2.00]	³ B ₂	[-49.324]	[2.03]
C ₂	[-75.879]	[0.00]	C ₂	[-75.872]	[0.00]
F ₂ O	[-274.694,-274.538]	[0.00,1.03]	F ₂ O	[-274.703]	[0.00]
ClF ₅	[-959.134]	[0.00]	ClF ₅	[-959.090]	[0.00]
S ₃	[-1194.583]	[0.00]	S ₃	[-1194.437]	[0.00]
² FO ₂	[-250.080]	[1.00]	² FO ₂	[-250.098,-250.024]	[0.93,0.77]
FOOF	[-349.844]	[0.00]	FOOF	[-349.865]	[0.00]
² OClO	[-610.485]	[0.76]	² OClO	[-610.441]	[0.76]
Cl ₂ O	[-995.528]	[0.00]	Cl ₂ O	[-995.419]	[0.00]
² OF	[-174.893]	[0.75]	² OF	[-174.901]	[0.75]
S ₄ -C _{2v}	[-1592.786]	[0.00]	S ₄ -C _{2v}	[-1592.589]	[0.00]
¹ BN	[-79.380]	[0.00]	¹ BN	[-79.376]	[0.00]
ClOOCl	[-1070.674]	[0.00]	ClOOCl	[-1070.569]	[0.00]

(g) ωB97M-V			(h) Skala		
Molecule	Total energy	$\langle S^2 \rangle$	Molecule	Total energy	$\langle S^2 \rangle$
² ClOO	[-610.497,-610.436]	[1.13,0.77]	² ClOO	[-610.434]	[0.84]
² ClO ₃	[-685.647,-685.580]	[0.76,0.77]	² ClO ₃	[-685.555]	[0.75]
O ₃	[-225.467,-225.462]	[0.42,0.00]	O ₃	[-225.382]	[0.00]
ClF ₃	[-759.599]	[0.00]	ClF ₃	[-759.533]	[0.00]
³ B ₂	[-49.398,-49.392,-49.322]	[2.59,2.00,2.02]	³ B ₂	[-49.427]	[2.01]
C ₂	[-75.881]	[0.00]	C ₂	[-75.885,-75.876]	[0.83,1.01]
F ₂ O	[-274.732,-274.561]	[0.00,1.02]	F ₂ O	[-274.667]	[0.00]
ClF ₅	[-959.194]	[0.00]	ClF ₅	[-959.096]	[0.00]
S ₃	[-1194.570]	[0.00]	S ₃	[-1194.470]	[0.00]
² FO ₂	[-250.121,-250.049]	[0.90,0.77]	² FO ₂	[-250.047,-250.046]	[0.80,0.78]
FOOF	[-349.901]	[0.00]	FOOF	[-349.807]	[0.00]
² OClO	[-610.502]	[0.76]	² OClO	[-610.437]	[0.76]
Cl ₂ O	[-995.521]	[0.00]	Cl ₂ O	[-995.473]	[0.00]
² OF	[-174.918]	[0.75]	² OF	[-174.870]	[0.75]
S ₄ -C _{2v}	[-1592.775,-1592.767]	[0.68,0.00]	S ₄ -C _{2v}	[-1592.637]	[0.00]
¹ BN	[-79.386]	[0.00]	¹ BN	[-79.386,-79.374]	[1.02,0.00]
ClOOCl	[-1070.679]	[0.00]	ClOOCl	[-1070.601]	[0.00]

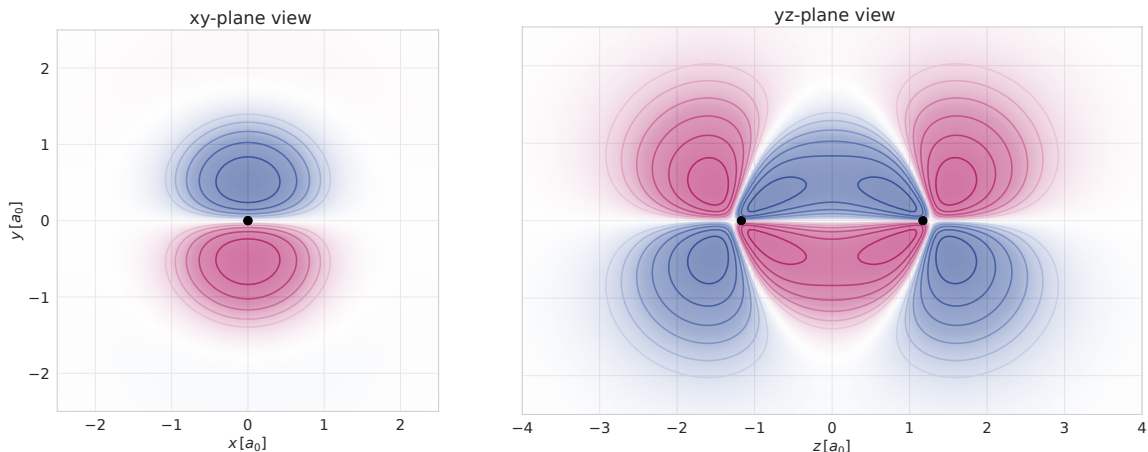


Figure 9: Spin-density difference for the lowest spin-symmetry broken solution for the C_2 molecule at $R_{C-C} = 2.34326 a_0$ with the Skala functional in def2-QZVP basis. The left panel is a cut orthogonal to the bond axis and the right panel a cut along the bond axis. The position of the carbon atoms is marked with a black disk.

the probability of finding the lowest energy solution. We have run these calculations with tighter convergence criteria: a tolerance on the energy difference equal to $10^{-8} E_h$ and a convergence tolerance on gradient norm equal to $10^{-4} E_h$. We subsequently clustered the converged results with an energy criterion of $10^{-3} E_h$ and a total spin $\langle S^2 \rangle$ criterion of $10^{-1} \hbar^2$. The result for the clustering can be found in Table 5.

We show the difference in MAE on W4-17 in Table 4, where we see that the performance of all of the functionals including Skala (except $\omega B97X-V$) can be improved by merely breaking the spin-symmetry of 1BN , B_2 and C_2 , which contributed to most of the performance gain.

To gain more understanding of how spin symmetry is broken for Skala, we have also examined the C_2 molecule in more detail for the Skala functional. In Fig. 9 we show the spin-density difference for the ground state in two planes through the bond midpoint. One sees that the typical banana bonds appear for the Skala functional similar to SCAN.²²¹

E.2 GMTKN55 benchmark

We report the full breakdown of the error on all 55 subsets of GMTKN55 in Table 7 and the contribution of each category of the subsets to the WTMAD-2 score in Table 6. We also report structures where Skala outperforms and underperforms $\omega B97M-V$ the most in the entire GMTKN55 set in Table 8.

Table 6: GMTKN55 WTMAD-2 for each category of subsets. All functionals without the VV10 corrections are with D3(BJ), except M06-2X which uses D3(0).

Functional	revPBE	r ² SCAN	B97M-V	B3LYP	M06-2X	$\omega B97X-V$	$\omega B97M-V$	Skala
Basic properties	1.81	1.58	1.25	1.34	0.84	1.01	0.71	0.79
Reaction energies	1.71	1.33	1.52	1.68	0.96	1.07	0.65	0.69
Barrier heights	1.99	1.79	0.93	1.09	0.48	0.54	0.40	0.64
Intermolecular NCI	1.27	1.42	0.72	1.16	1.09	0.62	0.59	0.52
Intramolecular NCI	1.56	1.13	1.15	1.10	1.46	0.71	0.87	1.26
WTMAD-2	8.34	7.25	5.56	6.38	4.83	3.96	3.23	3.89

Table 7: GMTKN55 unweighted MAE breakdown (kcal/mol). All functionals without the VV10 corrections are with D3(BJ), except M06-2X which uses D3(0).

	Functional	revPBE	r ² SCAN	B97M-V	B3LYP	M06-2X	ω B97X-V	ω B97M-V	Skala
Basic properties	al2x6	2.07	1.71	1.53	2.72	0.90	1.20	1.29	0.88
	alk8	3.62	3.48	2.63	2.46	2.34	0.92	2.48	3.08
	alkbde10	5.16	5.07	4.12	4.39	4.80	4.05	3.74	3.19
	bh76rc	2.80	2.97	2.02	1.98	0.94	1.51	0.87	0.57
	dc13	8.46	7.88	5.20	10.58	7.49	6.52	5.40	3.97
	dipcs10	4.77	5.12	4.52	4.68	3.11	4.05	5.20	3.17
	fh51	3.33	2.19	2.27	2.60	1.19	2.32	1.06	0.88
	g21ea	2.84	3.59	3.09	1.99	1.86	1.93	1.44	1.89
	g2lip	4.19	4.69	3.02	3.55	2.63	3.04	2.88	3.60
	g2rc	6.15	5.69	4.60	2.73	1.94	3.93	1.99	1.28
	heavysb11	2.79	3.07	2.17	3.37	8.21	1.46	2.70	2.83
	nbprc	1.98	1.61	1.76	2.01	0.94	1.45	0.91	1.26
	pa26	4.70	2.63	3.32	2.86	1.22	2.62	1.40	1.47
	rc21	4.85	5.11	3.51	2.53	1.63	3.53	1.86	2.08
	sie4x4	23.42	18.17	16.27	18.05	8.67	11.48	10.75	13.60
	taut15	1.55	1.57	0.89	1.16	0.76	0.72	0.33	0.76
	w4-11	7.56	3.88	2.87	3.21	3.02	2.82	2.08	1.28
	ybde18	4.42	3.26	4.37	4.72	2.42	2.01	2.90	1.81
Reaction energies	bsr36	1.79	0.45	0.22	3.38	2.48	2.01	0.46	0.74
	c60iso	9.85	5.32	4.85	2.40	7.86	13.70	11.85	8.54
	cdie20	1.49	1.59	1.62	0.99	0.54	0.62	0.59	0.33
	darc	3.69	2.65	3.50	8.01	2.16	4.33	0.75	2.89
	iso34	1.50	1.29	1.46	1.78	1.23	1.17	0.62	0.69
	isol24	4.58	4.02	4.09	5.80	2.73	2.98	1.62	3.50
	mb16-43	27.03	14.69	35.97	25.28	15.58	33.06	14.52	6.87
	parel	1.53	1.55	1.36	1.17	0.97	0.63	0.59	0.91
	rse43	2.32	1.52	2.11	1.72	0.63	0.98	0.77	0.47
	Barrier heights	bh76	7.84	7.01	4.15	5.10	1.22	1.69	1.33
bhdiv10		7.81	6.12	2.90	3.21	1.02	0.87	1.28	1.34
bhperi		6.27	4.73	1.15	1.15	1.35	2.09	1.13	3.13
bhrot27		0.37	0.76	0.69	0.41	0.36	0.31	0.22	0.33
inv24		1.91	1.13	1.22	1.02	1.56	1.66	1.29	1.80
px13		8.75	8.95	1.09	4.34	5.32	2.54	1.88	2.47
wcpt18		7.25	6.18	1.49	2.30	1.90	1.73	1.41	0.93
Intermolecular NCI		adim6	0.22	0.14	0.14	0.12	0.29	0.12	0.11
	ahb21	1.07	1.23	0.47	0.30	0.94	0.34	0.28	0.35
	carbhb12	1.12	1.21	0.30	0.90	0.26	0.35	0.20	0.21
	chb6	0.87	0.40	0.80	1.42	1.45	0.86	0.96	1.30
	hal59	0.73	0.83	0.47	0.58	0.35	0.30	0.28	0.20
	heavy28	0.29	0.25	0.23	0.34	0.33	0.18	0.18	0.20
	il16	0.87	0.57	0.52	0.84	0.53	1.05	0.94	0.78
	pnico23	0.88	0.86	0.22	0.48	0.29	0.18	0.26	0.19
	rg18	0.09	0.16	0.07	0.14	0.24	0.10	0.08	0.04
	s22	0.43	0.30	0.23	0.32	0.35	0.21	0.24	0.17
	s66	0.28	0.31	0.13	0.27	0.24	0.12	0.14	0.13
	water27	3.37	7.27	0.77	4.10	3.83	1.56	1.10	2.47
	Intramolecular NCI	aconf	0.10	0.15	0.15	0.06	0.24	0.02	0.06
amino20x4		0.36	0.20	0.23	0.21	0.29	0.19	0.19	0.28
but14diol		0.31	0.25	0.14	0.30	0.13	0.04	0.05	0.19
iconf		0.32	0.30	0.29	0.28	0.31	0.25	0.15	0.18
idisp		3.03	2.48	3.18	3.59	2.07	2.59	1.63	3.46
mconf		0.44	0.46	0.34	0.22	0.56	0.25	0.38	0.24
pconf21		0.86	0.46	0.82	0.52	1.10	0.32	0.63	0.96
sconf		0.54	0.54	0.18	0.30	0.27	0.15	0.17	0.16
upu23		0.48	0.37	0.44	0.62	0.52	0.55	0.47	0.60

Table 8: Reactions in GMTKN55 with the largest difference in energy prediction accuracy between Skala and ω B97M-V.

	Ref. energy [kcal/mol]	Energy error		
		Skala (a)	ω B97M-V (b)	$ b - a $
Skala performs better than ωB97M-V				
19H ₂ + 2 ² AlB ₃ H ₆ LiMg ₂ OSi ₂ → ³ O ₂ + 6BH ₃ + 2HLi + 4H ₂ Mg + 4H ₄ Si + 2AlH ₃ mb16-43	326.76	14.20	56.33	-42.13
7H ₂ + 2Al ₂ BClH ₇ Mg ₂ NaO ₂ → 2 ³ O ₂ + 2BH ₃ + 2HNa + Cl ₂ + 4H ₂ Mg + 4AlH ₃ mb16-43	806.23	6.33	45.23	-38.90
13H ₂ + 2AlC ₃ FH ₆ LiMgNaOS → F ₂ + ³ O ₂ + ³ S ₂ + 2HNa + 6CH ₄ + 2HLi + 2H ₂ Mg + 2AlH ₃ mb16-43	518.66	6.87	32.32	-25.45
6H ₂ + 2 ² B ₂ FH ₇ LiMgOS ₂ Si → F ₂ + ³ O ₂ + 2 ³ S ₂ + 4BH ₃ + 2HLi + 2H ₂ Mg + 2H ₄ Si mb16-43	737.79	5.87	27.64	-21.76
20H ₂ + 2B ₄ CClFH ₆ MgSi ₂ → F ₂ + 8BH ₃ + Cl ₂ + 2CH ₄ + 2H ₂ Mg + 4H ₄ Si mb16-43	215.39	6.27	25.51	-19.24
C ₂ → 2 ³ C w4-11	147.02	12.53	31.39	-18.86
12H ₂ + 2 ² AlBCF ₅ H ₄ Li ₂ SSi → 5F ₂ + ³ S ₂ + 2BH ₃ + 2CH ₄ + 4HLi + 2H ₄ Si + 2AlH ₃ mb16-43	1290.74	7.96	26.09	-18.12
19H ₂ + 2AlB ₄ CFH ₄ O ₂ S ₂ Si → F ₂ + 2 ³ O ₂ + 2 ³ S ₂ + 8BH ₃ + 2CH ₄ + 2H ₄ Si + 2AlH ₃ mb16-43	629.78	11.57	28.00	-16.43
10H ₂ + 2 ² AlB ₃ CH ₈ MgNO → ³ O ₂ + N ₂ + 6BH ₃ + 2CH ₄ + 2H ₂ Mg + 2AlH ₃ mb16-43	368.49	6.05	22.00	-15.95
17H ₂ + 2AlB ₃ CFH ₇ OSi ₂ → F ₂ + ³ O ₂ + 6BH ₃ + 2CH ₄ + 4H ₄ Si + 2AlH ₃ mb16-43	356.85	9.74	24.09	-14.35
3H ₂ + 2 ² B ₃ FH ₈ MgO ₂ P → F ₂ + 2 ³ O ₂ + P ₂ + 6BH ₃ + 2H ₂ Mg mb16-43	706.20	1.87	15.16	-13.30
...				
ωB97M-V performs better than Skala				
C ₁₁ H ₂₄ → C ₁₁ H ₂₄ idisp	9.10	-7.12	0.09	7.03
20H ₂ + 2Al ₂ B ₂ C ₂ ClH ₅ LiOPSi → ³ O ₂ + P ₂ + 4BH ₃ + Cl ₂ + 4CH ₄ + 2HLi + 2H ₄ Si + 4AlH ₃ mb16-43	228.17	18.60	11.54	7.06
² H ₄ O ₂ ⁺ → ² H ₂ O ⁺ + H ₂ O sie4x4	9.30	-19.47	-11.72	7.75
ClF + ² CH ₃ → ² CClFH ₃ bh76	7.10	9.71	1.79	7.92
12H ₂ + 2 ² AlBC ₃ ClH ₆ N ₂ OS → ³ O ₂ + ³ S ₂ + 2N ₂ + 2BH ₃ + Cl ₂ + 6CH ₄ + 2AlH ₃ mb16-43	114.97	12.28	4.20	8.08
C ₃₀ H ₅₀ O → C ₃₀ H ₅₀ O isol24	69.03	10.44	-1.51	8.93
³ C → ² C ⁺ g21ip	259.60	-10.09	-1.09	9.01
² H ₆ N ₂ ⁺ → H ₃ N + ² H ₃ N ⁺ sie4x4	4.90	-17.83	-8.00	9.83
² B → B ⁺ g21ip	190.40	-10.11	-0.02	10.09
⁴ N → ³ N ⁺ g21ip	335.30	-11.25	0.43	10.82
CaO → ³ O + Ca alkbde10	96.20	-15.47	-1.65	13.82

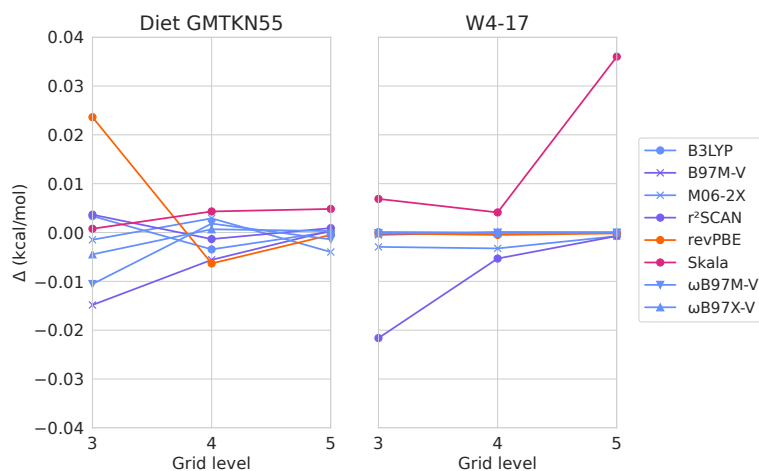


Figure 10: Evaluation on Diet GMTKN55 and W4-17 benchmarks at different pycscf grid levels (sizes). Δ on the y-axis represents the difference in WTMAD-2 for Diet GMTKN55 and MAE for W4-17 with respect to grid level 6. Reactions were included if they converged for all functionals at all grid levels with the retry logic, not including the orbital gradient descent. This resulted in 199 reactions being included in W4-17 and 96 reactions being included in Diet GMTKN55.

E.3 Convergence with respect to the grid size

To study the effect of the DFT grid we performed benchmark calculations on W4-17 and Diet GMTKN55 using Skala and a variety of traditional functionals, displayed in Fig. 10. Skala displays similar convergence behavior to traditional functionals on both the W4-17 and Diet GMTKN55 benchmarks, with only a small spike on the W4-17 set at grid level 5.

E.4 Computational cost on GPU for exchange correlation energy and electron repulsion integrals

For details on the evaluation dataset and the computational settings see Sec. D.1 and Sec. D.7 respectively. The component timings in Accelerated DFT for the computation of the exchange correlation energy and the electron repulsion integrals (Coulomb for semi-local and Coulomb+Exchange for hybrids) are shown in Fig. 11

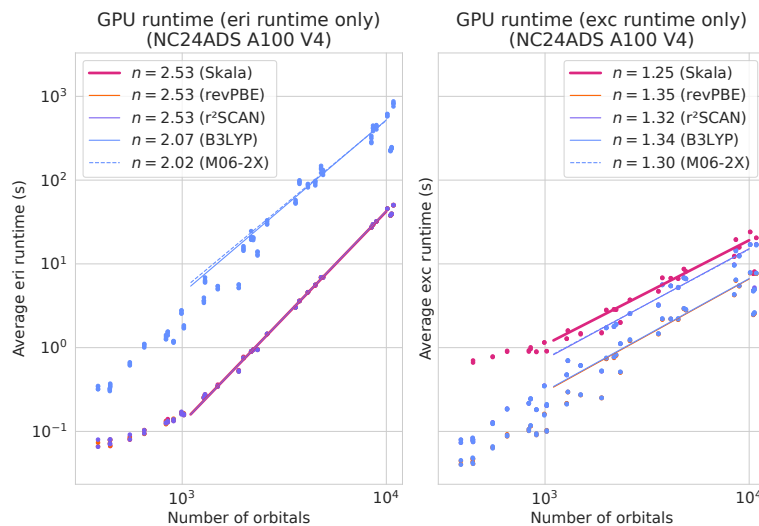


Figure 11: Timing components for Accelerated DFT comparing the electron repulsion integral (eri) and the exchange-correlation (exc) component runtimes. For hybrids the exc component includes only the semi-local part of E_{xc} .

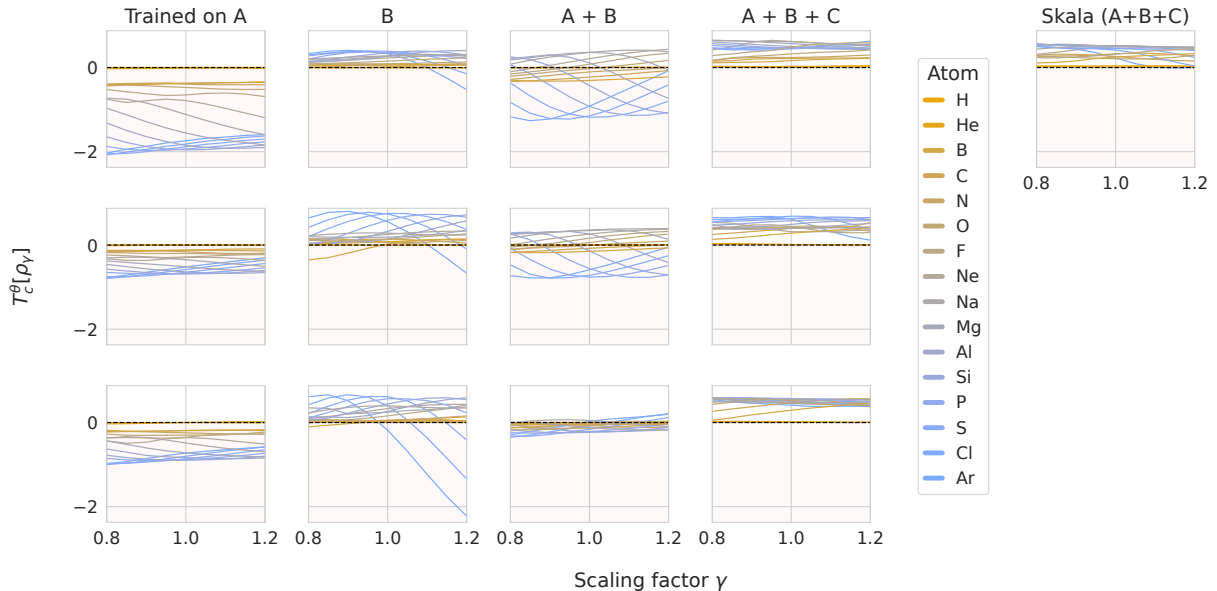


Figure 12: Model T_c of functionals trained with different data compositions and the final Skala functional. The area below the x -axis is shaded in red to indicate the violation of the positivity constraint. The 4 columns on the left represent: results of training Skala on A, MSR-ACC/TAE only, on B, the public data NCIAtlas and W4-CC plus the Atomic datasets only, on A + B, and further adding all the other MSR-ACC data C. The 3 rows represent models trained with different random seeds. On the right, results of the final Skala functional trained on all A + B + C.

E.5 Emergence of exact constraints with more training data

Although the exact functional has an implicit form, several exact constraints that the functional satisfies can be derived.^{222–225} Traditionally, the exact constraints are directly built into the approximate functional by restricting the form of the functional. With a neural network functional, it is harder to incorporate some of these constraints without limiting the model’s expressivity. But with enough data, the model could learn to satisfy the constraints as an emergent behavior. In this section, we investigate a known exact constraint related to the uniform coordinate scaling of the density.

Concretely, a uniformly scaled density is defined as

$$\rho_\gamma(r) = \gamma^3 \rho(\gamma r) \quad (34)$$

where the leading γ^3 factor ensures the scaled density integrates to the same number of electrons for different scaling factors $\gamma > 0$. Larger γ leads to a density squeezed towards the origin, with $\gamma \rightarrow \infty$ commonly known as the high-density limit. Similarly, smaller γ corresponds to a density expanding away from the origin, where $\gamma \rightarrow 0$ is known as the low density limit.

Uniform density scaling allows one to extract the kinetic contribution to the correlation functional, formally defined as

$$T_c[\rho] = T[\rho] - T_s[\rho] \quad (35)$$

where T_s is the KS kinetic energy. Since the interacting ground state needs to compromise between kinetic energy and the Coulomb repulsion, the kinetic energy of the physical system is always higher than the kinetic energy of the non-interacting Kohn-Sham system, which does not need to make this compromise. The kinetic correlation energy T_c is therefore always non-negative.

This quantity can be related to the XC energy on any scaled density via²²²

$$T_c[\rho_\gamma] = \gamma^2 \frac{d}{d\gamma} \frac{E_{xc}[\rho_\gamma]}{\gamma}. \quad (36)$$

To assess the degree of violation of the T_c -positivity constraint, we simply plug our functional E_{xc}^θ into Eq. (36) to obtain the model T_c^θ . We evaluate this quantity on scaled features using the following assignments

$$\rho_{\gamma,i} \leftarrow \gamma^3 \rho_i \quad (37a)$$

$$\|\nabla \rho_{\gamma,i}\| \leftarrow \gamma^4 \|\nabla \rho_i\| \quad (37b)$$

$$\tau_{\gamma,i} \leftarrow \gamma^5 \tau_i \quad (37c)$$

$$w_{\gamma,i} \leftarrow \gamma^{-3} w_i \quad (37d)$$

$$r_{\gamma,i} \leftarrow \gamma^{-1} r_i \quad (37e)$$

where the unscaled counterparts are from a self-consistent calculation. We recall that r_i and w_i are the points and the weights of the integration grids.

In Fig. 12 we present the evaluation of the model T_c^θ on the atoms from the Atomic TOT set in Extended Data Table 1 for all models that were trained for the dataset ablation study, as well as the final Skala model. We see that the T_c -constraint is clearly violated if we only train on the MSR-ACC/TAE set (A). When trained only on the public NCIAtlas, W4-CC, and Atomic datasets (B), the models tend to violate this constraint less frequently, likely because the dissociation curves in NCIAtlas sample small configurational density variations that provide a training signal akin to the derivative term in Eq. (36). When trained on (A + B), the model exhibits mixed performance and increased variance across seeds and atom types. This could be explained by the fact that the benefits of training on the datasets in (B) are diluted when the TAE set (A) is included, given that dataset (A) contains a significantly larger number of reactions (a factor of ~ 6) compared to (B). We obtain a more definite answer when we include all MSR-ACC data (A + B + C). In this case, T_c -positivity is satisfied consistently across all seeds conducted in the data ablation as well as the final Skala model that has been trained with more compute (see Sec. B.4 and Sec. B.3). The emergence of the constraint likely stems from the fact that dataset C contains a sufficiently large proportion of data with relatively smaller density variations, such as those found in the MSR-ACC conformers and reactions datasets.

Supplementary References

123. Kohn, W. & Sham, L. J. Self-Consistent Equations Including Exchange and Correlation Effects. *Phys. Rev.* **140**, A1133. doi:10.1103/PhysRev.140.A1133 (1965).
124. Dirac, P. A. M. Note on Exchange Phenomena in the Thomas Atom. *Math. Proc. Camb. Philos. Soc.* **26**, 376. doi:10.1017/S0305004100016108 (1930).
125. Lieb, E. H. A lower bound for Coulomb energies. *Phys. Lett. A* **70**, 444. doi:10.1016/0375-9601(79)90358-X (1979).
126. Dick, S. & Fernandez-Serra, M. Machine learning accurate exchange and correlation functionals of the electronic density. *Nat. Commun.* **11**, 3509. doi:10.1038/s41467-020-17265-7 (2020).
127. Kasim, M. F. & Vinko, S. M. Learning the Exchange-Correlation Functional from Nature with Fully Differentiable Density Functional Theory. *Phys. Rev. Lett.* **127**, 126403. doi:10.1103/PhysRevLett.127.126403 (2021).
128. Cuierrier, E., Roy, P.-O. & Ernzerhof, M. Constructing and representing exchange–correlation holes through artificial neural networks. *J. Chem. Phys.* **155**, 174121. doi:10.1063/5.0062940 (2021).
129. Kirkpatrick, J. *et al.* Pushing the frontiers of density functionals by solving the fractional electron problem. *Science* **374**, 1385. doi:10.1126/science.abj6511 (2021).
130. Kanungo, B., Hatch, J., Zimmerman, P. M. & Gavini, V. *Learning local and semi-local density functionals from exact exchange-correlation potentials and energies* 2024. <http://arxiv.org/abs/2409.06498>.
131. Lebedev, V. I. & Laikov, D. N. In *Doklady Mathematics* (Pleiades Publishing, Ltd., 1999), 477–481 ().
132. Becke, A. D. A multicenter numerical integration scheme for polyatomic molecules. *J. Chem. Phys.* **88**, 2547. doi:10.1063/1.454033 (1988).
133. Treutler, O. & Ahlrichs, R. Efficient molecular numerical integration schemes. *J. Chem. Phys.* **102**, 346. doi:10.1063/1.469408 (1995).
134. Perdew, J. P. & Schmidt, K. Jacob’s ladder of density functional approximations for the exchange–correlation energy. *AIP Conf. Proc.* **577**, 1. doi:10.1063/1.1390175 (2001).
135. Nagai, R., Akashi, R. & Sugino, O. Completing density functional theory by machine learning hidden messages from molecules. *npj Comput. Mater.* **6**, 1. doi:10.1038/s41524-020-0310-0 (2020).

136. Bystrom, K. & Kozinsky, B. CIDER: An Expressive, Nonlocal Feature Set for Machine Learning Density Functionals with Exact Constraints. *J. Chem. Theory Comput.* **18**, 2180. doi:10.1021/acs.jctc.1c00904 (2022).
137. Grimme, S., Antony, J., Ehrlich, S. & Krieg, H. A consistent and accurate ab initio parametrization of density functional dispersion correction (DFT-D) for the 94 elements H-Pu. *J. Chem. Phys.* **132**, 154104. doi:10.1063/1.3382344 (2010).
138. Grimme, S., Ehrlich, S. & Goerigk, L. Effect of the damping function in dispersion corrected density functional theory. *J. Comput. Chem.* **32**, 1456. doi:10.1002/jcc.21759 (2011).
139. Ramachandran, P., Zoph, B. & Le, Q. V. *Searching for Activation Functions* 2017. doi:10.48550/arXiv.1710.05941.
140. Pyykkö, P. & Atsumi, M. Molecular single-bond covalent radii for elements 1-118. *Chem. (Weinheim an Der Bergstrasse, Ger.)* **15**, 186. doi:10.1002/chem.200800987 (2009).
141. Gasteiger, J., Groß, J. & Günnemann, S. *Directional Message Passing for Molecular Graphs* 2022. doi:10.48550/arXiv.2003.03123.
142. Dusson, G., Bachmayr, M., Csanyi, G., Drautz, R., Etter, S., Oord, C. v. d. & Ortner, C. *Atomic Cluster Expansion: Completeness, Efficiency and Stability* 2021. doi:10.48550/arXiv.1911.03550.
143. Varshalovich, D. A., Moskalev, A. N. & Khersonskii, V. K. *Quantum Theory of Angular Momentum* 1988. <https://www.worldscientific.com/worldscibooks/10.1142/0270>.
144. Batatia, I., Kovacs, D. P., Simm, G., Ortner, C. & Csanyi, G. *MACE: Higher Order Equivariant Message Passing Neural Networks for Fast and Accurate Force Fields in Advances in Neural Information Processing Systems* (Curran Associates, Inc., 2022) (eds Koyejo, S., Mohamed, S., Agarwal, A., Belgrave, D., Cho, K. & Oh, A.) **35** (), 11423–11436. https://proceedings.neurips.cc/paper_files/paper/2022/file/4a36c3c51af11ed9f34615b81edb5bbc-Paper-Conference.pdf.
145. Drautz, R. *Atomic cluster expansion for accurate and transferable interatomic potentials* | *Phys. Rev. B* <https://journals.aps.org/prb/abstract/10.1103/PhysRevB.99.014104>.
146. Greengard, L. & Rokhlin, V. A fast algorithm for particle simulations. *J. Comput. Phys.* **73**, 325. doi:10.1016/0021-9991(87)90140-9 (1987).
147. Gao, N., Eberhard, E. & Günnemann, S. *Learning Equivariant Non-Local Electron Density Functionals* 2024. <http://arxiv.org/abs/2410.07972>.
148. Bätzner, S., Musaelian, A., Sun, L., Geiger, M., Mailoa, J. P., Kornbluth, M., Molinari, N., Smidt, T. E. & Kozinsky, B. E(3)-equivariant graph neural networks for data-efficient and accurate interatomic potentials. *Nat. Commun.* **13**, 2453. doi:10.1038/s41467-022-29939-5 (2022).
149. Sestak, F., Schneckenreiter, L., Brandstetter, J., Hochreiter, S., Mayr, A. & Klambauer, G. *VN-EGNN: E(3)-Equivariant Graph Neural Networks with Virtual Nodes Enhance Protein Binding Site Identification* 2024. doi:10.48550/arXiv.2404.07194.
150. Alkin, B., Fürst, A., Schmid, S., Gruber, L., Holzleitner, M. & Brandstetter, J. *Universal Physics Transformers: A Framework For Efficiently Scaling Neural Operators* 2024. <http://arxiv.org/abs/2402.12365>.
151. Kovachki, N., Li, Z., Liu, B., Azizzadenesheli, K., Bhattacharya, K., Stuart, A. & Anandkumar, A. *Neural Operator: Learning Maps Between Function Spaces* 2023. <http://arxiv.org/abs/2108.08481>.
152. Becke, A. D. Density-functional thermochemistry. III. The role of exact exchange. *J. Chem. Phys.* **98**, 5648. doi:10.1063/1.464913 (1993).
153. Stephens, P. J., Devlin, F. J., Chabalowski, C. F. & Frisch, M. J. Ab Initio Calculation of Vibrational Absorption and Circular Dichroism Spectra Using Density Functional Force Fields. *J. Phys. Chem.* **98**, 11623. doi:10.1021/j100096a001 (1994).
154. Glorot, X. & Bengio, Y. Understanding the difficulty of training deep feedforward neural networks.
155. Geiger, M. & Smidt, T. *e3nn: Euclidean Neural Networks* 2022. doi:10.48550/arXiv.2207.09453.
156. Shazeer, N. & Stern, M. *Adafactor: Adaptive Learning Rates with Sublinear Memory Cost in Proceedings of the 35th International Conference on Machine Learning* (PMLR, 2018) (), 4596–4604. <https://proceedings.mlr.press/v80/shazeer18a.html>.
157. Wolf, T. *et al. Transformers: State-of-the-Art Natural Language Processing in Proceedings of the 2020 Conference on Empirical Methods in Natural Language Processing: System Demonstrations* (Association for Computational Linguistics, 2020) (eds Liu, Q. & Schlangen, D.) (), 38–45. doi:10.18653/v1/2020.emnlp-demos.6.

158. Weigend, F., Furche, F. & Ahlrichs, R. Gaussian basis sets of quadruple zeta valence quality for atoms H–Kr. *J. Chem. Phys.* **119**, 12753. doi:10.1063/1.1627293 (2003).
159. Ehlert, S. *et al.* Accurate Chemistry Collection: Coupled cluster atomization energies for broad chemical space 2025. doi:10.48550/arXiv.2506.14492.
160. Spicher, S. & Grimme, S. Robust Atomistic Modeling of Materials, Organometallic, and Biochemical Systems. *Angewandte Chemie Int. Ed.* **59**, 15665. doi:10.1002/anie.202004239 (2020).
161. Karton, A. & Martin, J. M. L. Explicitly correlated W_n theory: W1-F12 and W2-F12. *J. Chem. Phys.* **136**, 124114. doi:10.1063/1.3697678 (2012).
162. Karton, A., Rabinovich, E., Martin, J. M. L. & Ruscic, B. W4 theory for computational thermochemistry: In pursuit of confident sub-kJ/mol predictions. *J. Chem. Phys.* **125**, 144108. doi:10.1063/1.2348881 (2006).
163. Mester, D. *et al.* Overview of Developments in the MRCC Program System. *J. Phys. Chem. A* **129**, 2086. doi:10.1021/acs.jpca.4c07807 (2025).
164. Peterson, K. A., Adler, T. B. & Werner, H.-J. Systematically convergent basis sets for explicitly correlated wavefunctions: The atoms H, He, B–Ne, and Al–Ar. *J. Chem. Phys.* **128**, 084102. doi:10.1063/1.2831537 (2008).
165. Pracht, P., Bohle, F. & Grimme, S. Automated exploration of the low-energy chemical space with fast quantum chemical methods. *Phys. Chem. Chem. Phys.* **22**, 7169. doi:10.1039/C9CP06869D (2020).
166. Schreiner, M., Bhowmik, A., Vegge, T., Busk, J. & Winther, O. Transition1x - a dataset for building generalizable reactive machine learning potentials. *Sci. Data* **9**, 779. doi:10.1038/s41597-022-01870-w (2022).
167. Zhao, Q., Vaddadi, S. M., Woulfe, M., Ogunfowora, L. A., Garimella, S. S., Isayev, O. & Savoie, B. M. Comprehensive exploration of graphically defined reaction spaces. *Sci. Data* **10**, 145. doi:10.1038/s41597-023-02043-z (2023).
168. Van Gerwen, P., Briling, K. R., Bunne, C., Somnath, V. R., Laplaza, R., Krause, A. & Corminboeuf, C. 3DReact: Geometric Deep Learning for Chemical Reactions. *J. Chem. Inf. Model.* **64**, 5771. doi:10.1021/acs.jcim.4c00104 (2024).
169. Unsleber, J. P., Grimm, S. A. & Reiher, M. Chemoton 2.0: Autonomous Exploration of Chemical Reaction Networks. *J. Chem. Theory Comput.* **18**, 5393. doi:10.1021/acs.jctc.2c00193 (2022).
170. Young, T. A., Silcock, J. J., Sterling, A. J. & Duarte, F. autodE: Automated Calculation of Reaction Energy Profiles— Application to Organic and Organometallic Reactions. *Angewandte Chemie Int. Ed.* **60**, 4266. doi:10.1002/anie.202011941 (2021).
171. Staroverov, V. N., Scuseria, G. E., Tao, J. & Perdew, J. P. Comparative assessment of a new nonempirical density functional: Molecules and hydrogen-bonded complexes. *J. Chem. Phys.* **119**, 12129. doi:10.1063/1.1626543 (2003).
172. Karton, A. & Martin, J. M. L. Comment on: “Estimating the Hartree–Fock limit from finite basis set calculations” [Jensen F (2005) *Theor Chem Acc* 113:267]. *Theor. Chem. Accounts* **115**, 330. doi:10.1007/s00214-005-0028-6 (2006).
173. Karton, A., Tarnopolsky, A. & M.L. Martin, J. Atomization energies of the carbon clusters C_n ($n = 2–10$) revisited by means of W4 theory as well as density functional, Gn, and CBS methods. *Mol. Phys.* **107**, 977. doi:10.1080/00268970802708959 (2009).
174. Řezáč, J. Non-Covalent Interactions Atlas Benchmark Data Sets 2: Hydrogen Bonding in an Extended Chemical Space. *J. Chem. Theory Comput.* **16**, 6305. doi:10.1021/acs.jctc.0c00715 (2020).
175. Řezáč, J. Non-Covalent Interactions Atlas Benchmark Data Sets: Hydrogen Bonding. *J. Chem. Theory Comput.* **16**, 2355. doi:10.1021/acs.jctc.9b01265 (2020).
176. Kříž, K., Nováček, M. & Řezáč, J. Non-Covalent Interactions Atlas Benchmark Data Sets 3: Repulsive Contacts. *J. Chem. Theory Comput.* **17**, 1548. doi:10.1021/acs.jctc.0c01341 (2021).
177. Kříž, K. & Řezáč, J. Non-covalent interactions atlas benchmark data sets 4: σ -hole interactions. *Phys. Chem. Chem. Phys.* **24**, 14794. doi:10.1039/D2CP01600A (2022).
178. Řezáč, J. Non-Covalent Interactions Atlas benchmark data sets 5: London dispersion in an extended chemical space. *Phys. Chem. Chem. Phys.* **24**, 14780. doi:10.1039/D2CP01602H (2022).
179. Sun, Q. *et al.* PySCF: the Python-based simulations of chemistry framework. *WIREs Comput. Mol. Sci.* **8**, e1340. doi:10.1002/wcms.1340 (2018).

180. Zheng, J., Xu, X. & Truhlar, D. G. Minimally augmented Karlsruhe basis sets. *Theor. Chem. Accounts* **128**, 295. doi:10.1007/s00214-010-0846-z (2011).
181. Karton, A., Sylvetsky, N. & Martin, J. M. L. W4-17: A diverse and high-confidence dataset of atomization energies for benchmarking high-level electronic structure methods. *J. Comput. Chem.* **38**, 2063. doi:10.1002/jcc.24854 (2017).
182. Goerigk, L., Hansen, A., Bauer, C., Ehrlich, S., Najibi, A. & Grimme, S. A look at the density functional theory zoo with the advanced GMTKN55 database for general main group thermochemistry, kinetics and noncovalent interactions. *Phys. Chem. Chem. Phys.* **19**, 32184. doi:10.1039/c7cp04913g (2017).
183. Gould, T. ‘Diet GMTKN55’ offers accelerated benchmarking through a representative subset approach. *Phys. Chem. Chem. Phys.* **20**, 27735. doi:10.1039/C8CP05554H (2018).
184. Hait, D. & Head-Gordon, M. How accurate are static polarizability predictions from density functional theory? An assessment over 132 species at equilibrium geometry. *Phys. Chem. Chem. Phys.* **20**, 19800. doi:10.1039/C8CP03569E (2018).
185. Grimme, S., Brandenburg, J. G., Bannwarth, C. & Hansen, A. Consistent structures and interactions by density functional theory with small atomic orbital basis sets. *J. Chem. Phys.* **143**, 054107. doi:10.1063/1.4927476 (2015).
186. Piccardo, M., Penocchio, E., Puzzarini, C., Biczysko, M. & Barone, V. Semi-Experimental Equilibrium Structure Determinations by Employing B3LYP/SNSD Anharmonic Force Fields: Validation and Application to Semirigid Organic Molecules. *J. Phys. Chem. A* **119**, 2058. doi:10.1021/jp511432m (2015).
187. Grimme, S. Exploration of Chemical Compound, Conformer, and Reaction Space with Meta-Dynamics Simulations Based on Tight-Binding Quantum Chemical Calculations. *J. Chem. Theory Comput.* **15**, 2847. doi:10.1021/acs.jctc.9b00143 (2019).
188. Sure, R. & Grimme, S. Comprehensive Benchmark of Association (Free) Energies of Realistic Host–Guest Complexes. *J. Chem. Theory Comput.* **11**, 3785. doi:10.1021/acs.jctc.5b00296 (2015).
189. Gorges, J., Grimme, S. & Hansen, A. Reliable prediction of association (free) energies of supramolecular complexes with heavy main group elements – the HS13L benchmark set. *Phys. Chem. Chem. Phys.* **24**, 28831. doi:10.1039/D2CP04049B (2022).
190. Gorges, J., Baendorf, B., Grimme, S. & Hansen, A. Efficient computation of the interaction energies of very large non-covalently bound complexes. *Synlett* **34**, 1135. doi:10.1055/s-0042-1753141 (2023).
191. Zhang, Y. & Yang, W. Comment on “Generalized Gradient Approximation Made Simple”. *Phys. Rev. Lett.* **80**, 890. doi:10.1103/PhysRevLett.80.890 (1998).
192. Mardirossian, N. & Head-Gordon, M. Mapping the genome of meta-generalized gradient approximation density functionals: The search for B97M-V. *J. Chem. Phys.* **142**, 074111. doi:10.1063/1.4907719 (2015).
193. Furness, J. W., Kaplan, A. D., Ning, J., Perdew, J. P. & Sun, J. Accurate and Numerically Efficient r2SCAN Meta-Generalized Gradient Approximation. *J. Phys. Chem. Lett.* **11**, 8208. doi:10.1021/acs.jpcllett.0c02405 (2020).
194. Ehlert, S., Huniar, U., Ning, J., Furness, J. W., Sun, J., Kaplan, A. D., Perdew, J. P. & Brandenburg, J. G. r2SCAN-D4: Dispersion corrected meta-generalized gradient approximation for general chemical applications. *J. Chem. Phys.* **154**, 061101. doi:10.1063/5.0041008 (2021).
195. Zhao, Y. & Truhlar, D. G. The M06 suite of density functionals for main group thermochemistry, thermochemical kinetics, noncovalent interactions, excited states, and transition elements: two new functionals and systematic testing of four M06-class functionals and 12 other functionals. *Theor. Chem. Accounts* **120**, 215. doi:10.1007/s00214-007-0310-x (2008).
196. Mardirossian, N. & Head-Gordon, M. ω B97X-V: A 10-parameter, range-separated hybrid, generalized gradient approximation density functional with nonlocal correlation, designed by a survival-of-the-fittest strategy. *Phys. Chem. Chem. Phys.* **16**, 9904. doi:10.1039/C3CP54374A (2014).
197. Mardirossian, N. & Head-Gordon, M. ω B97M-V: A combinatorially optimized, range-separated hybrid, meta-GGA density functional with VV10 nonlocal correlation. *J. Chem. Phys.* **144**, 214110. doi:10.1063/1.4952647 (2016).
198. Vydrov, O. A. & Van Voorhis, T. Nonlocal van der Waals density functional: The simpler the better. *J. Chem. Phys.* **133**, 244103. doi:10.1063/1.3521275 (2010).
199. Ehlert, S. Simple DFT-D3: Library first implementation of the D3 dispersion correction. *J. Open Source Softw.* **9**, 7169. doi:10.21105/joss.07169 (2024).

200. Weigend, F. & Ahlrichs, R. Balanced basis sets of split valence, triple zeta valence and quadruple zeta valence quality for H to Rn: Design and assessment of accuracy. *Phys. Chem. Chem. Phys.* **7**, 3297. doi:10.1039/B508541A (2005).
201. Ambrose, M. A. & Jensen, F. Probing Basis Set Requirements for Calculating Core Ionization and Core Excitation Spectroscopy by the Δ Self-Consistent-Field Approach. *J. Chem. Theory Comput.* **15**, 325. doi:10.1021/acs.jctc.8b01071 (2019).
202. Sun, Q. *et al.* Recent developments in the PySCF program package. *J. Chem. Phys.* **153**, 024109. doi:10.1063/5.0006074 (2020).
203. Li, R., Sun, Q., Zhang, X. & Chan, G. K.-L. Introducing GPU Acceleration into the Python-Based Simulations of Chemistry Framework. *J. Phys. Chem. A* **129**, 1459. doi:10.1021/acs.jpca.4c05876 (2025).
204. Eichkorn, K., Treutler, O., Öhm, H., Häser, M. & Ahlrichs, R. Auxiliary basis sets to approximate Coulomb potentials. *Chem. Phys. Lett.* **240**, 283. doi:10.1016/0009-2614(95)00621-A (1995).
205. Eichkorn, K., Weigend, F., Treutler, O. & Ahlrichs, R. Auxiliary basis sets for main row atoms and transition metals and their use to approximate Coulomb potentials. *Theor. Chem. Accounts* **97**, 119. doi:10.1007/s002140050244 (1997).
206. Van Lenthe, J. H., Zwaans, R., Van Dam, H. J. J. & Guest, M. F. Starting SCF calculations by superposition of atomic densities. *J. Comput. Chem.* **27**, 926. doi:10.1002/jcc.20393 (2006).
207. Almlöf, J., Faegri, K. & Korsell, K. Principles for a direct SCF approach to LICAO-MOab-initio calculations. *J. Comput. Chem.* **3**, 385. doi:10.1002/jcc.540030314 (1982).
208. Pulay, P. Convergence acceleration of iterative sequences. the case of scf iteration. *Chem. Phys. Lett.* **73**, 393. doi:10.1016/0009-2614(80)80396-4 (1980).
209. Pulay, P. Improved SCF convergence acceleration. *J. Comput. Chem.* **3**, 556. doi:10.1002/jcc.540030413 (1982).
210. Sun, Q., Yang, J. & Chan, G. K.-L. A general second order complete active space self-consistent-field solver for large-scale systems. *Chem. Phys. Lett.* **683**, 291. doi:10.1016/j.cpllett.2017.03.004 (2017).
211. Seeger, R. & Pople, J. A. Self-consistent molecular orbital methods. XVIII. Constraints and stability in Hartree-Fock theory. *J. Chem. Phys.* **66**, 3045. doi:10.1063/1.434318 (1977).
212. Bendokat, T., Zimmermann, R. & Absil, P.-A. A Grassmann manifold handbook: basic geometry and computational aspects. *Adv. Comput. Math.* **50**, 6. doi:10.1007/s10444-023-10090-8 (2024).
213. Helgaker, T., Jørgensen, P. & Olsen, J. *Molecular Electronic-Structure Theory* (Wiley, 2000) ().
214. Nocedal, J. & Wright, S. J. *Numerical optimization* Second edition (Springer, 2006) ().
215. Pulay, P. *Ab initio* calculation of force constants and equilibrium geometries in polyatomic molecules: I. Theory. *Mol. Phys.* **17**, 197. doi:10.1080/00268976900100941 (1969).
216. Wang, L.-P. & Song, C. Geometry optimization made simple with translation and rotation coordinates. *J. Chem. Phys.* **144**, 214108. doi:10.1063/1.4952956 (2016).
217. Ju, F. *et al.* *Acceleration without Disruption: DFT Software as a Service* 2024. doi:10.48550/arXiv.2406.11185.
218. Petrone, A., Williams-Young, D. B., Sun, S., Stetina, T. F. & Li, X. An efficient implementation of two-component relativistic density functional theory with torque-free auxiliary variables. *Eur. Phys. J. B* **91**, 169. doi:10.1140/epjb/e2018-90170-1 (2018).
219. Williams-Young, D. B., de Jong, W. A., van Dam, H. J. J. & Yang, C. On the Efficient Evaluation of the Exchange Correlation Potential on Graphics Processing Unit Clusters. *Front. Chem.* **8**. doi:10.3389/fchem.2020.581058 (2020).
220. Williams-Young, D. B., Asadchev, A., Popovici, D. T., Clark, D., Waldrop, J., Windus, T. L., Valeev, E. F. & de Jong, W. A. Distributed memory, GPU accelerated Fock construction for hybrid, Gaussian basis density functional theory. *J. Chem. Phys.* **158**, 234104. doi:10.1063/5.0151070 (2023).
221. Perdew, J. P., Chowdhury, S. T. u. R., Shahi, C., Kaplan, A. D., Song, D. & Bylaska, E. J. Symmetry Breaking with the SCAN Density Functional Describes Strong Correlation in the Singlet Carbon Dimer. *J. Phys. Chem. A* **127**, 384. doi:10.1021/acs.jpca.2c07590 (2023).
222. Levy, M. & Perdew, J. P. Hellmann-Feynman, virial, and scaling requisites for the exact universal density functionals. Shape of the correlation potential and diamagnetic susceptibility for atoms. *Phys. Rev. A* **32**, 2010. doi:10.1103/PhysRevA.32.2010 (1985).

223. Kaplan, A. D., Levy, M. & Perdew, J. P. *Predictive Power of the Exact Constraints and Appropriate Norms in Density Functional Theory* 2022. doi:10.1146/annurev-physchem-062422-013259.
224. Lieb, E. H. Density functionals for coulomb systems. *Int. J. Quantum Chem.* **24**, 243. doi:10.1002/qua.560240302 (1983).
225. Sun, J., Ruzsinszky, A. & Perdew, J. P. Strongly Constrained and Appropriately Normed Semilocal Density Functional. *Phys. Rev. Lett.* **115**, 036402. doi:10.1103/PhysRevLett.115.036402 (2015).